Evaluating Use of Sub-Grade Drains with PFC for Stormwater Drainage: Final Report

Technical Report 0-6843-1

Cooperative Research Program

UNIVERSITY OF TEXAS AT SAN ANTONIO
DEPARTMENT OF CIVIL AND ENVIRONMENTAL ENGINEERING
SAN ANTONIO, TEXAS 78249

in cooperation with the
Federal Highway Administration and the
Texas Department of Transportation

1. Report No.
FHWA/TX-17/0-6843-1

2. Government Accession No.

3. Recipient's Catalog No.

4. Title and Subtitle
EVALUATING USE OF SUB-GRADE DRAINS WITH PFC FOR STORMWATER DRAINAGE

5. Report Date
August 2017

6. Performing Organization Code

7. Author(s)
Jie Huang, Ted Cleveland, Hatim Sharif, Samer Dessouky, Elma Annette Hernandez, and Chao Zheng

8. Performing Organization Report No.
Report 0-6843-1

9. Performing Organization Name and Address
University of Texas at San Antonio
Department of Civil
and Environmental Engineering
San Antonio, Texas 78249

Texas Tech University
Department of Civil, Environmental,
and Construction Engineering
Lubbock, TX 79409−1023

10. Work Unit No. (TRAIS)

11. Contract or Grant No.
Project 0-6843

12. Sponsoring Agency Name and Address
Texas Department of Transportation
Research and Technology Implementation Office
125 E. 11th Street
Austin, Texas 78701-2483

13. Type of Report and Period Covered
Technical Report:
February 2015–January 2017

14. Sponsoring Agency Code

15. Supplementary Notes
Project performed in cooperation with the Texas Department of Transportation and the Federal Highway Administration.
Project Title: Evaluating Use of Sub-Grade Drains with PFC for Stormwater Drainage
URL:

16. Abstract
The overarching objective of this project is to evaluate the effectiveness of incorporated subgrade drain (usually called "underdrain") in the permeable friction course (PFC) pavement to facilitate drainage of stormwater within and on the pavement. The researchers from the University of Texas at San Antonio (UTSA) and Texas Tech University (TTU) utilized large-scale physical model testing and numerical simulation to assess the water accumulation within and on the pavement under different rainfall intensities for different pavement configurations. In the TTU campus, a large-scale model facility was built to accommodate a PFC pavement with a dimension of 48 × 6 ft^2 and a 2% slope in the long direction. The rainfall was generated by a rain simulator that was connected to an oscillator. With the data collected from the model test, a numerical model was calibrated to further investigate the effectiveness of the underdrain for full scale travel lanes. The numerical model coupled 2D nonlinear hydrodynamic model for the surface run-off and 3D subsurface flow model for seepage within the PFC to account for the water flow within the pavement and underdrain as well as the flow on the pavement surface. For this study, the performance of underdrain for PFC pavement with 2, 3, and 4 lanes with a combination of a cross slope (i.e., 1%, 2% and 3%) and longitudinal slope (i.e., 0% and 1%) under low, moderate, heavy and extreme rainfall intensities was investigated. The effectiveness of underdrain was quantified by comparing with the water accumulation at PFC pavement without underdrain. It was found out that in general the underdrain could effectively remove standing (ponding) water on the pavement surface under moderate to heavy rainfall conditions. Based on the influence range of underdrain, spacing for underdrain under various pavement slope and rainfall intensity is proposed.

17. Key Words
permeable/porous frictional course (PFC) pavements, underdrain, stormwater

18. Distribution Statement

19. Security Classif. (of this report)
Unclassified

20. Security Classif. (of this page)
Unclassified

21. No. of Pages
118

22. Price

EVALUATING USE OF SUB-GRADE DRAINS WITH PFC FOR STORMWATER DRAINAGE

by

Jie Huang, Associate Professor
Hatim Sharif, Professor
Samer Dessouky, Professors
Chao Zheng, Graduate Research Assistant

Civil and Environmental Engineering
University of Texas at San Antonio
One UTSA Circle
San Antonio, TX 78249

Theodore Cleveland, Associate Professor
E. Annette Hernandez, Associate Professor
Caroline M. Neale, Graduate Research Assistant
Texas Tech University
Department of Civil, Environmental, and Construction Engineering
Lubbock, TX 79409−1023

Xiaofeng Liu, Assistant Professor
Department of Civil and Environmental Engineering
Penn State University

Report 0-6843-1
Project 0-6843
Project Title: Evaluating Use of Sub-Grade Drains with PFC for Stormwater Drainage

Performed in cooperation with the
Texas Department of Transportation
and the
Federal Highway Administration

September 1, 2017

UNIVERSITY OF TEXAS AT SAN ANTONIO
Department of Civil and Environmental Engineering
One UTSA Circle
San Antonio, Texas 78249

[This page is intentionally left blank.]

DISCLAIMER

The contents of this report reflect the views of the author(s), who is (are) responsible for the facts and the accuracy of the data presented in this report. The contents do not necessarily reflect the official view or policies of the Federal Highway Administration (FHWA) or the Texas Department of Transportation (TxDOT). This report does not constitute a standard, specification, or regulation. The United States Government and the State of Texas do not endorse products or manufacturers. Trade or manufacturers names appear herein solely because they are considered essential to the object of this report. The researcher in charge of this project was Dr. Jie Huang at University of Texas at San Antonio (UTSA).

There was no invention or discovery conceived or first actually reduced to practice in the course of or under this contract (to data), including any art, method, process, machine, manufacture, design, or composition of matter, or any new useful improvement thereof, or any variety of plant, which is or may be patentable under the patent laws of the United States of America or any foreign country.

ACKNOWLEDGMENTS

The authors thank the Texas Department of Transportation staff members — Chris Graf, Paul Wong, Ron Baker, Stan Hopfe, and Tom Beck — for their professional expertise and insights related to this project. Special thanks will go to the project manager, Sonya Badgley, who provided support and coordination throughout this project.

TABLE OF CONTENTS

LIST OF FIGURES

LIST OF TABLES

EXECUTIVE SUMMARY

Permeable friction course (PFC) pavement, characterized by its high permeability, has gradually gained attention in U.S., especially in southern states as it can remove or reduce standing (ponding) water on the roadway during rainy days. The voids in the PFC pavement provide drainage paths for water, with an associated permeability ranging from 0.2 in ~ 2 in/hr. Texas Department of Transportation (TxDOT) currently owns nearly 3,000 miles of permeable friction course (PFC) pavement in its highway system, which provides a safe driving condition during wet days. However, under certain circumstances, the PFC pavement still cannot remove the water quickly, resulting in water accumulation and splashing, for example, when the transverse slope is negligible (superelevation transition) and/or the rainfall intensity is too high. For such situations, the subgrade drain (usually called "underdrain"), installed at the bottom of the PFC pavement in the transverse direction, can further guide the water out. To assess the effectiveness of the underdrain under various conditions, this project employs large-scale physical testing and numerical simulations to study the water accumulation within and on the PFC pavement.

For the large-scale physical testing, a 48 feet long, 6 feet wide, 2 inches thick PFC pavement with a uniform 2% slope in the long direction was built inside a flume. The pavement was divided into 12 sections with 4 × 6 ft^2 individually. Each section was instrumented by 4 ~ 6 manometers at the bottom to acquire the water depth inside the PFC pavement. A 4-inch perforated PVC pipe, acting as underdrain, was installed at the bottom of the pavement. A rain simulator generated a rainfall up to approximately 6 in/hr, which was monitored by a rain gauge. The outflow at the bottom edge of the pavement was collected by measuring buckets to find out the outflow rate as well as total outflow quantity. The tests were proceeded with one of the two following scenarios: with underdrain (PVC pipe valve was open) and without underdrain (PVC pipe valve was close). There were totally 41 tests completed with different rainfall intensities and underdrain scenarios.

Upon the completion of the large-scale physical testing, a numerical model was developed and then calibrated by the obtained data from the physical model testing. The numerical model was employed by coupling the shallow water equation and 3D Richards equation. The surface flow was simulated by the shallow water equation, and the subsurface flow was modeled by the Richards equation. Then both equations were coupled based on mass balance and momentum conservation. With the calibrated model, the 2-lane (24 feet), 3-lane (36 feet) and 4-lane (48 feet) pavement with transverse slopes 0%, 1%, 2% and 3% and longitudinal slopes 0%, 1% were investigated under a rainfall intensity of 0.4, 1.0, 3.0 and 5.0 in/hr. Based on the results from the simulations, it was found out:

- PFC pavement was sufficient by itself to drain out water (no ponding) for 2-lane, 3-lane and 4-lane pavement when the rain intensity was no more than 0.4 in/hr under all slope conditions that assessed in this work. And increasing the slope would facilitate the drainage.

- The underdrain was needed to remove the ponding water on pavement surface when the rain intensity was over 0.4 in/hr for all the slope situations of 2-lane, 3-lane and 4-lane pavement investigated in the study.
- Increasing the slopes in both transverse and longitudinal directions does not necessarily mean an increase of the underdrain's effective range. The slope in both direction made the water distribution more unevenly. The data showed that the water was accumulated more at the toe of slope, causing ponding at the lower corner of the pavement.
- At high rainfall intensity (> 4 in/hr), to remove ponding water the underdrains would need to be closely spaced (a few feet apart), which may be impractical.

The effective ranges of the underdrain for various slopes, pavement widths and rainfall intensities are tabulated in this report, which can be used for planning the underdrain.

CHAPTER 1: INTRODUCTION

STATEMENT OF THE PROBLEM

Standing water on pavement travel lanes is an obvious and well-documented safety problem and is among the top five reasons causing car accidents. Removing water timely is the driving reason for highway drainage structures and its associated appurtenances. Curb inlets, slotted drains, grate inlets, roadside ditches, storm sewers, lift stations, drainage swales are used to convey water away from travel lanes to reduce spray and splash (visibility and vehicle control) and reduce or eliminate the chance of hydroplaning (vehicle control) (Berbee et al. 1999; Stotz and Krauth 1994).

In addition to all of the above conventional drainage design options, porous friction course (PFC), which is an overlay of porous asphalt placed in a typical 2 inches or thinner layer on top of conventional impermeable pavement, is gaining popularity. Europe initiated the use of PFC in 1970s and demonstrated its advantage in improving wet weather frictional properties, reducing the potential for hydroplaning, and reducing the amount of splash and spray (Cooley et al. 2009; Isenring et al. 1990).

Rainfall water seeps into the porous layer and flows to the side of the road by gravity. This desired drainage property, i.e., removing water from the road surface, improves road safety by reducing splashing and hydroplaning. In addition to reducing surface runoff and flooding, the benefits of PFC include the enhancement of groundwater recharge, filters and improve the water quality of runoff, reduces heat island effects while providing the load-carrying capacity of conventional pavement. From the point of drainage capacity, the design of PFCs needs to meet the goal of properly routing the stormwater through the porous matrix to minimize the depth of water film on the surface. Design charts and mathematical models have been developed to aid in such design. However, the experience has found out that sometimes the water still could not drain out timely, when the roadways are wide and/or have limited slope, and/or the rainfall is heavy. To address this issue, underdrain is proposed to be incorporated and placed at the bottom of the PFC pavement in the transverse direction to further facilitate water drainage. However, there is no methods or data available to assess the effectiveness of the proposed underdrain in PFC pavements.

OBJECTIVES AND TASKS OF THIS PROJECT

The overarching objective of the study is to assess effectiveness of the proposed underdrain in PFC pavement and quantify drainage capacity by comparing the hydraulic performance of PFC pavement with underdrain to that of PFC pavement without underdrain. To fulfil the objective, the following tasks were performed:

- Conduct a comprehensive literature review on PFC pavement with focus on its hydraulic properties as well as drainage related design,

- Build a large-scale indoor test facility and test PFC pavement with embedded underdrain under different rainfall intensities,
- Develop and calibrate a numerical model and employ the developed model to further assess the PFC pavement with underdrain for various conditions, and
- Analyze the test and numerical data and provide recommendations for practice

Upon the completion of the above-itemized tasks, a recommendation of the spacing of the underdrain for different transverse slopes and rainfall intensities has been provided at the end of this report.

CHAPTER 2: LITERATURE REVIEW

A BRIEF HISTORY OF PFC PAVEMENT

Generally speaking, the Permeable Friction Course (PFC) pavement originates from open-graded friction course (OGFC) pavements that were initially used by Oregon and California in the 1930s and 1940s respectively. In the 1930s, Oregon used a plant mix seal coats that consisted of open-graded aggregates to improve the surface friction of the pavement, while in the 1940s California used a similar mix to provide a drainage layer at the pavement surface (Cooley et al. 2009; Huber 2000). Although the mixes showed good drainage capacity and resistance to skid, they did not perform well in the long term due to lack of bonding between aggregates. In the 1970s, Europe derived a new mix from the U.S. OGFC mix by increasing the void content to at least 18% and adding material (primarily fiber) to the binder to improve bonding as well as prevent premature failure (Isenring et al. 1990). Such new OGFC is now commonly called PFC worldwide. Since the 1980s, the usage of PFC, with the void space of 18 ~ 22% (APC 2003), has been steadily increasing due to its effect on minimizing hydroplaning and splash/spray, noise reduction, and excellent friction properties (Caltrans 2006; Kandhal and Mallick 1998). So far, nearly every southern state of the U.S. has PFC pavements (Cooley et al. 2009; Huber 2000). The milestones of the PFC mix/pavement are listed below (Cooley et al. 2009; Decoene 1990; Huber 2000; Isenring et al. 1990; Kandhal and Mallick 1998; Ruiz et al. 1990; van Der Zwan et al. 1990):

- 1930s Oregon started to use OGFC to improve pavement
- 1940s California used OGFC to improve drainage
- 1972 Switzerland and Netherlands built their first PFC pavements
- 1980s PFC pavements became popular in Europe and miles of PFC pavements was built in Spain, Italy, France, Belgium, Austria, and the United Kingdom
- 1992 Georgia DOT used PFC to build some sections of I-75, which was the first usage of PFC in major U.S. highways
- 1990s PFC pavement has spread to Canada, Australia and many other Asian countries

According to the NCHRP survey completed in 2009, PFC has been used in many interstate highways of the southern and western states, such as Texas, Louisiana, New Mexico, California, Georgia, North Carolina, Arizona, Alabama, Mississippi. However, due to the difficulties in winter maintenance, the applications of PFC pavements are still limited in Northern and mid-western states as indicated in Figure 1. (Note: Figure 1 shows “no answer” for Arizona and New Mexico; however, another survey completed by Cooley et al. (2009) indicated that these two states used PFC pavements.)

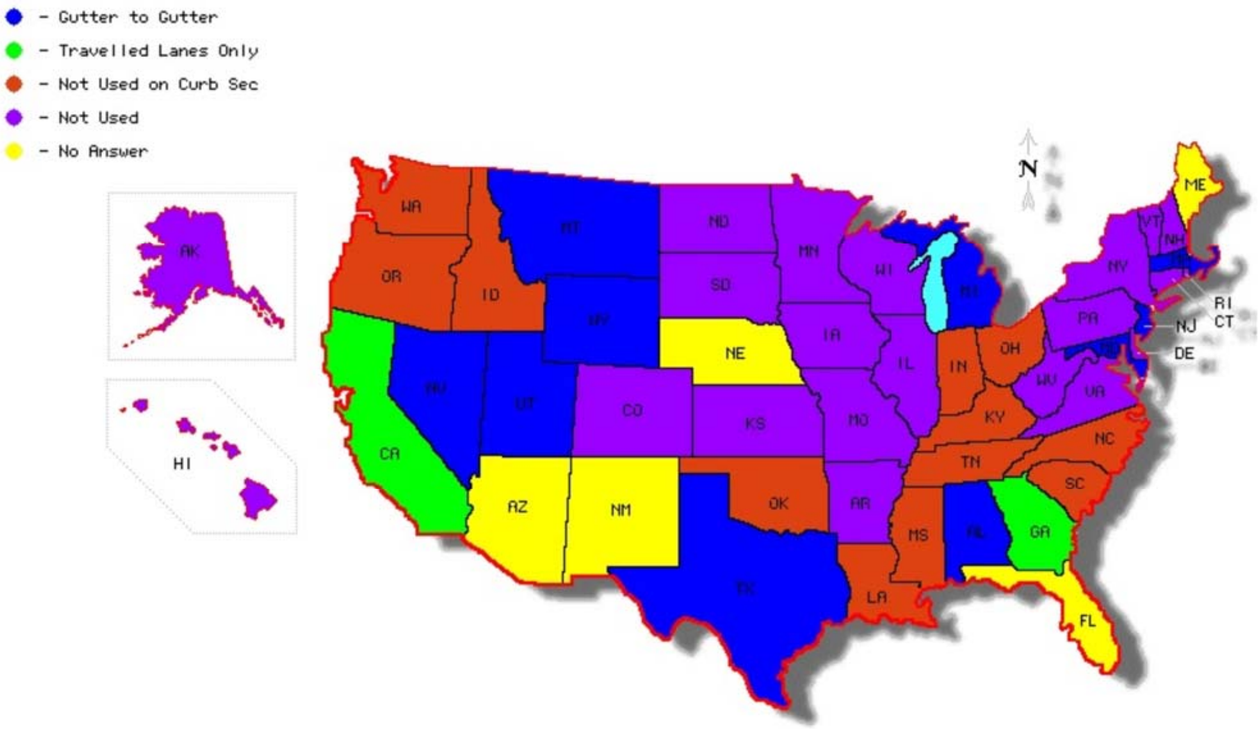

Figure 1. Survey of PFC usage in U.S. completed by TxDOT (Sampson et al. 2014)

Compared with conventional hot mixed asphalt (HMA) pavements, PFC pavements are featured with higher air void, open-grade coarse aggregate gradation, and low compaction effort, which make them advantageous in terms of surface friction and drainage in the wet weather. A simple comparison between conventional HMA and PFC pavements is provided in Table 1, which is based on the published literatures.

Table 1. Comparison of Conventional HMA and PFC pavements (Alvarez et al. 2006; Cooley et al. 2007; Cooley et al. 2009; Liu et al. 2010; Yildirim et al. 2007)

	Conventional HMA pavements	PFC pavements
Service life	12~15 years	6~10 years
Materials	Asphalt binder and aggregate	Asphalt binder, aggregate and additives (fibers)
Air void	4%	18~22%
Design	AASHTO design methodology	DOTs have their own design methods
Compaction	Various compactors	Only static steel wheel rollers
Usage	For various roadways	Use only for a thin layer of overlay on the conventional HMA pavement to improve friction and drainage during wet weather

PFC PAVEMENT IN TEXAS

TxDOT started to use PFC in the 1990s, which was defined as a surface course of a compacted permeable mixture of aggregate, asphalt binder, and additives according to TxDOT specification Item 324 (TxDOT 2004). So far, TxDOT has nearly four thousand miles of PFC pavements. The annual usage of PFC mix exceeds 100,000 tons according to the reported data in 2013 and 2009, respectively (Arambula 2013; Cooley et al. 2009). The distribution of the TxDOT PFC pavements is illustrated in Figure 2. Nearly every district of TxDOT has, more or less, some sections of PFC pavements.

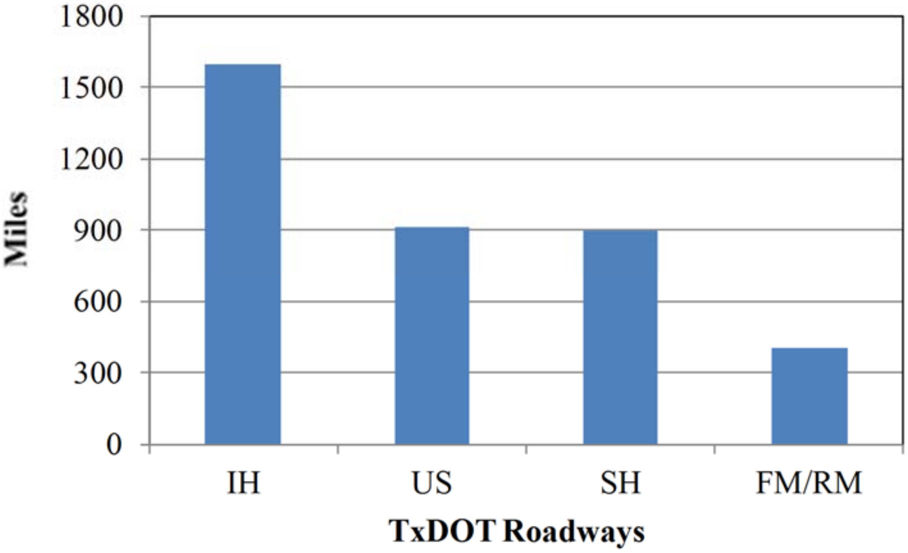

Figure 2. PFC pavements in Texas.

The TxDOT sponsored study (TxDOT 0-5836) evaluated the performance of PFC pavement across Texas in terms of noise, durability, drainability, texture, friction, skid resistance, and distress. The statistical data indicated that comparing with conventional HMA pavements the PFC pavements had better drainage, lower noise level, and superior texture and resistance to skid, which reduced the number of accidents, injuries and fatalities on the Texas roadways. The study transmitted an encouraging message for the application of PFC pavements in Texas.

ADVANTAGES AND DISADVANTAGES OF PFC PAVEMENTS

As aforementioned, the primary advantages of the PFC pavement are its capacity of water and noise reduction (Bean et al. 2007; Brown 1973; Collins et al. 2011; Kearfott et al. 2005; Khalid and Perez 1996). Recently, it has been found that PFC pavements could improve water runoff quality by retaining some contaminants.

<u>Reduction on water and water related issue:</u> PFC pavement has a permeability ranging approximately from 0.1 to 2 inch/s, depending on the porosity (Charbeneau 2011; Cooley et al. 2009). Such a high permeability allows water to drain fast to prevent water standing on the pavement surface, which has been the major cause for the wet weather related accidents and traffic jams on the roadways. Numerous studies in U.S. and Europe have proven that the PFC can significantly reduce the accidents in the wet weather and improve the ride comfort (Cooley et al. 2007). According to Luce et al. (2007), with better visibility and skid resistance, PFC pavements reduced accidents in wet weather by 54% and overall accidents by 29%, while Miller and Johnson (1973) reported 63% of accidents reduction in the wet weather. The benefit of PFC pavements in wet weather is shown in Figures 3-5.

Figure 3. PFC pavement reduce water standing on pavement during a rainstorm (modified from Poulikakos et al. (2003)).

Figure 4. PFC pavement reduces splash and improve visibility in the evening (Barrett and Stanard (2008))

Figure 5. PFCs in urban areas to reduce splash and spray (San Antonio IH 35) (Arambula (2013))

Noise reduction: PFC pavements result in noise reduction at the tire/pavement-interface due to the interface air pressure release and the improved surface texture (Cooley et al. 2007; Liu et al. 2010). When tires are rolling over a pavement, air trapped in the tire treads is first compressed between the tire and the pavement, and is then released as the tires continue to roll as shown in Figure 6. Such repeating process creates noises during driving. In contrast, as tires roll over PFC pavements, the air in the tire treads is able to escape through the voids of the PFC skeleton. As a result, such noise can be significantly reduced. In addition, the maximum aggregate size of PFC pavements is usually smaller than conventional HMA pavements, which can improve the surface texture and, consequently, further reduce the noise. Studies have shown that the tire/pavement noise level reduction on PFC pavements ranged from 3 to 9 dBA in U.S. and up to 10 dBA in Europe (Bendtsen and Andersen 2005; Donavan 2005; Liu et al. 2010).

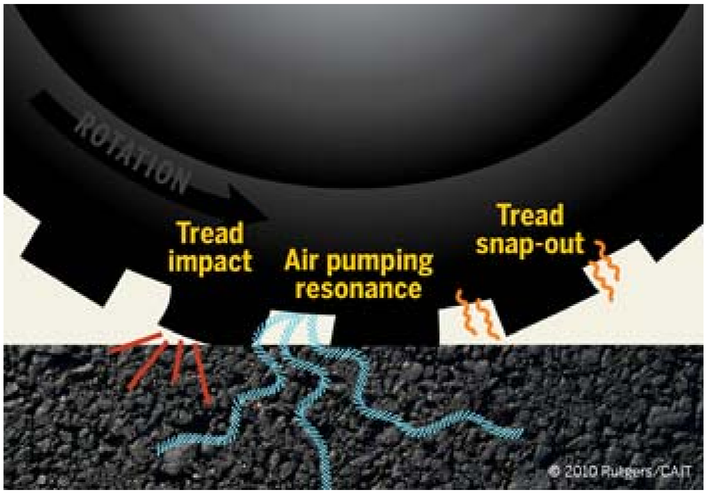

Figure 6. Tire-pavement noise (http://cait.rutgers.edu/prp/on-board-sound-intensity-obsi)

Cleaner water runoff: In recent years, PFC pavements have been found to act as filter, which significantly reduced the pollutants in runoff. Stotz and Krauth (1994) showed that PFC pavements reduced the solids in runoff by more than 50%. Additionally, PFC pavements can significantly reduce Total Kjeldahl Nitrogen (TKN), nitrate, nitrite, and dissolved heavy metals (Berbee et al. 1999; Pagotta et al. 2000; Ranchet 1995). The effect of PFC pavements on reducing solids and heavy metals in surface runoff is summarized in Table 2. Eck et al. measured the water qualify of PFC pavements for a few years and found that the PFC pavement demonstrated its capacity as a filter throughout its service life (Eck et al. 2012). Considering the findings of these completed studies, Texas Commission on Environmental Quality (TCEQ) recently approved the use of PFC mixes as a stormwater BMP in Texas on uncurbed roadways.

Table 2. Effect of PFC on reducing pollutants in surface runoff (Berbee et al. 1999; Pagotta et al. 2000; Ranchet 1995)

Heavy metal	Reduction (%)
Lead	87
Copper	62
Zinc	67
Total Kjeldahl Nitrogen (TKN)	84
Total Suspended Solids (TSS)	50~91

Admittedly, PFC pavements have some disadvantages/limitations compared with conventional HMA pavements (Arambula 2013; Cooley et al. 2009; Liu et al. 2010). First, PFC pavements usually have a service life of 6 to 10 years which is shorter than conventional HMA pavements (12~15 years). Second, PFC mixes use higher binder contents and additives, which make the cost higher than conventional HMA pavements. Third, the maintenance of the PFC pavement in snow and ice conditions is very difficult, which is the major obstacle for the wide application of PFC pavements in northern states. The high air void in the PFC pavement makes it 2 ~ 3 oF cooler than conventional HMA pavements, allowing ice to form earlier in PFC pavements. The air voids also provide room for moisture accumulation, which facilitates the ice forming in and on the pavement. The survey completed by Cooley et al. (2009) indicated that the only two northern states, Oregon and New Jersey, used PFC pavements. Even though the survey completed by Sampson in 2014 indicated a few more northern states started to use PFC pavements, the applications of PFCs are still predominantly in southern states as shown in Figure 1. Arambula (2013) surveyed PFC pavement in Texas and concluded the PFC was predominantly used in wet and warm regions of Texas as shown in Figure 7. Another maintenance concern is that clogging of the air voids in the PFC pavements has been reported, which makes the pavement lose its permeability (Alvarez et al. 2006; Cooley et al. 2009).

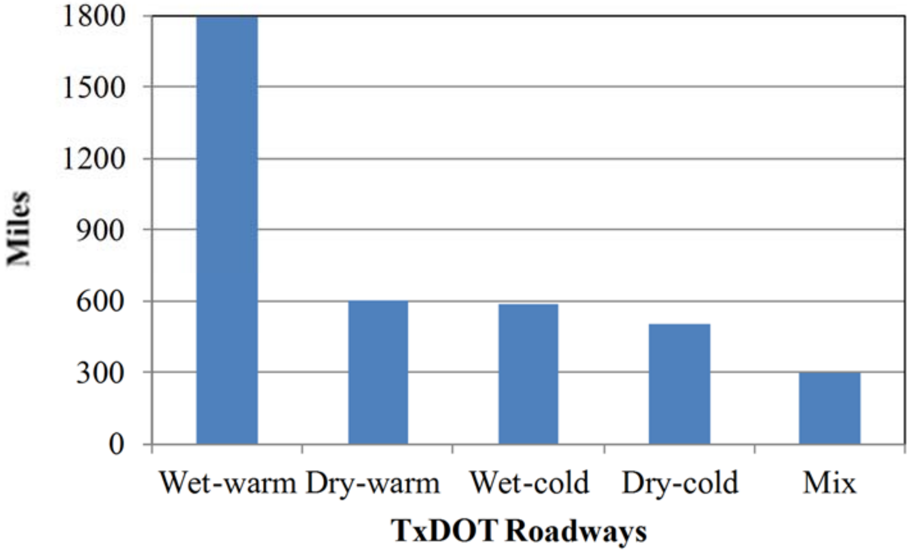

Figure 7. Usage of the PFC in different climatic regions of Texas

DESIGN AND CONSTRUCTION PFC PAVEMENTS IN TEXAS

Since its first appearance in 1970s, numerous design methods of PFC mixes have been used. Generally, they all include four primary steps including the selection of appropriate materials, determination of design aggregate gradation, selection of optimum asphalt binder content, and performance testing. In Texas, the PFC mix design is presented in Tex-204-F and material specifications are defined in Item 342 of the 2004 TxDOT Standard Specifications book. The design procedure and material requirements are summarized here in Figure 8 and Tables 3 and 4.

Step 1: Selection of Aggregates and binder according to Table 3

Step 2: Two replicate specimens [6 inch in diameter by 4.5 inch in height] at three selected asphalt contents are prepared using a Superpave Gyratory Compactor (SGC) at an N_{design} of 50

Step 3: An optimum asphalt content is then selected based on the target laboratory density specified according to Item 342 or equivalently between total AV contents of 18 and 22 %

Step 4:

- **Specimens at the optimum binder content are evaluated for draindown (Tex-235-F), moisture susceptibility (Tex-530-C), and durability (Tex-245-F) (Table 4)**

- **The durability of the optimum mixture is evaluated based on the percentage of Cantabro loss**

Figure 8. PFC mix design procedure of TxDOT

Table 3. Aggregate requirement of PFC

Sieve size	P-G 76 mixture	A-R mixture
¾”	100.0	100.0
½”	80.0-100.00	95.0-100.0
3/8”	35.0-60.0	50.0-80.0
#4	1.0-20.0	0.0-8.0
#8	1.0-10.0	0.0-4.0
#200	1.0-4.0	0.04.0
Binder content %		
	6.0-7.0	8.0-10.0

Table 4. Testing for PFCs

Test Description	Test Method
Individual % retained for sieve sized larger than #200	Tex-200-F
% passing the #200	
Laboratory-molded density, %	Tex-207-F
Binder content, %	Tex-236-F
Drain-down, %	Tex-235-F
Boil test	Tex-530-C

The Texas practice of PFC pavements is compared with the general practice of PFC pavements in the U.S in Table 5.

Table 5. Comparison of U.S. and TxDOT practice

		General practice	TxDOT practice
Applicable condition		Different pavement conditions	Only use PFC over conventional HMA pavement under good conditions
Materials	Maximum aggregate size	4.75 ~19 mm	12.5 mm
	Binder	Polymer modified PG and AR binder; Predominantly PG76-22, PG64-28	Polymer modified PG76-22, PG76-22TR and AR binder; 5.5–7.0% binder for PG-PFCs and 8.0–10.0% AR-PFCs
	Additives	Mineral or cellulose fiber, and elastomeric polymers at a dose of 0.2~0.5%	Mineral and cellulose fiber at 0.2%
Design	Structure number	Some of the states do not assign structure number to PFC layer.	Use a resilient modulus of 300 ksi (2,000 MPa)
	Thickness	Varies	Usually 1~2inches
Construction	Pavement marking	Paint, thermoplastic, epoxy	Predominantly thermoplastic
	Minimum temperature in transportation	225~350°F or 20~30°F below the job mix formula	280~350°F
	Storage time	1~12 hours	<12 hours

For the most of the states, PFCs are not given a structural value for the pavement structure design. Experience and studies did show that the PFC layer not only improved the driving safety but also contributed to the pavement structure in different ways: (1) the PFC layer increases the overall stiffness of the pavement structure; (2) the PFC layer leads to cooler temperatures in underlying pavement layers; (3) the PFC layer helps to distribute the load to a larger area. Rational consideration of the PFC's contribution to pavement structure is still an on-going research topic all over the world.

FAILURE MODES OF PFC PAVEMENTS

In 2009, Cooley et al. performed a survey to collect information about the PFC pavement practice in the U.S. as well as other counties such as Japan, Canada, and Australia (Cooley et al. 2009).

The survey disclosed that the raveling, rutting, bleeding, delamination, potholes, and clogging are the most frequent failure modes of PFC pavements. This survey outcome is consistent with the study completed by Arambula (2013) for Texas PFC pavements which revealed that raveling, bleeding, rutting and clogging are the most common failure modes, as shown in Figures 9 and 10.

Clogging is a unique failure mode of PFC pavements. When the Total Suspended Solids (TSS) and other chemicals accumulate in the air voids of PFC pavements, the permeability of the PFC will substantially decrease, which makes the pavement susceptible to moisture damage (Estakhri et al. 2008). Such a situation, though not occurring very often, can lead to severe damage to the PFC pavement if not addressed appropriately (Fwa et al. 1998). Based on the experience of TxDOT practice, the air void of the AR-PFC (see Materials, Binders in Table 5) pavements is more prone to clogging than the PG-PFC pavements, possibly due to the finer gradation and higher binder content that TxDOT specifications required.


(a)

(b)

Figure 9. Most frequent failure mode of PFC pavement in Texas (modified from Arambula et al. 2013): (a) raveling and rutting; and (b) rutting and bleeding.

Figure 10. Clogging (Estakhri et al. 2008)

PERMEABILITY/FLOW TESTS OF PFC PAVEMENTS

Isenring et al. (1990) described a field test device and procedure used in Switzerland to measure the PFC pavement's discharge/drainage capacity. TxDOT adopted and modified the method to measure water flow value (WFV), that is, the time for a given volume of water being discharge from the PFC pavement. WFV serves as an indicator of how the pavement will perform during a rain event. Figure 11 shows the device and test procedure. The details of the test can be found in Tex-246-F. At the beginning of the test, the cylindrical permeameter made of PVC with a clear pipette attached to the side is filled with water. The time that it takes to drain from the starting to the finishing lines as marked on the pipette in Figure 11 is recorded as the WFV.

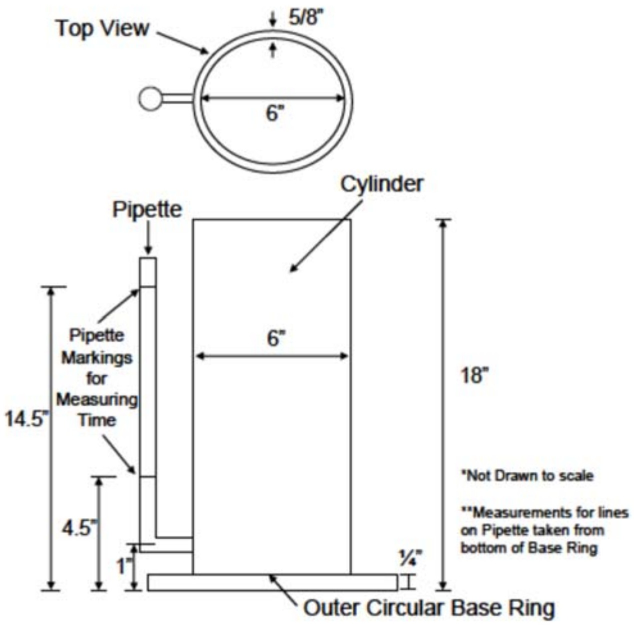

Figure 11. The WFV test device

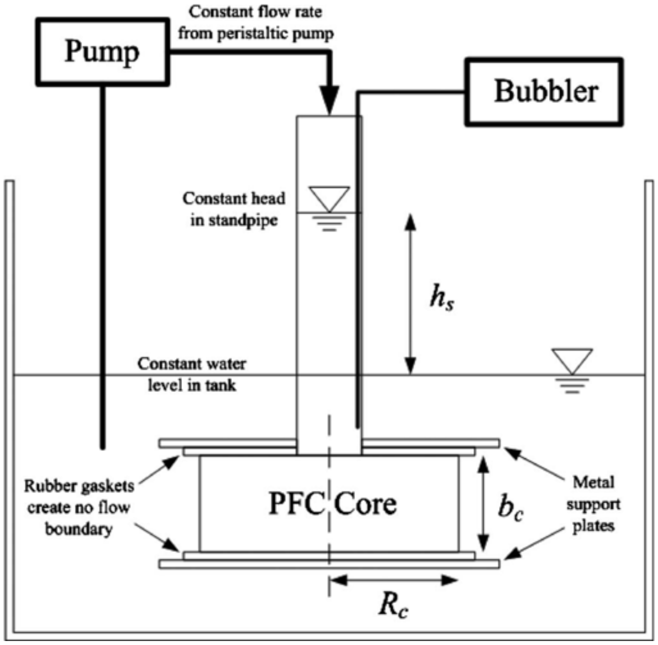

Figure 12. Permeability test of PFC mix (Charbeneau 2011)

The WFV test gives overall discharge capacity but does not provide permeability; that is usually obtained in the lab from falling and/or constant head permeability tests. For example, Figure 12 shows the constant head test apparatus used by Charbeneau (2011) to obtain the permeability of a PFC mix. Based on their analysis, Charbeneau (2011) further recommend using a falling head test in the field to determine the permeability of PFC pavements.

Tan (1999) modified the existing falling head by incorporating a pore water pressure transducer to measure the water depth inside the PFC pavements. Fwa et al. (1998) applied a similar method to test for both horizontal and vertical hydraulic conductivities of PFCs.

HYDRAULIC MODELS OF THE FLOW IN PFC PAVEMENTS

The most basic model of the flow in PFC pavements is Darcy's law, which is the most widely used to describe the linear (laminar) flow in porous medium as shown in Eq. 1 below.

$$Q = kiA \tag{1}$$

where Q is the volumetric flow rate; k is the permeability; i is the hydraulic gradient; and A is the cross-sectional area of flow.

Using the Darcy's law and considering the Dupuit-Forchheimer boundary conditions, i.e., (1) the hydraulic gradient equals the slope of the water table and is proportional to the discharge; and (2) the flow lines are only horizontal, the PFC pavement is treated as an unconfined aquifer and the flow is formulated in Eq. 2:

$$Q = \frac{k}{2}\frac{h_1^2 - h_2^2}{L} w \tag{2}$$

where h_1 and h_2 are the water levels at the entrance and exit; L is the distance between entrance and exit; w is the width.

Although being simple to use, the Dupuit equation (Eq. 2) is only applicable to linear flow, which generally does not introduce too much error when the velocity is low. The flow in PFC may become non-linear due to high hydraulic gradients. The transition between linear and non-linear flow is defined by Reynolds number (Re) as indicated in Eq. 3.

$$Re = \frac{\rho q d}{\mu} \tag{3}$$

where q is specific discharge; μ is fluid viscosity; ρ is fluid density; and d is the characteristic dimension.

The determination of d is complicated and different methods have been used to calculate d for flow in porous medium as listed in Table 6 below:

Table 6. Methods to calculate characteristic dimension

Method	Notation	References
$d = (\frac{k}{n_e})^{1/2}$	n_e – effective porosity	(Collins 1961)
$d = k^{1/2}$		(Ward 1964)
$d = d_{50}$	d_{50} – mean diameter of the flow channel in PFC	(Bear 1972)

Generally, when the Reynolds number becomes equal or greater than 100, the flow is non-linear. The Forcheimer's equation will be used to consider the non-linear flow in porous medium as shown in Eq. 4 (Charbeneau 2000; Forchheimer 1901).

$$I = \alpha q + \beta q^2 \tag{4}$$

where α and β are the two empirical coefficients.

Many researchers, such as Ergun (1952), Kovacs (1981), and Kadlec and Knight (1996), have studied α and β and found out α depended on both the properties of the porous media as well as the properties of the fluid, while β depended only on the properties of the porous media. Klenzendorf (2010) compared different methods approximating the two coefficients and found that the formulas proposed by Kadlec and Knight (1996) yielded a good agreement with the test results, which are shown in Eqs. 5 and 6 below.

$$\alpha = \frac{255\mu(1-n_e)}{\rho g n_e^{3.7} d^2} \tag{5}$$

$$\beta = \frac{2(1-n_e)}{g n_e^2 d} \tag{6}$$

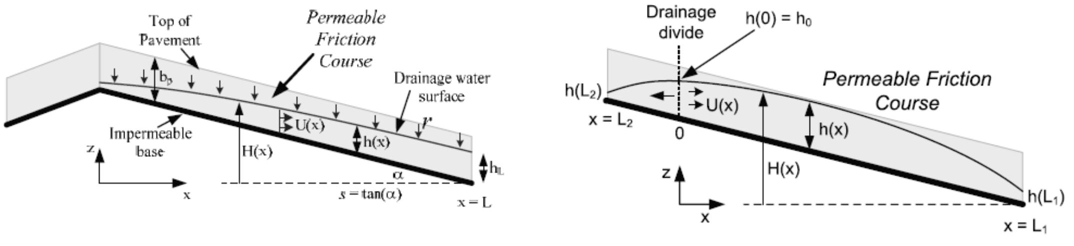

(a) (b)

Figure 13. Flow within PFC pavements: (a) unidirectional drainage; and (b) divided drainage (Charbeneau and Barrett 2008)

In addition to the estimated discharge capacity, the water depth profile is also a constant interest of researchers. Loaiciga (2005) derived the water surface based on steady Dupuit conditions. Ranieri (2002) and Charbeneau and Barrett (2008) proposed analytical solutions to describe the water surface for PFC pavement under linear flow conditions. Charbeneau and Barrett (2008) considered two situations as shown in Figure 13 and developed a series of water depth profiles for different rainfall intensities. So far all the developed water depth profiles for PFC pavements are based on the linear flow assumption and may lead to some error if the flow velocity is high.

PFC PAVEMENTS WITH UNDERDRAINS

The PFC pavements sometime are used in conjunction with underdrains to drain water faster. Jackson and Ragan (1974) studied the underdrains of the base course and examined their effects on facilitate the drainage as shown in Figure 14. Sampson (2013) completed a few small-scale laboratory tests to investigate the effect of underdrains on drainage of PFC pavements. In Sampson's test setup, the underdrains were installed directly under a PFC layer as shown in Figure 15. In the tests, the water depths within the PFC layer under different slope conditions were obtained. The test results are useful for two-dimensional flow with a uniform slope condition.

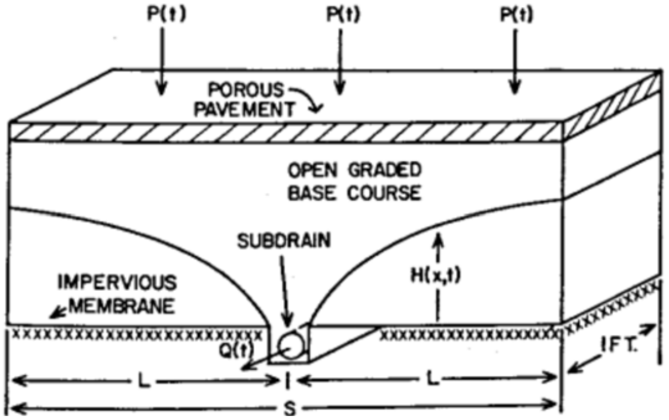

Figure 14. Underdrain underneath base course for a PFC paved park lot

Figure 15. Small-scale tests for PFC layers with underdrain (Sampson 2013)

In summary, PFC is a point of interest for many researchers; however, there is no completed large-scale study to assess the hydraulic performance of PFC pavement.

CHAPTER 3: PHYSICAL MODEL TESTS

INTRODUCTION

The TTU research team built and operated a large-scale physical model to test the use of underdrains beneath permeable friction course (PFC) to eliminate standing water on roadway surfaces. The physical model involved building pavement sections, instrumenting the sections to measure water surface within and on the PFC. The obtained physical model results were intended to calibrate a numerical model that would be used to simulate the dynamic process of infiltration, run-off and seepage under different rainfall events.

This chapter describes the construction of the physical model and its operation as well as the acquired experimental data. Summary results for different conditions are presented herein, which include the runoff depth within and on the pavement surface, the rainfall intensity and the discharge capacity for situations with and without an active underdrain.

TEST FACILITY CONSTRUCTION

Physical Model Construction

A physical model primarily consisted of a 48-feet long, 6-feet wide PFC pavement, a rainfall simulator, rain gauges, and numerous manometers. The PFC pavement was built in a 48 ×8×2 ft3 flume, which had a 2% slope in the long direction and a thickness of 2 inches. The rainfall simulator was designed to distribute rainfall across the entire model and the intensity of the rain fall was measured by the rain gauge(s). Pre-installed manometer array installed at the bottom of the PFC layer were used to measure the water depth in and on the pavement. Several totalizer gauges were to measure the water flows from the model, the drain, and leakage, and discharge from the underdrain.

Demolition of Prior Model

Figure 16 shows the prior installation, located in what is called the “Outer Flume Channel”, as it was when construction began. The Outer Flume Channel was cleared of all materials. All adhesive material on the walls and base of the channel were removed using a scraper. A pressure wash was used to ensure a clean surface for the construction of the PFC installation. Materials used to build the PFC model were plywood, various adhesives, and roofing tar. The PFC itself was the commercial product used in Sampson (2013) that was selected because (1) it has hydraulics comparable with asphaltic-based PFC, and (2) with a water-activated binder it was safe to apply indoors.

a) Prior Installation-Looking Upstream (Barnes, 2013)

b) Prior Installation-Looking Downstream (Barnes, 2013)

c) Partial Demolition of Prior Installation

d) Complete Demolition-Before Clean-Up

Figure 16. Photographs of prior installation and demolition in preparation of PFC placement

Construction of the Model

The Outer Flume Channel was water sealed using roofing tar places along the edges 8 inches up the side walls and 8 inches along the flat portion. Figure 17 is a collection of selected photographs of the sealed outer flume. Three channels, hereafter known as “Interior Flume Channels'” were placed along the length of the Outer Flume Channel. The three Interior Flume Channels consist of two smaller flume channels, of equal dimensions, on either side of a larger central flume channel. The smaller side channels were to collect leakage from the sides of the PFC as well as provide access to the underside of the model for placing and maintaining the manometers. Once the Interior Flume Channel Sections were constructed, they were placed in the Outer Flume Channel. The first Interior Flume Channel Section for each of the three Interior Flume Channels was placed at the upstream end. The side walls of each Interior Flume Channel Section were then bolted together. After a row of Interior Flume Channel Sections was in place, the next (downstream) row of Interior Flume Channel Sections was jacked into place.

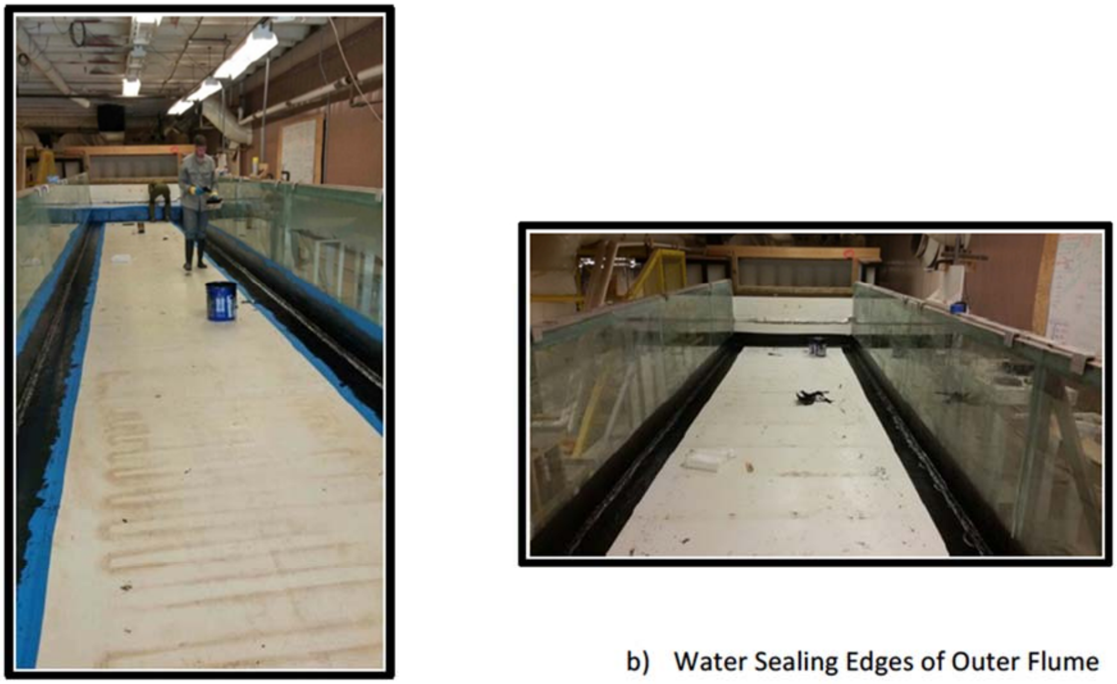

b) Water Sealing Edges of Outer Flume

a) Water Sealing Edges of Outer Flume Channel-With Painter's Tape

Figure 17. Waterproofing the outer channel

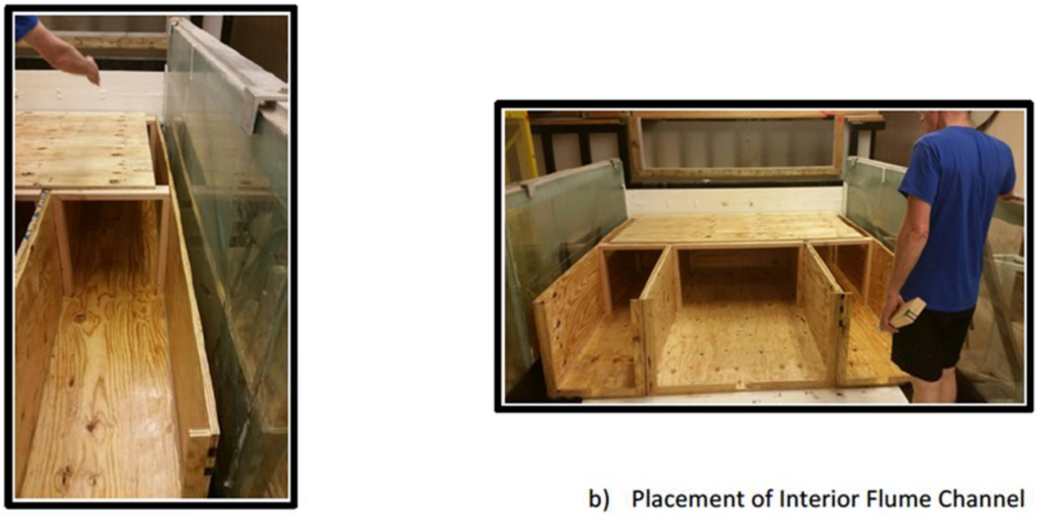

a) Placement of Interior Flume Channel Sections

b) Placement of Interior Flume Channel Upstream Row

c) Placement of Interior Flume Channel Sections

d) Bolting Together Interior Flume Channel Sections

Figure 18. Placing the inner channels

The flanges located on the end of each Interior Flume Channel Section were bolted to the flanges of the Interior Flume Channel Section located immediately downstream.

Bolting together the side walls and flanges of each Interior Flume Channel Section ensured a snug fit of the Interior Flume Channels both within the Outer Flume Channel and to one another. After all Interior Flume Channel Sections were in place and bolted together, polyurethane was used to coat all surfaces of the Interior Flume Channels. Figure 18 is a collection of photographs of the inner channel placement.

Once the Interior Flume Channel Sections were in place, the inside of the Interior Flume Channel Sections was sealed using roofing tar applied 6 inches up the side walls of the Interior Flume Channel Sections and along the entire bottom of the Interior Flume Channel Section, and to each Interior Flume Channel Section flange.

The tar was applied in two layers; the first layer has HVAC aluminum tape along the edges to make a complete water barrier, then tar was applied over the tape for the second, completion layer. Figure 19 is a collection of photographs of the inner channel system water sealed and ready for the PFC panel placement.

On top of the Interior Flume Channel Sections, a platform was constructed to hold the PFC layer, acting as an impermeable bottom. The platform has a drain slot used to accommodate the PFC underdrains. The platform was intentionally constructed so that a 6-inch gap was left on either side of the platform. This gap is intended to allow flow to travel transversely along the PFC layer to model 3D flow in the future.

The platform section frames were placed from the upstream end to the downstream end, and each platform section frame was connected to its subsequent downstream platform section frame using construction adhesive. Figure 20 is a collection of photographs of the platform frames being built, and Figure 21 is a collection of photographs of the completed platform. The underdrain slot was designed to hold a 2-inch inside diameter perforated PVC pipe, and ran laterally along the length of the installation, intentionally off-center, above the Interior Flume Channels. The underdrain's purpose was to move flow laterally along the PFC in order to facilitate increased drainage to reduce ponding and overland/sheet flow at the upper surface of the PFC. The upstream end of the Underdrain was capped and sealed, whereas the downstream end employs an open/close valve so that the PFC performance could be modeled both with an Underdrain (open), and without an Underdrain (closed). When the Underdrain is closed, the perforated PVC pipe fills completely with water, and once the drain is filled, the PFC behaves as if there is no underdrain.

a) Water Sealed Interior Flume Channels

b) Water Sealed Interior Flume Channels

c) Water Sealed Interior Flume Channels

d) Water Sealed Interior Flume Channels

Figure 19. Inner channels water sealed. Ready for the PFC panel on top

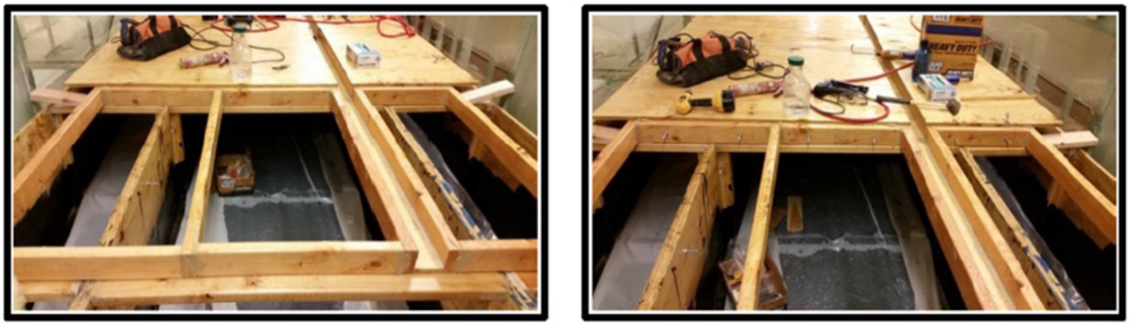

a) Platform Frame

b) Platform Frame

c) Platform Frame

d) Platform Frame

Figure 20. Platform frame building and platform panels placement. Slot is for underdrain

a) Completed Platform

b) Completed Platform

c) Completed Platform

Figure 21. Completed platform frame and panels

Figure 22 is a collection of photographs of the platform with the underdrain installed, aggregate backfill, ready for the PFC placement. Sidewalls were constructed to hold the PFC in place as it was placed and set. The sidewalls are 6 inches high and held in place with L-Brackets; the sidewalls were intentionally constructed to be removable, so that the performance of the PFC could be analyzed with the sidewalls in place and, potentially, with the sidewalls removed.

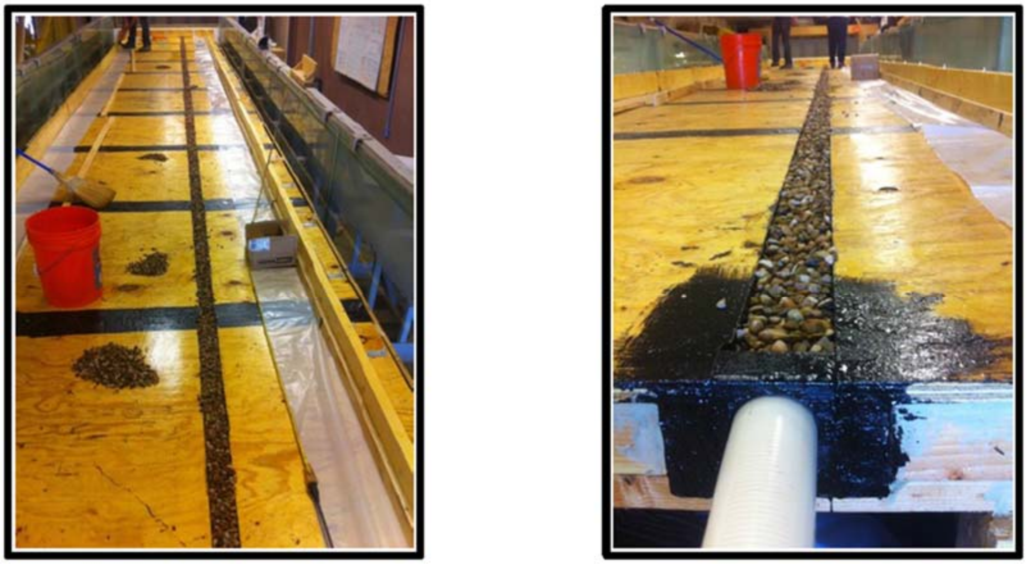

a) Underdrain Slot Backfilled with Aggregate

b) Underdrain Slot Backfilled with Aggregate

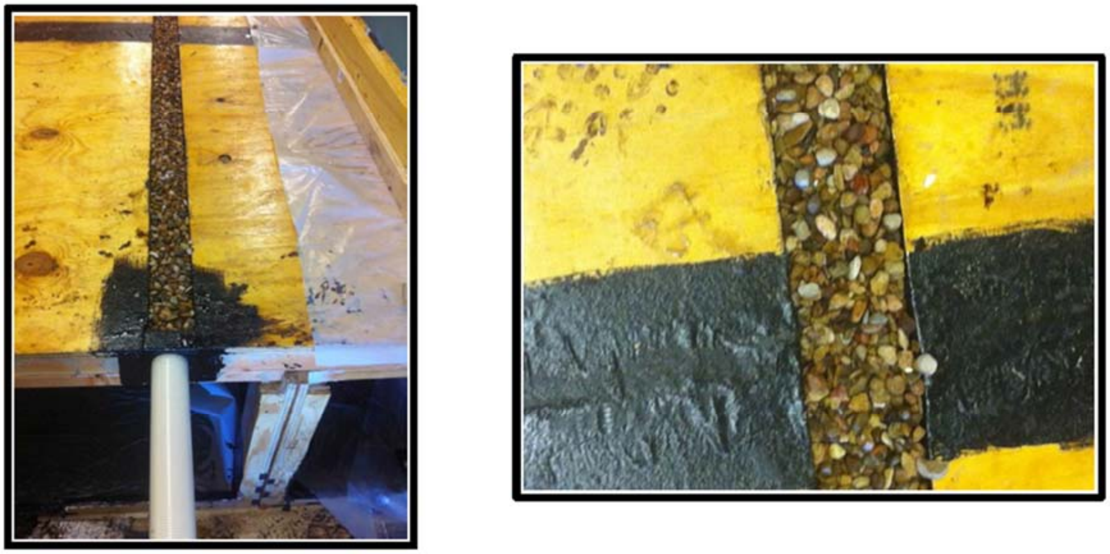

c) Underdrain Slot Backfilled with Aggregate

d) Underdrain Slot Backfilled with Aggregate

Figure 22. Underdrain installed and backfilled

Aggregate materials for the PFC mixture were delivered by the manufacturer. The PFC was mixed in the laboratory using a concrete mixer according to the manufacturer's instructions. The PFC layer was poured with a thickness of 2-3[1] inches and allowed to set overnight. The completed PFC pavement in the flume was shown in Figure 23.

a) Side Walls for PFC Pour

b) PFC Layer With Underdrain Shown

c) Full PFC Layer

Figure 23. PFC before and after placement

Manometers were installed at regular intervals along the PFC. Figure 24 is a plan view map of the locations of the Manometers along the length of the PFC layer. In the figure, flow direction was from left to right (after raining onto the PFC). Manometers were stationed at each of the 12 “banks” (vertical columns on the map).

---

[1] The placement goal was 2-inches, but portions of the PFC layer are greater than 2-inches thick. Removable guides were cut to 2 inches and stapled onto the side walls; these guides were placed as flush as possible, but there was some variability, hence the PFC surface has some variability. No formal compaction was used, although to complete the placement, plywood boards were used so the crew could walk on the rest PFC without damage.

Up to six manometers were located at each bank, at stations (horizontal rows on the map) labeled A, B, C, D, D', and E in the drawing, but later named to A, B, C, D, E, and F in the subsequent experiments (and the renamed rows are shown on the map in magenta).

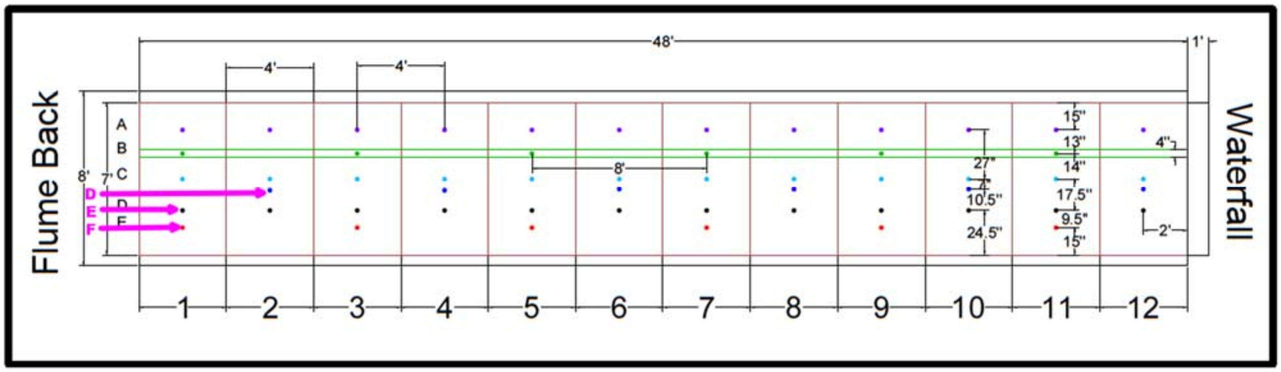

Figure 24. Manometer location map for PFC experiments

The B-station manometers were located along the underdrain channel axis, and manometers A, C, D, E, and F were located various distances away from the underdrain channel axis. All 12 banks included manometers A, C, and D, with alternating banks containing B, E, F in addition to the other manometers at that bank. The manometers were installed by drilling holes through the platform, and epoxy was used to secure the fittings into the holes. The manometer tubes were of 1/4-inch diameter, 25-foot-long, PVC tubing held in these fittings, and were used to measure water depth within the PFC layer.

Figure 25 are photographs of the manometer fittings and tubes fed to the side of the flume. The manometers feed out of the right side flume channel, and were secured to one of three manometer boards that were used to make measurements of depth within the PFC layer. Figure 26 are photographs of the manometer boards that were used to observe the water depth within the PFC during experiments.

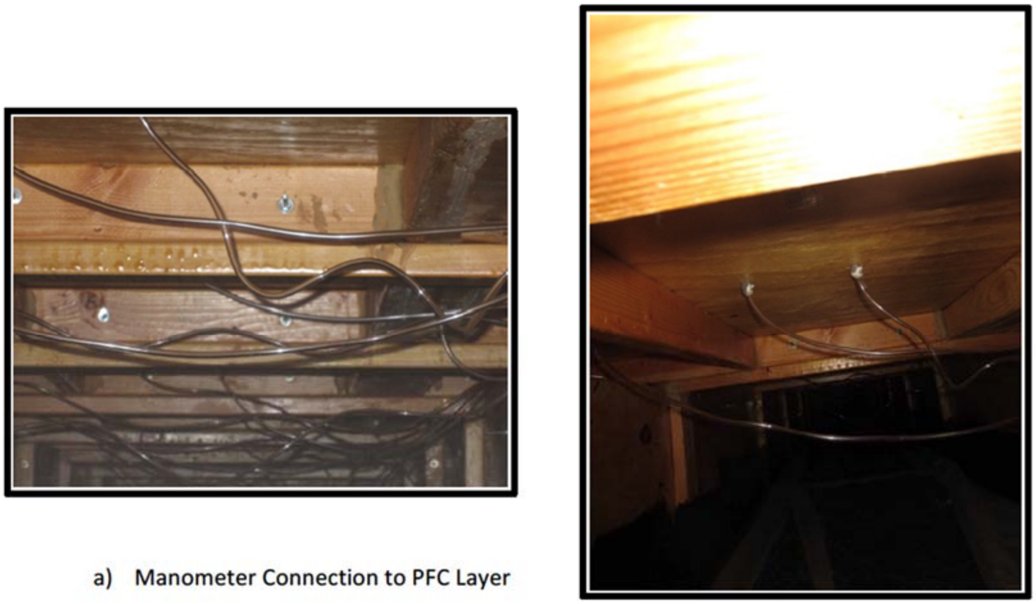

a) Manometer Connection to PFC Layer

b) Manometer Connection to PFC Layer

c) Manometer Tubes Feeding to Manometer Board

d) Manometer Tubes Feeding to Manometer Board

Figure 25. Photographs of manometer fittings and tubes

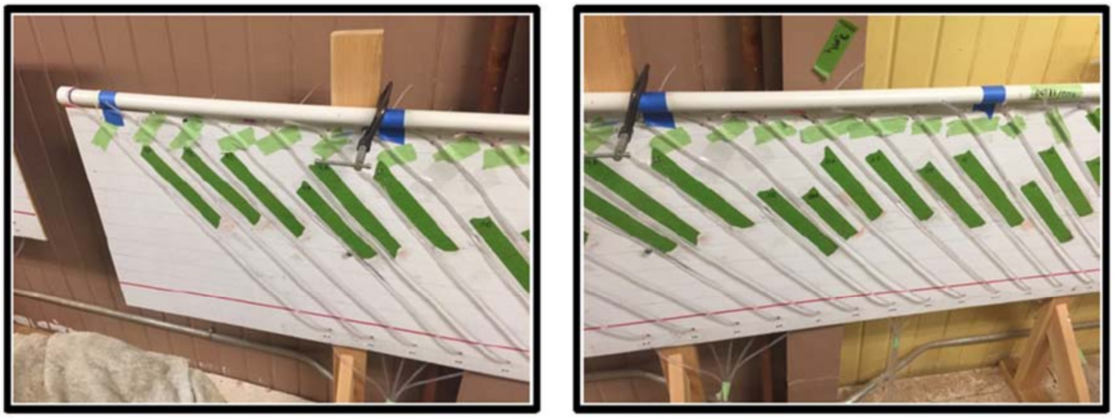

a) Manometer Board

b) Manometer Board

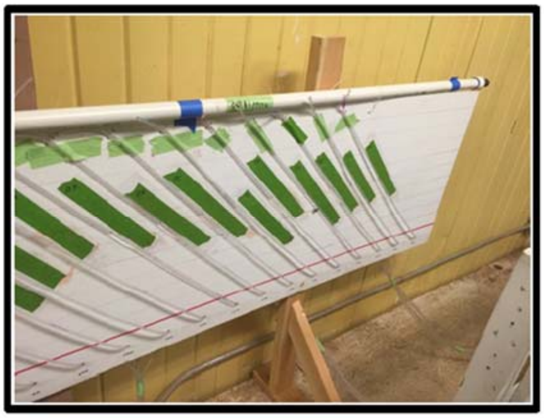

c) Manometer Board

Figure 26. Photographs of manometer read-out board(s)

A rainfall simulator, as shown in Figure 27, was fabricated to convey water from the holding tank to the PFC. The rainfall simulator is made of 1-inch diameter PVC piping, with Tee and Ell brackets used as connections and solvent welded. The PVC pipes have 1/8-inch diameter holes were drilled with 6-inch spacing to generate uniform rainfall rates along the entire length of the simulator. The rainfall simulator was assembled on top of a plywood frame and was then hoisted to a height of 5 feet above the PFC using ropes suspended from the ceiling. A frame was constructed from 2-inch by 3/4-inch plywood to hold the rainfall simulator and reduce the deformation of the PVC pipes when the rainfall simulator was filled with water. The frame is the same dimensions as the rainfall simulator, and is situated beneath the PVC piping to support the rainfall simulator. The frame is secured to the ceiling using ropes, and is connected to the rainfall simulator using Aluminum HVAC Tape at various locations along the simulator.

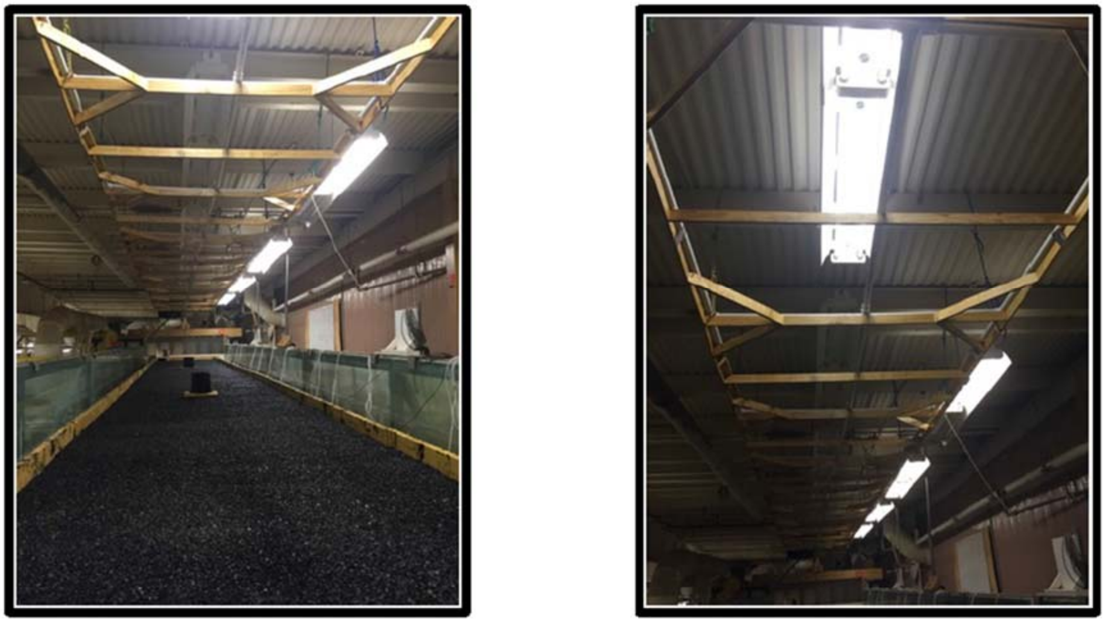

a) Rainfall Simulator with Frame

b) Rainfall Simulator with Frame

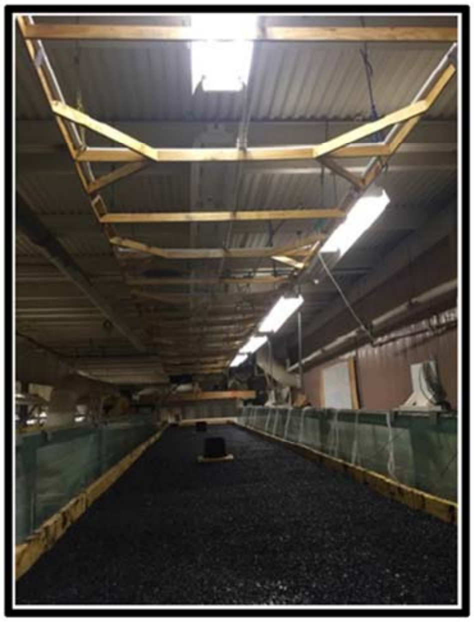

c) Rainfall Simulator with Frame

Figure 27. Photographs of rainfall simulator suspended over PFC layer

Figure 28 are photographs of an oscillator that was constructed to increase the randomization of rainfall coming from the rainfall simulator. The oscillator was connected to the rainfall simulator using a section of 2-inch by 3/4-inch plywood; the connection had an intentional weak joint at the simulator for safety - if the system became jammed, the connection would break and mechanically disconnect the motor from the frame. The oscillator rotated, and moved the rainfall simulator and frame enough to generate a pseudo-random rainfall spatial pattern thereby mimicking real-world rainfall, and preventing an uneven distribution of inflow over the model.

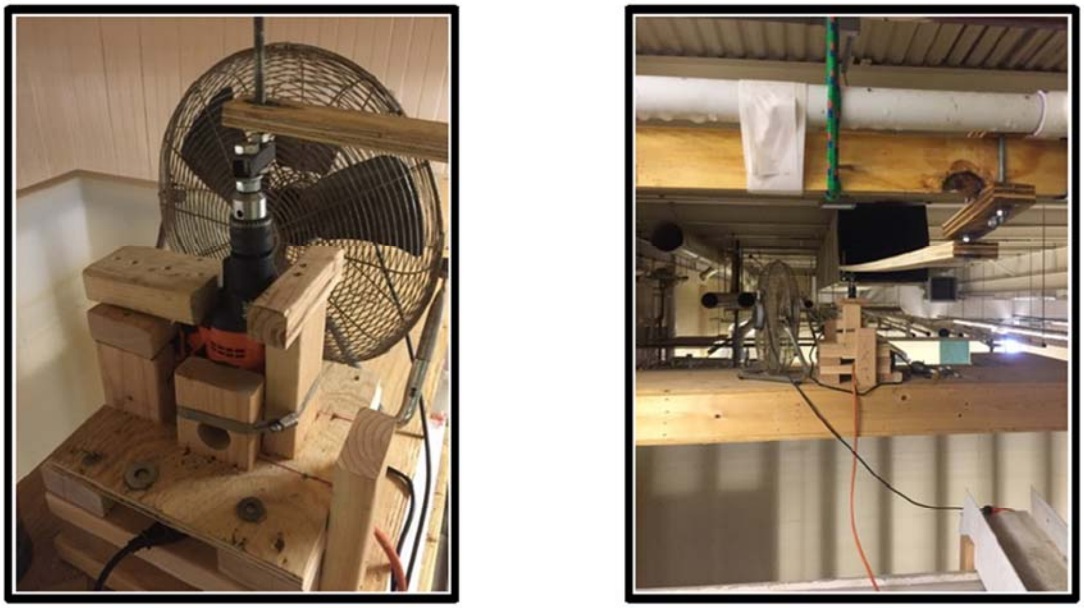

a) Oscillator

b) Oscillator Connection to Rainfall Simulator

Figure 28. Device to move (vibrate) the rainfall simulator

The rainfall simulator was supplied by one of two pump systems, depending on the desired rainfall rate. An inflow hosepipe is connected near the center of the rainfall simulator, which could be switched depending on which pump system was used for that experiment. Figure 29 were photographs of the two different pump systems as well as the central connection to the simulator. Two pump systems could be used with this simulator; a small pump system that could apply a flow rate of up to 0.4 CFS, and a medium pump that could apply a flow rate of up to 0.98 CFS. Both systems had in-line throttle valves, so flow rates could be reduced to produce more than just two rainfall rates.

These components: the pump system(s); the rainfall simulator and oscillator; PFC layer and manometer; and the support channels comprised the physical model used for the experimental studies to develop data to test the numerical model.

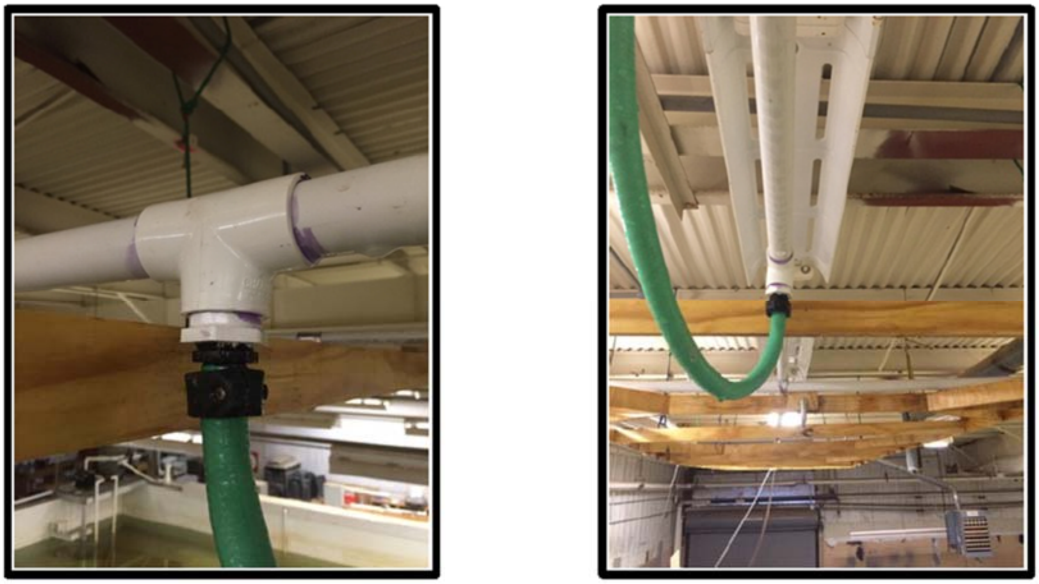

a) Inflow Connection to Rainfall Simulator

b) Inflow Connection to Rainfall Simulator

c) Small Pump System

d) Medium Pump System

Figure 29. Pump systems used to supply the rainfall simulator

MEASUREMENTS

The experimental design for the PFC and underdrain system was comprised of two distinct types of physical model configurations: (1) the first configuration was with the underdrain valve shut, effectively removing the underdrain from the model. In this configuration, all flow from precipitation must travel either over the surface, or within the porous PFC (or leak out) to the outlets; and (2) the second configuration was with the underdrain valve open; flow from precipitation could travel over the surface, through the porous PFC to the surface outlets, or through the underdrain to the subsurface outlet.

The two variables that were controllable were the rainfall intensity. Each experiment was conducted multiple times (replicates) to generate sufficient measurements for reporting arithmetic mean values and computing estimates of standard deviations. Once a series at one rainfall intensity was complete, the next series was run using different rainfall rates. The goal was to generate enough rainfall to partially flood the system. These series were conducted with the underdrain closed and open and the head values were recorded. From the head values and measured flow rates, the hydraulic performance of the PFC was quantified and can be used for further assessment.

Experimental data readings were taken at 5-minute intervals for the first 50 minutes of an experiment, and then were taken at 10-minute intervals for an additional 60 minutes for a total of 16 measurement readings. At each time step, measurements were recorded for flow rate, rainfall rate, and differential head.

DISCHARGE FROM PFC, UNDERDRAIN, AND LEAKAGE

Flow rate leaving the system was measured using a tank-type measuring device as shown in Figure 30. Polyethylene buckets were suspended below the overland outflow pipe, the underdrain outflow pipe, and a leakage slot. These buckets had outflow holes with a known area; the inside of the buckets were labeled with a depth scale from 0 to 12-inches. Flow into the bucket accumulates and eventually reaches an equilibrium level, and the water height in the bucket is used to quantify flow rate. Drainage curves for each bucket were determined both analytically and experimentally.

Figure 30. Outflow measuring assembly

Figure 31 is an excerpt of the drainage curves for the five different buckets used. Buckets would be changed if the flow rates were too large and overflowing the bucket during experiments. Similarly, for small flow rates, the buckets would be changed to try to obtain readings that were at least 1-inch depth (in some instances 1/2-inch were usable readings). The buckets were checked by measuring how long a bucket would take to deliver one liter at a given flow rate and comparing that result to the tabulated reading in the figure. In all these cases, the readings were consistent with the measured time so the bucket curves were deemed reliable.

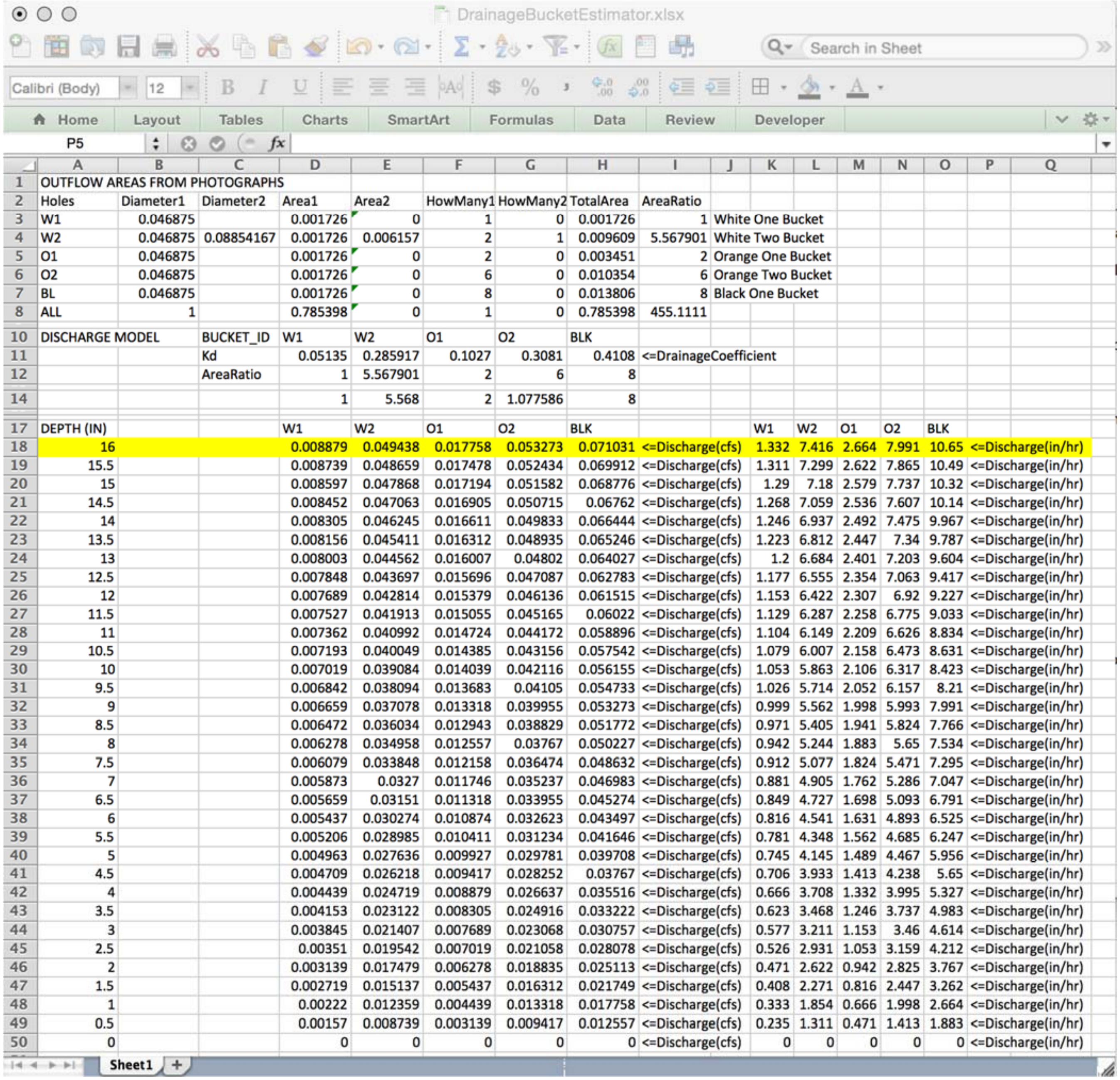

	A	B	C	D	E	F	G	H	I	J	K	L	M	N	O	P	Q
1	OUTFLOW AREAS FROM PHOTOGRAPHS																
2	Holes	Diameter1	Diameter2	Area1	Area2	HowMany1	HowMany2	TotalArea	AreaRatio								
3	W1	0.046875		0.001726	0	1	0	0.001726	1	White One Bucket							
4	W2	0.046875	0.08854167	0.001726	0.006157	2	1	0.009609	5.567901	White Two Bucket							
5	O1	0.046875		0.001726	0	2	0	0.003451	2	Orange One Bucket							
6	O2	0.046875		0.001726	0	6	0	0.010354	6	Orange Two Bucket							
7	BL	0.046875		0.001726	0	8	0	0.013806	8	Black One Bucket							
8	ALL	1		0.785398	0	1	0	0.785398	455.1111								
10	DISCHARGE MODEL		BUCKET_ID	W1	W2	O1	O2	BLK									
11			Kd	0.05135	0.285917	0.1027	0.3081	0.4108	<=DrainageCoefficient								
12			AreaRatio	1	5.567901	2	6	8									
14				1	5.568	2	1.077586	8									
17	DEPTH (IN)			W1	W2	O1	O2	BLK			W1	W2	O1	O2	BLK		
18	16			0.008879	0.049438	0.017758	0.053273	0.071031	<=Discharge(cfs)		1.332	7.416	2.664	7.991	10.65	<=Discharge(in/hr)	
19	15.5			0.008739	0.048659	0.017478	0.052434	0.069912	<=Discharge(cfs)		1.311	7.299	2.622	7.865	10.49	<=Discharge(in/hr)	
20	15			0.008597	0.047868	0.017194	0.051582	0.068776	<=Discharge(cfs)		1.29	7.18	2.579	7.737	10.32	<=Discharge(in/hr)	
21	14.5			0.008452	0.047063	0.016905	0.050715	0.06762	<=Discharge(cfs)		1.268	7.059	2.536	7.607	10.14	<=Discharge(in/hr)	
22	14			0.008305	0.046245	0.016611	0.049833	0.066444	<=Discharge(cfs)		1.246	6.937	2.492	7.475	9.967	<=Discharge(in/hr)	
23	13.5			0.008156	0.045411	0.016312	0.048935	0.065246	<=Discharge(cfs)		1.223	6.812	2.447	7.34	9.787	<=Discharge(in/hr)	
24	13			0.008003	0.044562	0.016007	0.04802	0.064027	<=Discharge(cfs)		1.2	6.684	2.401	7.203	9.604	<=Discharge(in/hr)	
25	12.5			0.007848	0.043697	0.015696	0.047087	0.062783	<=Discharge(cfs)		1.177	6.555	2.354	7.063	9.417	<=Discharge(in/hr)	
26	12			0.007689	0.042814	0.015379	0.046136	0.061515	<=Discharge(cfs)		1.153	6.422	2.307	6.92	9.227	<=Discharge(in/hr)	
27	11.5			0.007527	0.041913	0.015055	0.045165	0.06022	<=Discharge(cfs)		1.129	6.287	2.258	6.775	9.033	<=Discharge(in/hr)	
28	11			0.007362	0.040992	0.014724	0.044172	0.058896	<=Discharge(cfs)		1.104	6.149	2.209	6.626	8.834	<=Discharge(in/hr)	
29	10.5			0.007193	0.040049	0.014385	0.043156	0.057542	<=Discharge(cfs)		1.079	6.007	2.158	6.473	8.631	<=Discharge(in/hr)	
30	10			0.007019	0.039084	0.014039	0.042116	0.056155	<=Discharge(cfs)		1.053	5.863	2.106	6.317	8.423	<=Discharge(in/hr)	
31	9.5			0.006842	0.038094	0.013683	0.04105	0.054733	<=Discharge(cfs)		1.026	5.714	2.052	6.157	8.21	<=Discharge(in/hr)	
32	9			0.006659	0.037078	0.013318	0.039955	0.053273	<=Discharge(cfs)		0.999	5.562	1.998	5.993	7.991	<=Discharge(in/hr)	
33	8.5			0.006472	0.036034	0.012943	0.038829	0.051772	<=Discharge(cfs)		0.971	5.405	1.941	5.824	7.766	<=Discharge(in/hr)	
34	8			0.006278	0.034958	0.012557	0.03767	0.050227	<=Discharge(cfs)		0.942	5.244	1.883	5.65	7.534	<=Discharge(in/hr)	
35	7.5			0.006079	0.033848	0.012158	0.036474	0.048632	<=Discharge(cfs)		0.912	5.077	1.824	5.471	7.295	<=Discharge(in/hr)	
36	7			0.005873	0.0327	0.011746	0.035237	0.046983	<=Discharge(cfs)		0.881	4.905	1.762	5.286	7.047	<=Discharge(in/hr)	
37	6.5			0.005659	0.03151	0.011318	0.033955	0.045274	<=Discharge(cfs)		0.849	4.727	1.698	5.093	6.791	<=Discharge(in/hr)	
38	6			0.005437	0.030274	0.010874	0.032623	0.043497	<=Discharge(cfs)		0.816	4.541	1.631	4.893	6.525	<=Discharge(in/hr)	
39	5.5			0.005206	0.028985	0.010411	0.031234	0.041646	<=Discharge(cfs)		0.781	4.348	1.562	4.685	6.247	<=Discharge(in/hr)	
40	5			0.004963	0.027636	0.009927	0.029781	0.039708	<=Discharge(cfs)		0.745	4.145	1.489	4.467	5.956	<=Discharge(in/hr)	
41	4.5			0.004709	0.026218	0.009417	0.028252	0.03767	<=Discharge(cfs)		0.706	3.933	1.413	4.238	5.65	<=Discharge(in/hr)	
42	4			0.004439	0.024719	0.008879	0.026637	0.035516	<=Discharge(cfs)		0.666	3.708	1.332	3.995	5.327	<=Discharge(in/hr)	
43	3.5			0.004153	0.023122	0.008305	0.024916	0.033222	<=Discharge(cfs)		0.623	3.468	1.246	3.737	4.983	<=Discharge(in/hr)	
44	3			0.003845	0.021407	0.007689	0.023068	0.030757	<=Discharge(cfs)		0.577	3.211	1.153	3.46	4.614	<=Discharge(in/hr)	
45	2.5			0.00351	0.019542	0.007019	0.021058	0.028078	<=Discharge(cfs)		0.526	2.931	1.053	3.159	4.212	<=Discharge(in/hr)	
46	2			0.003139	0.017479	0.006278	0.018835	0.025113	<=Discharge(cfs)		0.471	2.622	0.942	2.825	3.767	<=Discharge(in/hr)	
47	1.5			0.002719	0.015137	0.005437	0.016312	0.021749	<=Discharge(cfs)		0.408	2.271	0.816	2.447	3.262	<=Discharge(in/hr)	
48	1			0.00222	0.012359	0.004439	0.013318	0.017758	<=Discharge(cfs)		0.333	1.854	0.666	1.998	2.664	<=Discharge(in/hr)	
49	0.5			0.00157	0.008739	0.003139	0.009417	0.012557	<=Discharge(cfs)		0.235	1.311	0.471	1.413	1.883	<=Discharge(in/hr)	
50	0			0	0	0	0	0	<=Discharge(cfs)		0	0	0	0	0	<=Discharge(in/hr)	

Figure 31. Drainage curves for measurement buckets

PRECIPITATION INTENSITY

The rainfall intensity was measured by using two rain gauges, located at two positions along the length of the installation. These rain gauges were moved to a new location for each experiment. Rain gauge readings were recorded at regular intervals during the experiment, and were used to compute rainfall rates. Figure 32 are photographs of the rain gages, a typical placement, and the readouts.

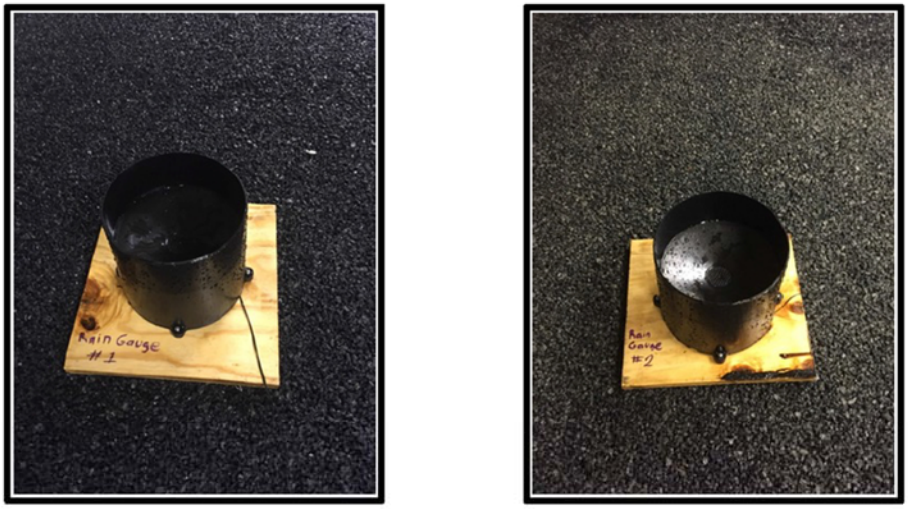

a) Rain Gauge #1

b) Rain Gauge #2

d) Rain Gauge Displays

c) Rain Gauges Located on PFC Layer

Figure 32. Rain gauges and readouts used

FLOW DEPTH WITHIN AND ON PFC

Differential head readings were measured using manometers located along the PFC layer. The water level in each manometer was marked on the manometer board using dry erase markers. Because of the large number of manometers utilized in this research project, an average mark time was used for each time step. The mark time start indicated when the user began marking the manometer levels, and the mark time end indicated when the user finished marking the manometer levels. An average mark time was calculated for that reading and was taken as the time recording for that reading. Average mark times were 5 minutes apart for the first 10 readings, and were 10 minutes apart for the following 6 readings.

A camera was used to photograph the 16 different readings of each manometer, and the images were used for interpretation and analysis. The images were imported into Adobe Acrobat Pro and, after adjusting the scale of the photograph, measurement tools within Acrobat Pro were used to measure the change in distance between a specified zero point and each reading for all manometers. These changes in manometer level measurements were then input into an Excel Spreadsheet designed to convert the measurements into the appropriate form. The analysis of the manometer readings was done after experiments had been completed.

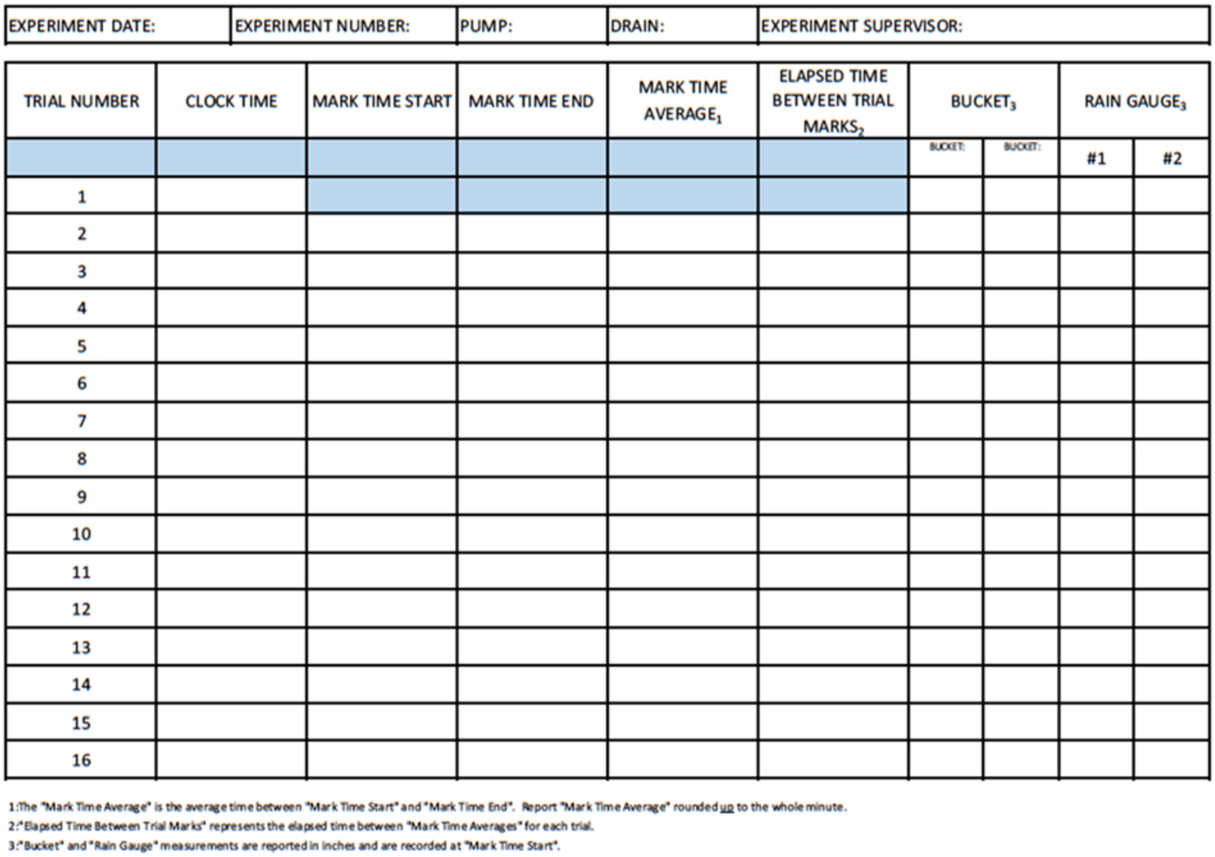

EXPERIMENT DATE:	EXPERIMENT NUMBER:	PUMP:	DRAIN:	EXPERIMENT SUPERVISOR:

TRIAL NUMBER	CLOCK TIME	MARK TIME START	MARK TIME END	MARK TIME AVERAGE$_1$	ELAPSED TIME BETWEEN TRIAL MARKS$_2$	BUCKET$_3$		RAIN GAUGE$_3$	
						BUCKET:	BUCKET:	#1	#2
1									
2									
3									
4									
5									
6									
7									
8									
9									
10									
11									
12									
13									
14									
15									
16									

1:The "Mark Time Average" is the average time between "Mark Time Start" and "Mark Time End". Report "Mark Time Average" rounded <u>up</u> to the whole minute.
2:"Elapsed Time Between Trial Marks" represents the elapsed time between "Mark Time Averages" for each trial.
3:"Bucket" and "Rain Gauge" measurements are reported in inches and are recorded at "Mark Time Start".

Figure 33. Experiment data sheet used during experiments to record times, bucket depths, and rain gage cumulative depths

The flow depth on PFC is measured using a ruler to determine the depth above the PFC that flow occurs. These measurements are made close to the nearest manometers where possible.

Figure 33 is the in-laboratory data sheet that was developed after the 3rd experiment and used to record measurement times, rain gage readings, and flow readings for the PFC and underdrain.

EXPERIMENT CONDITIONS AND DATA MANAGEMENT

Table 7 is a list of the experimental conditions in terms of rainfall conditions and whether the underdrain was open or closed. The closed underdrain situation was used to mimic the PFC pavement without underdrain, which provided baseline data for comparison to manifest the effectiveness of the underdrain. Most experiments had unique dates so the date was used as the experiment ID. In some instances, two experiments were conducted in a single day, and these were labeled as DATE-1, DATE-2, and so on. Table 8 is a list of the experiments conducted to date, with remarks regarding each experiment. In July, the researchers added the ability to measure leakage after considerable efforts to stop leaks. Experiments from July onward had good quantification of leakage and were used to estimate leakage rates in the earlier experiments.

Table 7. Experiment Configuration Summary

RAIN_ID	DRAIN_ID	REMARKS
Small	Closed	Experiment Count = 13. Leaks measured = 3. Remainder estimated.
Medium	Closed	Experiment Count = 9. Leaks measured = 3. Remainder estimated.
Large	Closed	Experiment Count = 4. Leaks measured = 2. Remainder estimated.
Small	Open	Experiment Count = 4. Leaks measured =3. Remainder estimated.
Medium	Open	Experiment Count = 7. Leaks measured = 4. Remainder estimated.
Large	Open	Experiment Count = 4. Leaks measured = 2. Remainder estimated.
		Total Experiment Count = 41.

Table 8. Individual Experiment Configurations

COUNT	EXP_ID	RAIN	DRAIN	REMARKS
1	04-03-2016	Small	Closed	Method develop
2	04-08-2016	Small	Closed	Need flow measure tool
3	04-13-2016-1	Small	Closed	Bucket test
4	04-13-2016-2	Small	Closed	Created lab sheet for data management
5	04-20-2016	Small	Closed	Short run; pump broke
6	04-22-2016	Small	Closed	Leak Estimated
7	04-25-2016	Small	Closed	Leak Estimated
8	05-02-2016	Small	Closed	Leak Estimated
9	05-04-2016	Small	Closed	Leak Estimated
10	05-18-2016	Small	Closed	Leak Estimated
11	05-26-2016-1	Medium	Closed	Leak Estimated
12	05-25-2016-2	Medium	Closed	Leak Estimated
13	05-26-2016	Medium	Closed	Leak Estimated
14	05-31-2016	Medium	Closed	Leak Estimated
15	06-01-2016	Medium	Open	Leak Estimated
16	06-03-2016-1	Medium	Open	Leak Estimated
17	06-03-2016-2	Medium	Closed	Leak Estimated
18	06-04-2016	Medium	Open	Leak Estimated
19	06-11-2016	Small	Closed	Leak Estimated
20	07-05-2016	Large	Open	Leak Measured
21	07-06-2016	Large	Closed	Leak Measured
22	07-08-2016	Large	Open	Leak Measured
23	07-18-2016	Large	Closed	Leak Measured
24	07-19-2016	Large	Open	Leak Measured
25	07-20-2016	Large	Closed	Leak Measured
26	07-27-2016	Medium	Closed	Leak Measured
27	07-28-2016	Medium	Open	Leak Measured
28	07-29-2016	Medium	Closed	Leak Measured
29	08-02-2016	Medium	Open	Leak Measured
30	08-03-2016	Medium	Closed	Leak Measured
31	08-04-2016	Medium	Open	Leak Measured
32	08-09-2016	Small	Closed	Leak Measured
33	08-10-2016	Small	Open	Leak Measured
34	08-11-2016	Small	Closed	Leak Measured
35	08-15-2016	Small	Open	Leak Measured
36	08-16-2016	Small	Closed	Leak Measured
37	08-17-2016	Small	Open	Leak Measured
38	08-23-2016-1	Large	Closed	Leak Measured
39	08-23-2016-2	Large	Open	Leak Measured

COUNT	EXP_ID	RAIN	DRAIN	REMARKS
40	08-23-2016-3	Medium	Closed	Leak Measured
41	08-23-2016-4	Medium	Open	Leak Measured

EXPERIMENTAL RESULTS

The experimental results are summarized in Tables 9 – 10; Table 9 is a summary of collective results for different experimental configurations, while Table 10 lists the individual experiments.

Table 9. Arithmetic Mean Values for Experimental Conditions (Summary)

RAIN	Rain-Value	DRAIN	Drain-Value	PFC-Value	Leak-Value
Small	1.55 in/hr	Closed	0.00 in/hr	1.21 in/hr	0.28 in/hr
Medium	5.63 in/hr	Closed	0.00 in/hr	5.01 in/hr	0.54 in/hr
Large	6.15 in/hr	Closed	0.00 in/hr	5.48 in/hr	0.66 in/hr
Small	2.35 in/hr	Open	1.50 in/hr	0.70 in/hr	0.12 in/hr
Medium	5.77 in/hr	Open	2.97 in/hr	2.47 in/hr	0.35 in/hr
Large	6.07 in/hr	Open	4.83 in/hr	0.91 in/hr	0.32 in/hr

The summary table indicates that the Medium and Large rainfall values are repeatable regardless of the valve setting (an anticipated result). The Small Rain, Closed Valve results contained experiments that were part of the apparatus "learning curve".[2] The leakage rates were smaller by almost a factor of two when the underdrain is active.[3]

Not quantified in the tables was the observation that downstream end would have ponded (overland flow) water over the last 4 to 6 feet of the model for the Medium and Large Rain, with the drain closed. The flow depths were quite small, about 1/4 inch. The water depth at the "curb" end of the model was approximately equal to the thickness of the PFC, decreasing to 3/4 inches at the drain holes in the model.

Table 10 lists equilibrium results (the system came to equilibrium quite fast, the table shows values after nearly an hour of operation). The various columns in the table, in order, are:

COUNT = the serial count.

EXP_ID = the experiment ID code.

---

[2] These early experiments contribute to the difference in rainfall rates for the Small Rain results. As the experimenter's skills improved the repeatability improved.

[3] The result is unanticipated, but explainable. When the drain valve is closed the heads in the drainage channel are greater, and any leaks in this region are subject to greater driving force, hence the greater rate. Similarly anywhere away from the drainage channel the heads would also be larger, again providing greater driving force for leakage.}

RAIN-RAW = the raw rainfall as reported by the rain gages.[4]

RAIN-ADJ = the adjusted rainfall.

Q-LEAK = the measured or estimated leakage.

Q-PFC = the measured flow through the permeable friction course.

Q-DRAIN = the measured flow through the under-drain when it was active.

Q-TOTAL = the sum of the outflows.

All units in Table 10 are inches-per-hour. The flows measured in cubic feet per second were converted into inches per hour assuming the contributing area to the flow measurements is an area 48-feet long and 7-feet wide.

SUMMARY

A large-scale model of a PFC layer on top of an impermeable base was constructed and tested for its drainage under rainfall intensities of ~2.00 inches/hour, ~ 5.70 inches/hour, and ~ 6.11 inches/hour. Although leakage was detected during the tests, the mass balance was acceptable after correcting for leakage and over-reporting of the rain gauges and the total outflow from the model was reasonably close to the input rates.

---

[4] The rain gages over-report the catch, even when moved around on the PFC. The researchers recorded the catch and then adjusted based on an analysis of the total outflows (mass balance)

Table 10. Rainfall Input and Measured Flow Rates at Equilibrium

COUNT	EXP_ID	RAIN-RAW	RAIN-ADJ	Q-LEAK	Q-PFC	Q-DRAIN	Q-TOTAL
1	04-03-2016	1.57	0.54	0.25	0.53	0.00	0.78
2	04-08-2016	2.04	0.70	0.26	0.50	0.00	0.76
3	04-13-2016-1	4.00	1.37	0.28	0.55	0.00	0.83
4	04-13-2016-2	2.83	0.97	0.26	0.58	0.00	0.84
5	04-20-2016	7.57	2.60	0.33	1.33	0.00	1.66
6	04-22-2016	7.57	2.60	0.33	1.70	0.00	2.03
7	04-25-2016	7.54	2.60	0.33	1.70	0.00	2.03
8	05-02-2016	6.16	2.12	0.31	1.56	0.00	1.87
9	05-04-2016	6.37	2.19	0.31	1.56	0.00	1.87
10	05-18-2016	3.91	1.35	0.28	1.56	0.00	1.84
11	05-26-2016-1	18.07	5.84	0.57	4.73	0.00	5.30
12	05-25-2016-2	19.78	6.39	0.62	4.73	0.00	5.35
13	05-26-2016	18.20	5.88	0.58	5.08	0.00	5.66
14	05-31-2016	17.71	5.72	0.57	4.90	0.00	5.47
15	06-01-2016	17.62	5.88	0.35	0.33	4.90	5.58
16	06-03-2016-1	16.28	5.44	0.33	0.23	4.90	5.46
17	06-03-2016-2	16.86	5.45	0.54	4.73	0.00	5.27
18	06-04-2016	16.91	5.65	0.34	0.23	4.73	5.30
19	06-11-2016	4.25	1.46	0.13	0.23	1.85	2.21
20	07-05-2016	14.03	5.26	0.12	0.23	4.54	4.89
21	07-06-2016	14.70	5.48	0.47	5.33	0.00	5.80
22	07-08-2016	16.51	6.19	0.47	1.33	3.93	5.73
23	07-18-2016	16.53	6.17	1.15	5.33	0.00	6.48
24	07-19-2016	15.02	5.63	0.24	0.67	4.90	5.81
25	07-20-2016	16.44	6.13	0.47	5.33	0.00	5.80
26	07-27-2016	16.98	5.49	0.53	4.15	0.00	4.68
27	07-28-2016	16.70	5.58	0.33	4.90	0.23	5.46
28	07-29-2016	13.56	4.38	0.47	4.73	0.00	5.20
29	08-02-2016	16.26	5.43	0.33	5.08	0.23	5.64
30	08-03-2016	15.86	5.12	0.47	5.08	0.00	5.55
31	08-04-2016	15.92	5.32	0.33	5.08	0.47	5.88
32	08-09-2016	3.50	1.20	0.33	1.41	0.00	1.74
33	08-10-2016	2.29	2.47	0.12	1.85	0.47	2.44
34	08-11-2016	3.14	1.08	0.24	1.41	0.00	1.65
35	08-15-2016	2.07	2.11	0.12	0.24	1.85	2.21
36	08-16-2016	2.53	0.87	0.24	1.33	0.00	1.57
37	08-17-2016	2.45	2.50	0.12	0.47	1.85	2.44
38	08-23-2016-1	18.31	6.83	0.58	5.96	0.00	6.54
39	08-23-2016-2	19.26	7.22	0.47	1.41	5.96	7.84
40	08-23-2016-3	19.78	6.39	0.58	6.92	0.00	7.50
41	08-23-2016-4	21.33	7.12	0.41	1.41	5.33	7.15

CHAPTER 4: NUMERICAL SIMULATION

INTRODUCTION

This chapter explains the details of a developed computing algorithm of numerical model called "pfc_DF_Richards", which simulates the hydraulic behavior of permeable friction course (PFC). In addition, the mathematical background of the numerical model, the numerical schemes as well as the calibration are also discussed herein.

The first part describes the mathematical framework, within which the governing equations used in the computational model for both surface and subsurface component Then the numerical schemes including mesh generation and discretization for both surface and subsurface domains are included in the second part. The third part further discusses about the convergence criteria and coupling algorithm. Thereafter, the calibration of parameters in the numerical model is presented based on the experiments data. This chapter also includes the large-scale laboratory testing to determine the permeability of the PFC for various void ratios.

NUMERICAL MODEL

The developed numerical model couples the surface and subsurface flow based on the continuity of mass and conservation of momentum in the fluid mechanics. The subsurface domain is simulated by the three dimensional (3D) Richards equation. Due to the nature of thin layer on the PFC surface, the vertical component of flow velocity is treated uniform and the surface domain can be modeled by the shallow water equations (SWE). The framework of the numerical model is described as follows.

Equations for Surface Flow

The surface flow, i.e., the flow on PFC surface, can be described by 2-D shallow water equation (SWE), which is derived from the simplified Navier-Stokes equations. By assuming the pressure is hydrostatic ($\partial p = \rho g \partial h$) and neglecting the momentum of rainfall. The complete version of the equation is (Liu et al. 2016):

$$\frac{\partial h}{\partial t} + \nabla \cdot (\boldsymbol{u} h) = q_I + q_R \qquad (7)$$

$$\frac{\partial \boldsymbol{u}}{\partial t} + \nabla \cdot (\boldsymbol{u}\boldsymbol{u}) = g \nabla h - g(S_o - S_f) \qquad (8)$$

where h = Flow depth [m];

$\boldsymbol{u}$ = depth-averaged velocity vector (u, v), [m/s];

q_I = infiltration (-) /exfiltration (+) rate [m^2/s];

q_R = rainfall intensity [m/hr];

S_o = bottom slope [-], which equals to bed slope vector ∇z;

z = bottom elevation of PFC [m]

S_f = friction slope [-]

By adopting the diffusive wave approximation that the inertial terms are less than the pressure, gravity and friction terms, Eqn. 8 can be reduced to

$$0 = g\nabla h - g(S_o - S_f) \tag{9}$$

The friction slope S_f is typically calculated by Manning's equation:

$$S_f = \frac{n^2|\boldsymbol{u}|\boldsymbol{u}}{h^{4/3}} \tag{10}$$

where n is the Manning's roughness parameter.

By combining Eqns. 9 and 10, the depth averaged velocity ***u*** can be calculated by

$$u = -\frac{h^{2/3}}{n}\frac{\nabla H}{|\nabla H|^{1/2}} \tag{11}$$

where H (= $h + z$) is the total pressure head.

Equations for Subsurface Flow

Subsurface flow in porous media, i.e., the flow within PFC, is modeled by the 3-D Richards equation. This equation is derived from the combination of Darcy's law and mass conservation equation. The mixed-form Richards equation, which includes both water content (θ) and the water pressure head (h), is implemented in this numerical model (Richards 1931; Szymkiewicz 2012):

$$\frac{\partial\theta(h)}{\partial t} = \nabla \cdot [K_s k_r(h) \cdot \nabla(h + z)] + q_s \tag{12}$$

where $\theta(h)$ = moisture content [-];

h = pressure head [m];

z = bottom elevation [m];

$k_r(\theta)$ = relative hydraulic conductivity, which is a second-order tensor

K_s= saturated hydraulic conductivity [m/s]

q_s = volumetric source/sink term

The van Genuchten model is used for the constitutive relation of moisture content $\theta(h)$ and relative hydraulic conductivity $k_r(\theta)$ (van Genuchten 1980):

$$\theta(h) = \begin{cases} \theta_r + \frac{\theta_s - \theta_r}{[1+(\alpha|h|)^n]^m} \; if \; h < 0 \\ \theta_s \; otherwise \end{cases} \tag{13}$$

$$k_r(\theta) = \frac{K}{K_s} = \left(\frac{\theta-\theta_r}{\theta_s-\theta_r}\right)^{0.5} \left\{1 - \left[1 - \left(\frac{\theta-\theta_r}{\theta_s-\theta_r}\right)^{1/m}\right]^m\right\}^2 \tag{14}$$

In the above equations, α and n are the parameters determined by the shape of the soil water characteristic curves, and m = 1-1/n.

FINITE VOLUME DISCRETIZATION

The purpose of discretization includes producing computational meshes on which the governing equations are solved and transforming the governing equations into a matrix. The numerical model was implemented in the OpenFOAM, which was an open source toolbox that can be used to build customized solvers for solving partial differential equations (PDEs) using finite volume method (FVM) on structured and unstructured meshes (Weller et al. 1998) .

The FVM divides the solution domain into a finite number of contiguous control volumes (CVs) and then integrate the PDEs in each CV. The advantages of this method includes conservation of basic quantities such as mass and momentum, applicable to both steady-state and transient state, and systems of partial differential equations are solved at one time (Jasak 1996).

Mesh Generation

The physical model built in Texas Tech University (TTU) is used to calibrate the numerical model. The physical model primarily includs 48-feet long and 6-feet wide with 2-inch PFC, rain simulator, and various gauges. The sketch of the physical model is shown in Figure 34.

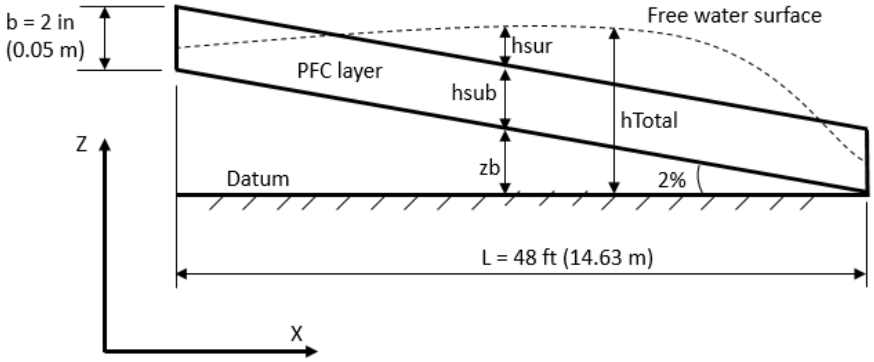

Figure 34. Sketch for the physical model and its variables

In the computational model, two geometries were created as shown in Figure 35. The geometry at the bottom, as subsurface domain, is created as the same dimension as physical PFC model and used to simulate the water movement inside the PFC, on which the Richards equation [Eqn. 12] will be solved, while the top geometry, as surface domain, is used to simulate the rainfall and free surface water, on which the Richards equation [Eqn. 7] will be solved.

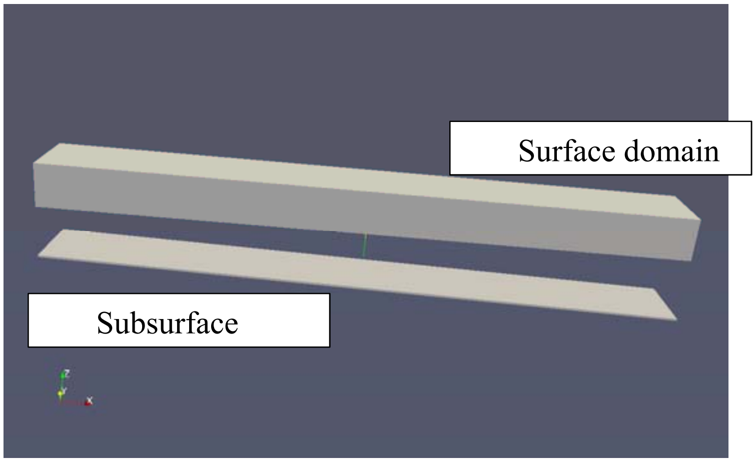

Figure 35. Geometries for surface domain (top) and subsurface domain (bottom)

To simulate the water depth when the underdrain pipe is turned on during the rainfall event (Figure 36a), a mixed boundary condition called "seepageFaceHead" was implemented. This boundary condition included both fixed value and fixed gradient boundary conditions, more details would be explained later on in this chapter (Figure 36b).

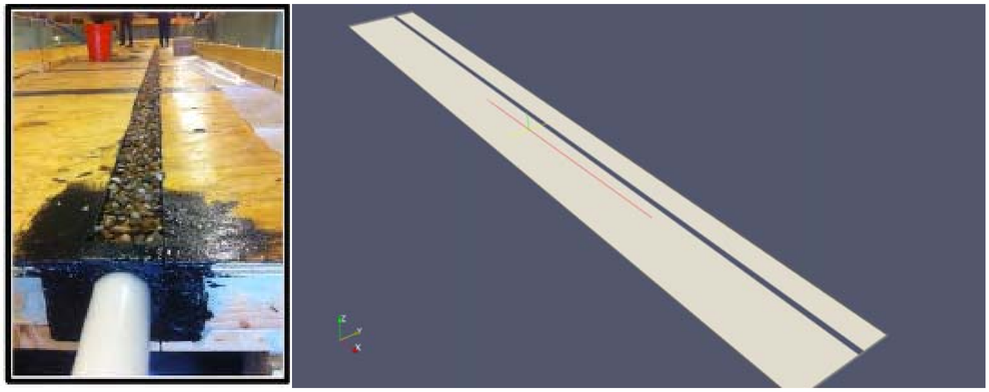
(a) (b)

Figure 36. Physical and numerical model of underdrain: a) underdrain slot in physical model b) underdrain in numerical model

To use the FVM, the generated domains were required to be discretized into control volumes (CVs), on which the governing equations can be solved. A typical control volume is bounded by a set of flat faces, as shown in Figure 37, and each face is shared with only one neighboring CV and does not overlap with other control volumes. The computational point P was the centroid of the control volume so that:

$$\int_{V_p} (x - x_P)\, dV = 0 \qquad (15)$$

The cell faces could have two groups as internal faces that were connecting two control volumes and boundary faces that restricted the boundaries of the domain. The face area vector S_f was always pointed from lower index cell to higher index cell.

In the simulating model, the surface and the subsurface domain was discretized into appropriate number of cells to ensure computational accuracy and efficiency. The mesh structures were shown in Figures 38 and 39, respectively.

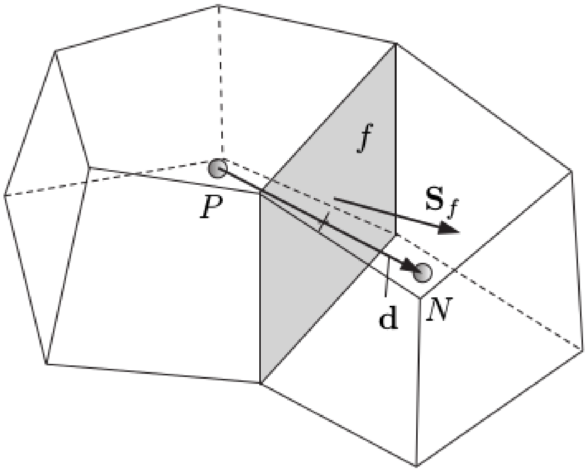

Figure 37. A typical control volume and its parameters (OpenFoam 2014)

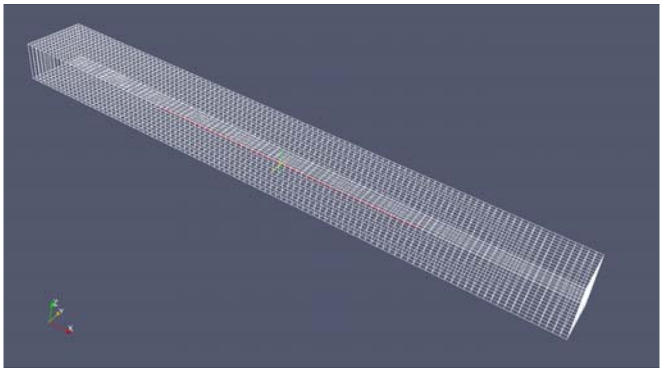

Figure 38. The mesh structure for surface domain

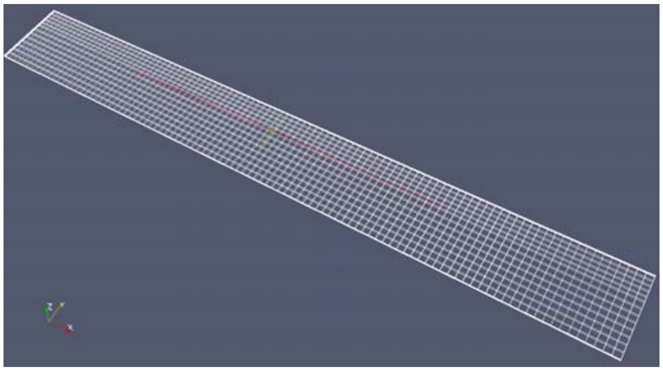

Figure 39. The mesh structure for subsurface domain

Discretization of Shallow Water Equation

Integrating the shallow water equation Eqn. 7 over the control volume V_p, we will have

$$\int_{V_p} \frac{\partial h}{\partial t} dV + \int_{V_p} \nabla \cdot (\boldsymbol{u}h)\, dV = \int_{V_p} q_I\, dV + \int_{V_p} q_R\, dV \tag{16}$$

The Gauss' theorem transfers the volume integration to face integration, and can be interpreted as the following equation:

$$\int_{V_p} \nabla \cdot \boldsymbol{a}\, dV = \int_{\partial V_p} \boldsymbol{a} \cdot dS \tag{17}$$

where ∂V is the closed surface bounding the control volume V_p, and dS represents an finitesimal surface element with associated outward pointing normal on ∂V.

So the convection term in Eqn. 17 can be written as

$$\int_{V_p} \nabla \cdot (\boldsymbol{u}h)\, dV = \int_{\partial V_p} (\boldsymbol{u}h) \cdot dS = \sum_f (\boldsymbol{u}h)_f \cdot S_f \tag{18}$$

And Eqn. 16 turns to

$$\frac{h_i^{N+1} - h_i^N}{\Delta t} V_p + \sum_f (\boldsymbol{u}h)_f \cdot S_f = q_{I,i} V_p + q_{R,i} V_p \tag{19}$$

where N + 1= next time step;

N = current time step;

S_f = the face area vector;

Δt = time step size [s].

Subscript *f* implied the value of the variable on the corresponding face center, which are interpolated from the values of surrounding cells centers.

Two different types of boundary conditions (B.C.) are implemented in the surface domain: fixed value and fixed gradient. The fixed value was specifying a fixed water depth on a boundary. This type of boundary condition is used to set the depth averaged velocity as $u \cdot n = \sqrt{gh}$ when the surface flow leaving the outlet boundary. The fixed gradient was used to impose flux. For example, a zerogradient B.C. corresponded to $\nabla(h + z) = 0$ and it was used at the impermeable walls as the surface flow cannot penetrate them and flux doesn't change.

Discretization of Richards Equation

Eqn. 12 is also a nonlinear equation due to the advection term $K_s k_r(h) \cdot \nabla(h + z)$. In the numerical model, it was solved iteratively by using fixed Picard iterations since it is very difficult to get the direct solution. The equation can be semi-discretized as the following equation (Liu 2012)

$$\frac{\theta^{n+1,m+1} - \theta^{n}}{\Delta t} = \nabla \cdot [K_s k_r(h) \cdot \nabla(h^{n+1,m+1} + z)] + q_s^{n+1} \qquad (20)$$

where n + 1 = current time step in iteration;

n = previous time step in iteration;

m + 1 = current Picard iteration level;

m = previous Picard iteration level.

According to Taylor series equation, the water content $\theta^{n+1,m+1}$ can be written as:

$$\theta^{n+1,m+1} \approx \theta^{n+1,m} + \left(\frac{d\theta}{dh}\right)^{n+1,m} (h^{n+1,m+1} - h^{n+1,m}) \qquad (21)$$

Substituting Eqn. 21 in to Eqn. 20

$$\left(\frac{d\theta}{dh}\right)^{n+1,m} \frac{h^{n+1,m+1} - h^{n+1,m}}{\Delta t} = \nabla \cdot [K_s k_r(h) \cdot \nabla(h^{n+1,m+1} + z)] + S \qquad (22)$$

where $\underline{S}$ is new source term and needs to be updated at each iteration level, and has the form

$$S = q_s^{n+1} + \frac{\theta^n - \theta^{n+1,m}}{\Delta t} \tag{23}$$

Then spatial terms in Eqn. 22 were discretized by OpenFOAM and the differential operators were assembled automatically.

Fixed value and fixed gradient boundary conditions were also implemented for Richards equation, which included fixed head h or fixed total head h+z, specified flux q.

The fixed head h or fixed total head h+z is used to define the water table locations and the shape of water bodies. In math, they are defined on the boundary faces as:

$$h = h_D(x, y, z, t) \tag{24}$$

and

$$h + z = h_D(x, y, z, t) \tag{25}$$

where h_D is head distribution function, and x, y, z are the coordinates of boundary face center.

The above two conditions can be generalized into a single boundary condition as

$$h = h_G(x, y, z, t) \tag{26}$$

In the finite volume method, the hydraulic gradient on boundary faces $(\nabla h)_f$, which was required for the Laplacian term in Richards equation, was calculated by

$$S_f \cdot (\nabla h)_f = |S_f| \frac{h_G - h_P}{|d|} \tag{27}$$

where h_G = general function related to x, y, z, t.

h_P = pressure head h at the center of boundary cell

The specified flux q can be written as

$$q_c(x,y,z,t) = -\frac{S_f}{|S_f|}[K_s k_r \cdot \nabla(h+z)] \tag{28}$$

The pressure gradient can be calculated as

$$\frac{S_f}{|S_f|} \cdot \nabla h = -\frac{S_f}{|S_f|} \cdot \nabla z - \frac{q_c(x,y,z,t)}{K_s k_r} \tag{29}$$

And the value of water pressure at the center of boundary face h_f can be calculated as

$$h_f = h_p - \frac{S_f}{|S_f|} \cdot \nabla h|d| \tag{30}$$

where h_p = the value of water pressure at the center of boundary cell

$|d|$ = the distance from the center of boundary cell to the center of boundary face.

SOLUTION CONTROL OF DISCRETIZED EQUATIONS

Surface flow

Eqn. 19 can be written as

$$\frac{h_i^{N+1} - h_i^N}{\Delta t} + \frac{1}{V_p}\sum_f F = q_{I,i} + q_{R,i} \tag{31}$$

where *F* is the total flux of quantity *h* crossing a face, and $F = (\boldsymbol{u}h)_f \cdot S_f$.

The term $(\boldsymbol{u}h)_f$, which is the value on the faces between two cells, were evaluated by using first-order accurate but bounded upwind scheme (UP) or second-order accurate but unbounded central difference scheme (CD).

To achieve both accuracy and boundedness, Eqn. 31 is solved by using the method called multidimensional universal limiter with explicit solution (MULES), which was already implemented as built-in module in OpenFOAM (OpenFoam 2014). The MULES adopted the flux corrected transport (FCT) algorithms (Kuzmin et al. 2003; Zalesak 1979) which used values at both higher-order and lower-order to predict the final solutions.

Consider in 1-D grid, as shown in Figure 40.

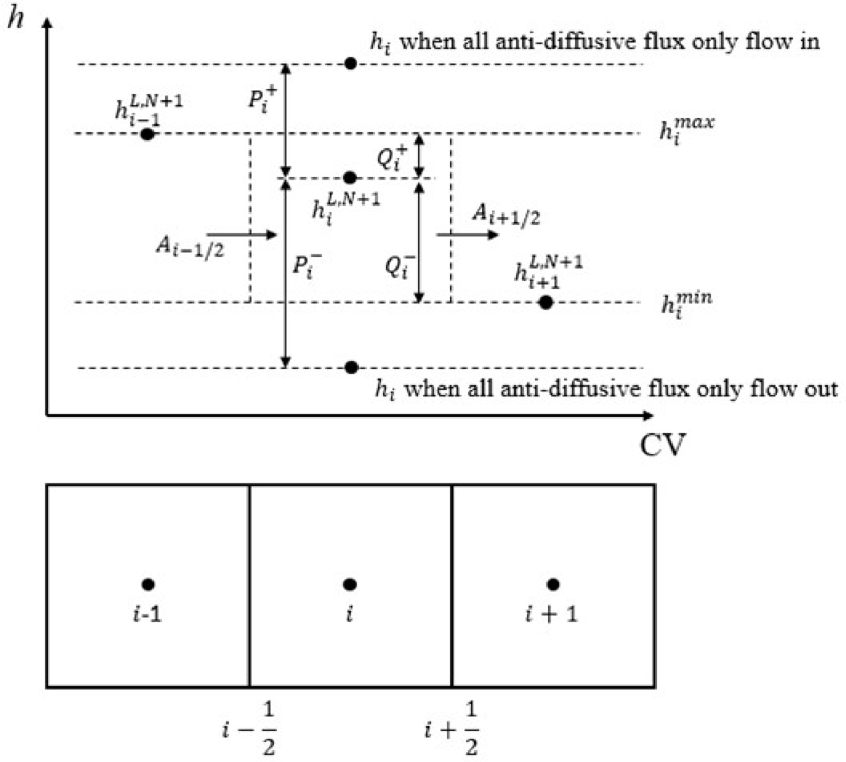

Figure 40. 1-D geometry and magnitudes for Zalesak's limiter (Kuzmin et al. 2003)

On the control volume (CV) i, Eqn. 31 can be rearranged as

$$h_i^{N+1} = h_i^N - \frac{\Delta t}{V_p}\left(F_{i+1/2}^N - F_{i-1/2}^N\right) + \Delta t(q_I + q_R) \tag{32}$$

The MULES procedure is listed as follows (Liu et al. 2016; Zalesak 1979):

(1) Compute the flux with a lower order scheme, $F_{i+1/2}^{L,N}$, $F_{i-1/2}^{L,N}$;

(2) Compute the flux with a higher order scheme, $F_{i+1/2}^{H,N}$, $F_{i-1/2}^{H,N}$;

(3) Calculate the "anti-diffusive flux", $A_{i+1/2}^N = F_{i+1/2}^{H,N} - F_{i+1/2}^{L,N}$, $A_{i-1/2}^N = F_{i-1/2}^{H,N} - F_{i-1/2}^{L,N}$;

(4) Compute the h_i^{N+1} with a lower order scheme,

$$h_i^{L,N+1} = h_i^N - \frac{\Delta t}{V_p}\left(F_{i+1/2}^{L,N} - F_{i-1/2}^{L,N}\right) + \Delta t(q_I + q_R) \tag{33}$$

(5) For term $A_{i+1/2}^N$, constrain it by the limiter $\lambda_{i+1/2}$ as

$$A_{i+1/2}^{C,N} = \lambda_{i+1/2} A_{i+1/2}^N \left(0 \le \lambda_{i+1/2} \le 1\right) \tag{34}$$

So that the final solution h_i^{N+1} was bounded between some maximum value h_i^{max} and some minimum value h_i^{min}, where

$$\begin{aligned} h_i^a &= \max\left(h_i^N, h_i^{L,N+1}\right) \\ h_i^{max} &= \max(h_{i-1}^a, h_i^a, h_{i+1}^a) \end{aligned} \tag{35}$$

and

$$\begin{aligned} h_i^b &= \min\left(h_i^N, h_i^{L,N+1}\right) \\ h_i^{min} &= \min\left(h_{i-1}^b, h_i^b, h_{i+1}^b\right) \end{aligned} \tag{36}$$

(6) The solution can be computed by

$$\begin{aligned} h_i^{N+1} &= h_i^N - \frac{\Delta t}{V_p}\left[\left(F_{i+1/2}^{L,N} + A_{i+1/2}^{C,N}\right) - \left(F_{i-1/2}^{L,N} + A_{i-1/2}^{C,N}\right)\right] + \Delta t(q_I + q_R) \\ &= h_i^{L,N+1} - \frac{\Delta t}{V_p}\left(A_{i+1/2}^{C,N} - A_{i-1/2}^{C,N}\right) \end{aligned} \tag{37}$$

To determine the limiter $\lambda_{i+1/2}$ in step (5), for example, we defined six quantities as:

$$\begin{aligned} P_i^+ &= \text{The sum of antidiffusive fluxes when all are flowing into CV } i \\ &= \max\left(0, A_{i-1/2}^N\right) - \min\left(0, A_{i+1/2}^N\right) \end{aligned} \tag{38}$$

$$Q_i^+ = \frac{V_p}{\Delta t}\left(h_i^{max} - h_i^{L,N+1}\right) \tag{39}$$

$$\lambda_i^+ = \begin{cases} \min\left(1, \dfrac{Q_i^+}{P_i^+}\right), (P_i^+ > 0) \\ 0, (P_i^+ = 0) \end{cases} \tag{40}$$

$$\begin{aligned} P_i^- &= \text{The sum of anti} - \text{diffusive fluxes when all of them are flowing away CV } i \\ &= \max\left(0, A_{i+1/2}^N\right) - \min\left(0, A_{i-1/2}^N\right) \end{aligned} \tag{41}$$

$$Q_i^- = \frac{V_p}{\Delta t}\left(h_i^{L,N+1} - h_i^{min}\right) \tag{42}$$

$$\lambda_i^- = \begin{cases} \min\left(1, \frac{Q_i^-}{P_i^-}\right), (P_i^+ > 0) \\ 0, (P_i^+ = 0) \end{cases} \tag{43}$$

As the anti-diffusive fluxes which leaving one CV would enter its neighbor through the shared face, then $\lambda_{i+1/2}$ can be determined by

$$\lambda_{i+1/2} = \begin{cases} \min(\lambda_{i+1}^+, \lambda_i^-), if\ A_{i+1/2}^N \geq 0 \\ \min(\lambda_i^+, \lambda_{i+1}^-), if\ A_{i+1/2}^N < 0 \end{cases} \tag{44}$$

The implementation of MULES for solving SWE in OpenFOAM is shown below:

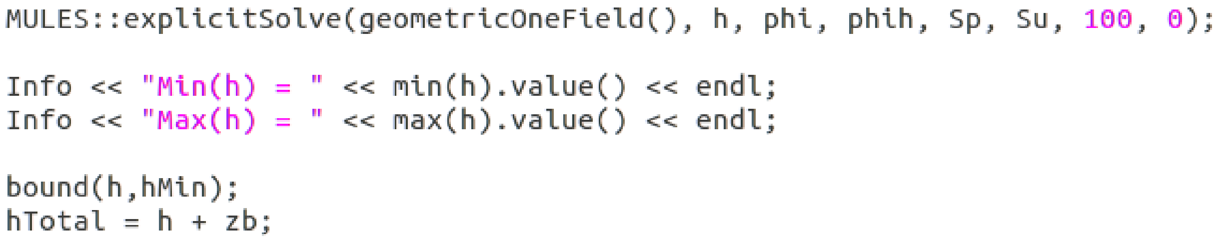

```
MULES::explicitSolve(geometricOneField(), h, phi, phih, Sp, Su, 100, 0);

Info << "Min(h) = " << min(h).value() << endl;
Info << "Max(h) = " << max(h).value() << endl;

bound(h,hMin);
hTotal = h + zb;
```

Figure 41. MULES implementation in pfc_DF_Richards

Subsurface flow

(a) Convergence criteria for Picard iteration

As Picard iteration proceeded in a time step, specific criteria were needed so that the iteration can stop when convergence requirement is met and moved to the next time step. There are three convergence criterion implemented in this numerical model, including standard criteria, mixed criteria and moisture content criteria (Huang et al. 1996; Liu 2012).

The standard criterion compares a user defined tolerance h_t with the discrepancy of pressure head between two successive iterations $|h^{n+1,m+1} - h^{n+1,m}|$, and stops the iteration when

$$|h^{n+1,m+1} - h^{n+1,m}| < \Delta h \tag{45}$$

But the disadvantage is that Δh is empirical to different users, and small value may need huge computational resources though it can improve the accuracy.

The mixed criterion is suggested as the upgraded version of standard criteria. By introducing a relative error δ_r which usually varies from 0.001 to 0.1, the mixed criteria can be written as

$$|h^{n+1,m+1} - h^{n+1,m}| < \Delta h + \delta_r |h^{n+1,m+1}| \tag{46}$$

This criterion can improve the speed of convergence since δ_r acts as relax factor, but the accuracy is reduced when moisture content changes rapidly.

The convergence criterion based on the moisture content is proposed as

$$|\theta^{n+1,m+1} - \theta^{n}| \leq \Delta\theta \tag{47}$$

Research (Huang et al. 1996) shows that the moisture content criterion is more efficient and accurate for simulating saturated flow while the rest two criterions can also produce good result if the number is set appropriately.

In our simulation, the standard criterion is used and h_t is set as10^{-3}, and the implementation in OpenFOAM is listed as below:

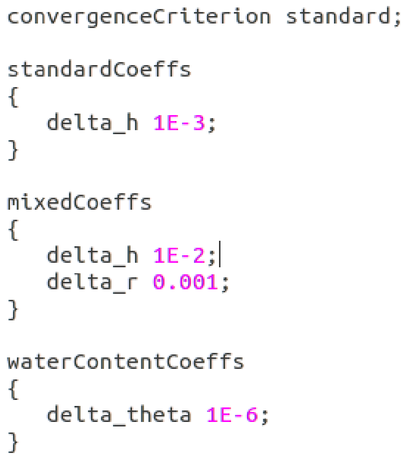

```
convergenceCriterion standard;

standardCoeffs
{
   delta_h 1E-3;
}

mixedCoeffs
{
   delta_h 1E-2;
   delta_r 0.001;
}

waterContentCoeffs
{
   delta_theta 1E-6;
}
```

Figure 42. Implementation for convergence criteria in pfc_DF_Richards

(b) Solution of linear equation system

After discretizing the governing equation on a control volume (CV), we can get a linear equation for that CV as:

$$a_P h_P + \sum_N a_N h_N = b_p \tag{48}$$

where a_P, h_P are the coefficient and variable for the calculated CV, a_N, h_N are the coefficients and variables for neighbor CVs, and b_p is the source terms and contributions from the boundary conditions. Assembling the linear equations for all CVs will give us a system of algebraic equations as:

$$[A][h] = [b] \tag{49}$$

where [A] is sparse matrix with a_P on the diagonal and a_N off the diagonal, [h] is the unknow pressure head at each cell center, [b] is the source vector.

To solve the leaner system Eqn. 49, OpenFOAM has four built-in linear solvers for users as preconditioned conjugate gradient (PCG), generalized geometric-algebraic multi-grid (GAMG), solver using a smoother (smoothSolver) and Diagonal solver for explicit systems (diagnoal).

To make the linear solver converge faster, preconditioners can be applied to the original symmetric matrix. The choice of preconditioners includes Diagonal incomplete-Cholesky (DIC), Faster Diagonal incomplete-Cholesky (FDIC) (OpenFoam 2014).

The implementation of linear solver for Eqn. 49 in OpenFOAM is listed in Figure 3.4, preconditioned conjugate gradient (PCG) is used as the linear solver with tolerance at 10^{-6}, and the preconditioner is Diagonal incomplete-Cholesky (DIC).

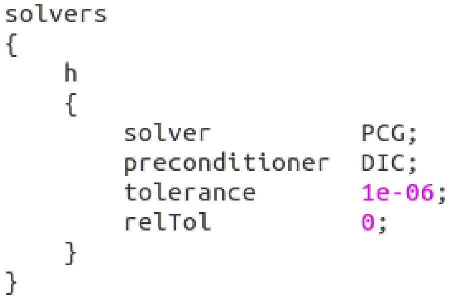

```
solvers
{
    h
    {
        solver          PCG;
        preconditioner  DIC;
        tolerance       1e-06;
        relTol          0;
    }
}
```

Figure 43. Solution control in pfc_DF_Richards

COUPLING ALGORITHM

The coupling between surface and subsurface domain was fulfilled by the Dirichlet-Neumann partitioning method (Liu et al. 2016), which is a boundary condition including both fixed value and fixed gradient.

The working flow and the coupling algorithm are shown in Figures 44 and 45. It is composed by two inner iterations for surface flow and subsurface flow individually, and one outer iteration between the two domains. During each time step, the shallow water equation [Eqn. 7] is first solved by predefined boundary conditions and the MULES iteration. The water head solution h form Eqn. (1.1) is then imposed as a fixed value boundary condition to the subsurface domain. Next, the Richards equation [Eqn. (1.6)] is solved by Picard iteration with the updated water head condition and yields a flux through the top boundary. This flux acted as a fixed gradient boundary condition and is imposed to the surface domain as infiltration and exfiltration. This step iterated until the changes of water head h and water flux at the interface is less than 10-6 m and 10-6 m3/s respectively between two successive steps.

In order to ensure the water depth on the surface is positive, additional limitations to infiltration rate is required. Eqn. 19 can be discretized as

$$\frac{h^{N+1}}{\Delta t} = {q_I}^{N+1} + {q_R}^{N+1} - \nabla \cdot (\boldsymbol{u}h^N) + \frac{h^N}{\Delta t} \geq 0 \tag{50}$$

And the infiltration rate ${q_I}^{N+1}$ is required as

$$q_{I_{bound}}^{N+1} \geq -\frac{h^N}{\Delta t} - {q_R}^{N+1} + \nabla \cdot (\boldsymbol{u}h^N) \tag{51}$$

To determine whether the water can flow into PFC, another parameter called infiltration capacity I_p is calculated on the top boundary of subsurface domain as

$$I_p \geq -K_s \nabla (h + z) \tag{52}$$

If the $q_{I_{bound}}^{N+1}$ from the surface domain is less than I_p, then the PFC is unsaturated which means water can flow into PFC. Otherwise, the PFC is saturated and the pressure head h on its top boundary is set to the water depth on the surface.

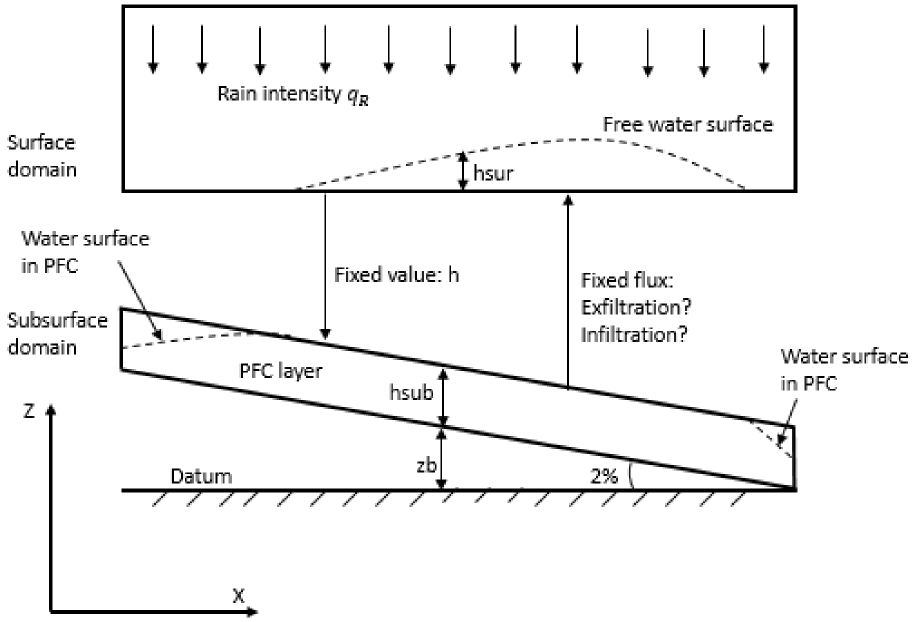

Figure 44. The coupling between the surface and subsurface domain

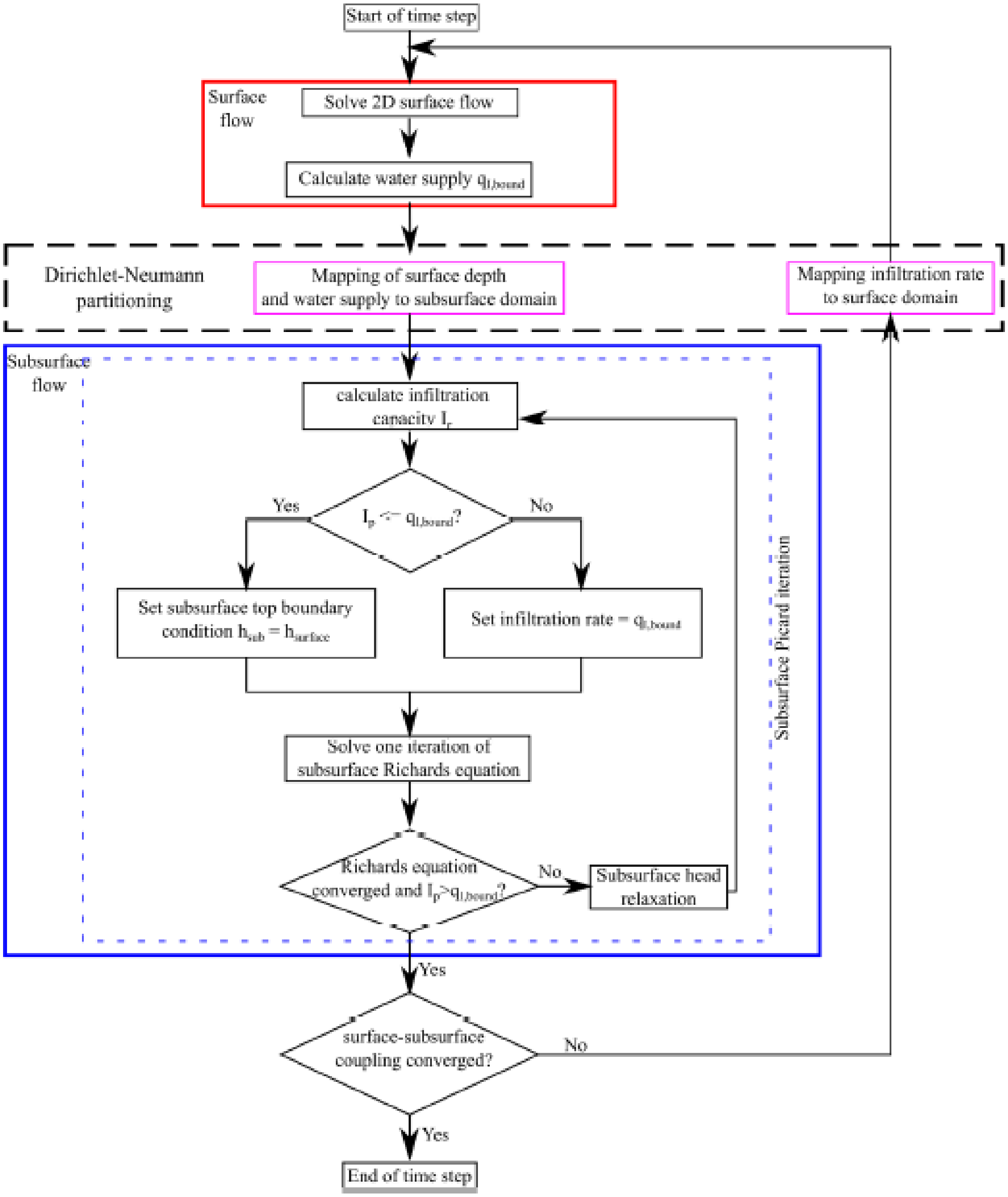

Figure 45. Flow Chart for the coupling algorithm within each time step (Liu et al. 2016)

MODEL CALIBRATION

In the numerical model, three parameters including saturated hydraulic conductivity Ks, n and α in Van Genuchten soil-water model are need to be calibrated based on the experiment data. Since all of the parameters are properties of the PFC, this section will elaborate how these parameters are calibrated using the obtained data from the large-scale physical testing.

Saturated Hydraulic Conductivity Ks

The hydraulic conductivity is determined in the laboratory by the constant head flow test. Due to the large void ratio in the PFCs, A large-scale test was set up to quantify the permeability of the PFC with different void ratios. The U-shape apparatus was composed by 4-inch inner dia. PVC pipes with 42 inches head difference (Figure 46a). The pipes were supported by two wood frames and located between the vertical wood plates, which were fixed by rubber clippers (Figure 46b). Six PFCs specimen with different porosity were fabricated based on the mixture receipt recommend by Sampson (2013), and the quantity of the composites used in the specimen were provided in Table 12.

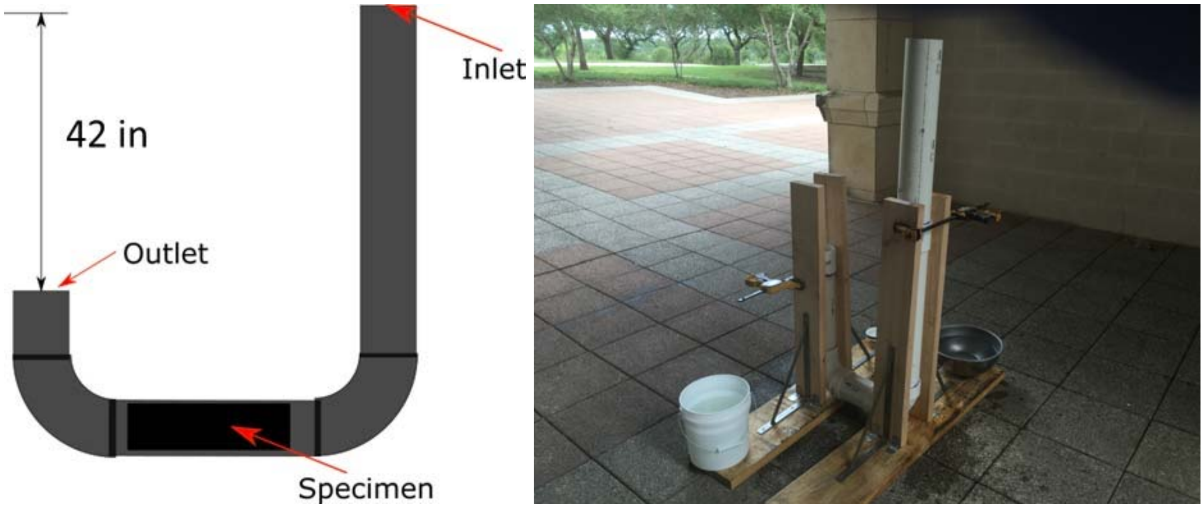

a) **b)**

Figure 46. Permeability test: (a) Schematic cross section of U-shape apparatus, (b) Large scale U-shape apparatus for PFCs permeability test

The samples were first fabricated in the PVC pipe that has a diameter of 4 inches and a length of 8 inches (Figure 47), and then the PVC pipe that contains the specimen was connect to apparatus.

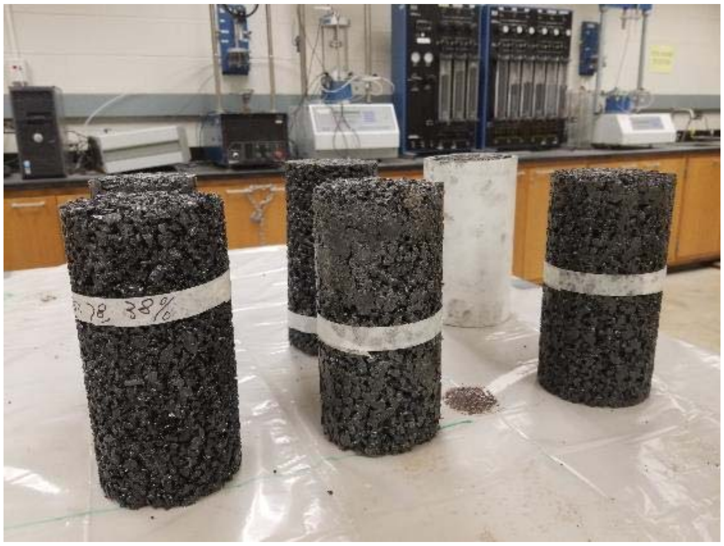

Figure 47. Specimen used in the hydraulic conductivity test

The test results are listed in Table 11. And Figure 48 illustrates that the hydraulic conductivity increases exponentially with the increase of the porosity.

Table 11. Quantity of the Composites used in PFCs Fabrication

No.	Materials			Porosity	Hydraulic conductivity Ks (in/s)
	Rubber Chips (lb)	Rock (lb)	Polymer (in^3)		
#1	1.3	1.3	7.3	0.09	0.04
#2	1.3	1.3	6.4	0.16	0.04
#3	1.5	1.5	8.3	0.26	0.12
#4	1.4	1.4	8.3	0.27	0.21
#5	1.3	1.3	4.9	0.33	0.47
#6	1.4	1.4	4.8	0.38	0.55

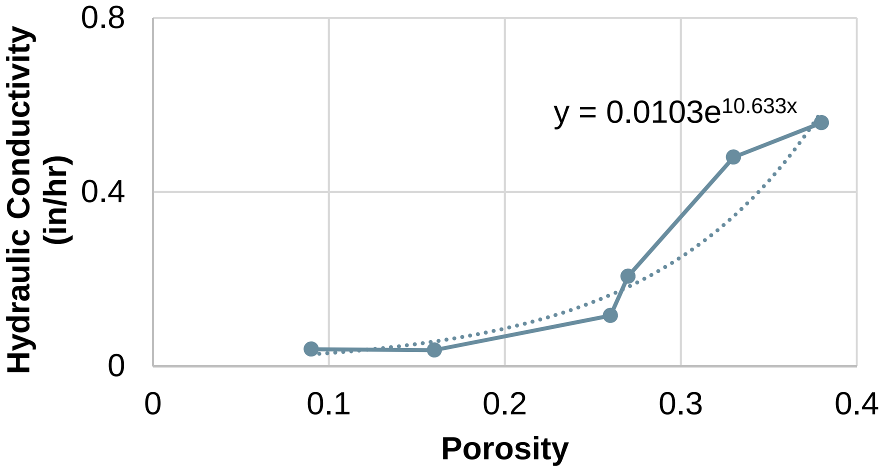

Figure 48. Porosity vs. hydraulic conductivity

Van Genuchten Parameters n and α

Since the Soil-Water Characteristic Curve (SWCC) for PFCs is not available, the Van Genuchten parameters are need to be calibrated based on the laboratory experiment data from Texas Tech University (TTU), and the sampled data is listed in Table 12. The values for the known parameters are presented in Table 13.

Table 12. Sampled Data Used for Calibration

Manometer Location (ft)	**Water Head (in)**	
	Open Drainage Rain Intensity (in/hr) = 5.4	**Closed Drainage Rain Intensity (in/hr) = 0.87**
2	1.4148	1.5327
6	1.7685	1.4148
10	2.0043	1.2576
14	2.7903	1.6506
18	2.2794	1.6899
22	2.5938	1.4934
26	3.144	1.8471
30	1.4148	2.7117
34	2.2008	1.3755
38	2.4366	1.6899
42	2.5938	2.0436
46	2.6331	2.751

Table 13. Parameters Used in Numerical Model

Parameter	Unit	Value
PFC length	ft	48
PFC width	ft	5.5
Slope	%	2.0
Manning's η	s/ft$^{1/3}$	0.015
Saturated moisture content θ	%	38.0
Residual moisture content θr	%	1.0

The calibration of α was carried out with the values of 0.3, 3, 15 and 30, under the condition of $n = 2$, rain intensity $r = 5.4$ in/hr, and opened underdrain. The calibration of the Van Genuchten parameter α suggested that the value of 3 makes more favorable overall match, as shown in Figure 49.

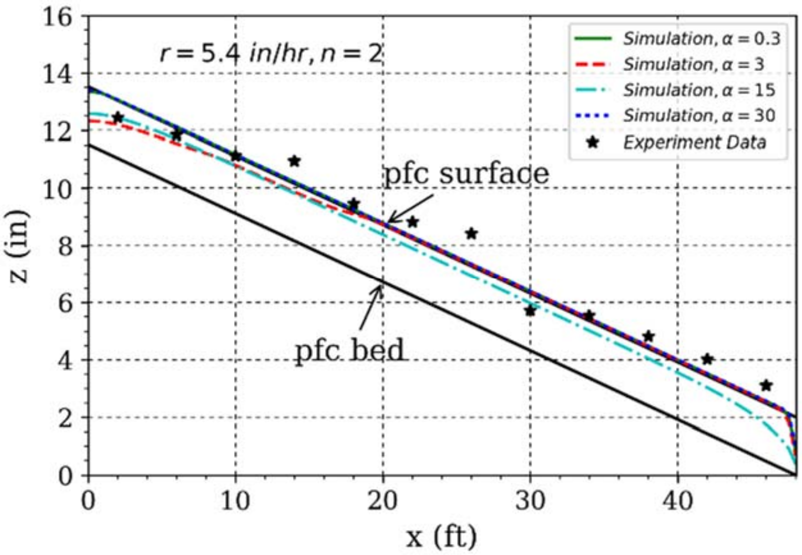

Figure 49. Water depth at steady state with different α value

With the same rain intensity and underdrain condition, the calibration of n was carried out with the values of 2 and 3, while higher values of n do not make physical sense to the PFC material. The calibration suggested that the result most close to the measured data when Van Genuchten parameter $n = 2$, as shown in Figure 50.

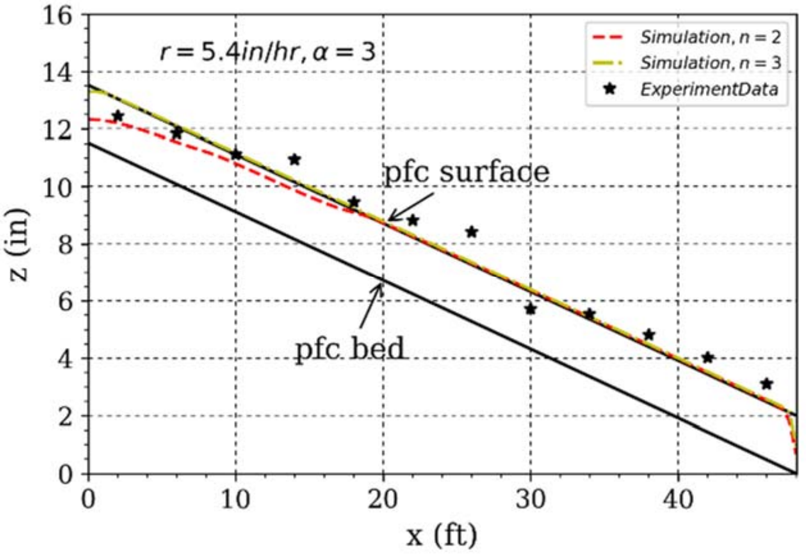

Figure 50. Water depth at steady state with different n value

The values of n and α were then validated with the measured data in the condition of rain intensity r = 0.87 in/hr and closed underdrain. As shown in Figure 51, the simulated result generally have the same trend as the experiment data with acceptable deviation from the test.

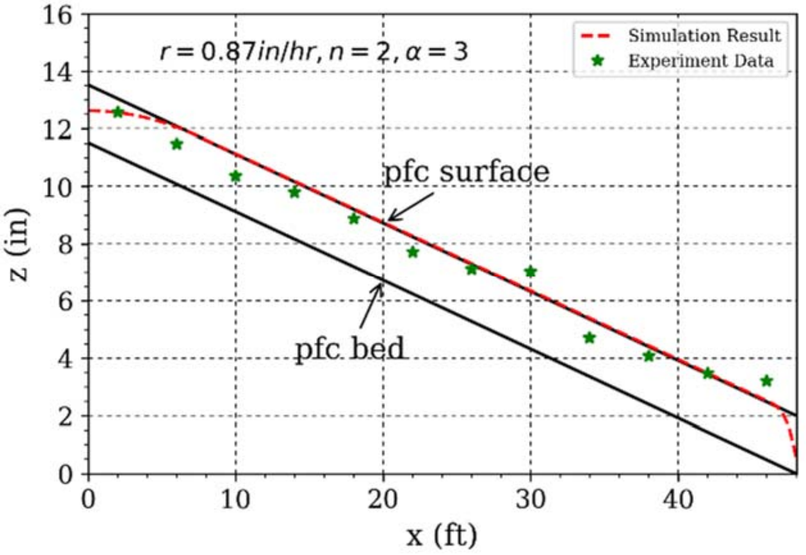

Figure 51. Water depth at steady state with rain intensity r = 0.87 in/hr and closed underdrain

RESULTS OF NUMERICAL SIMULATIONS

On the basis of the calibrated numerical model, a parametric study was conducted to assess the effectiveness of the undrain under different conditions. The roadway was simulated under three different widths (W), i.e., as 24 feet (2 lanes), 36 feet (3 lanes) and 48 feet (4 lanes) with the same longitudinal length (L) as 60 feet. Different combinations between cross (0%, 1%, 2% and 3%) and longitudinal (0% and 1%) slopes were considered. The scheme for the roadway geometry with underdrain is shown as Figure 52. The underdrain is 4 inches width for PFC drainage and was located at the mid-span of the longitudinal direction. It was slot cut into the base of the pavement that would be filled with pipes or coarse grain materials. The geometric parameters are summarized in Table 14. In the numerical simulation, four different rainfall intensities were assessed, namely, 0.4 in/hr (moderate), 1.0 in/hr (heavy), 3.0 in/hr (intense), and 5.0 in/hr (extreme). The parameters used in the simulation are listed in Table 15.

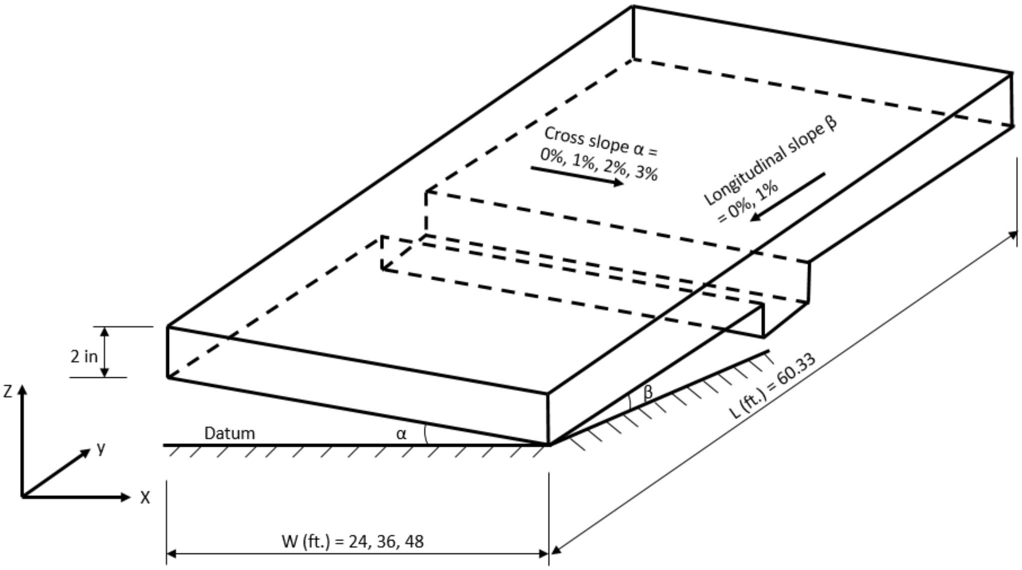

Figure 52. Scheme for the roadway geometry

Table 14. Values of parameters for roadway geometry

Parameter	Unit	Value
PFC length (L)	ft	60
PFC width (W)	ft	24, 36, 48
PFC thickness	in	2.0
Undrain width	in	4.0
Cross slope (s)	%	0, 1.0, 2.0, 3.0
Longitudinal slopes (s)	%	0, 1.0

Table 15. Modeling parameters used in cases

Parameter	Unit	Value
Rain intensity (r)	in/hr	0.4, 1.0, 3.0, 5.0
Hydraulic conductivity	ft/hr	165.4
n (Van Genuchten parameter)	-	2
α (Van Genuchten parameter)	-	3

The simulation started with dry pavement and lasted until the equilibrium was reached under a certain rain intensity. Depending the rain intensity and slope, it took up to hour(s) until the water surface became steady.

Water Flow within and on PFC without Underdrain

Figures 53~76 present the water depth under conditions of different rainfall intensities and roadway geometries when the underdrain is closed. These figures indicate that larger slope would facilitate the water drainage only when the rain intensity is less than 0.4 in/hr and the pavement is no more than 2-lane width. In other words, for most of the cases investigate in this study, underdrain appears to be necessary to remove standing water on the pavement surface.

1) Zero slope on both longitudinal and cross directions

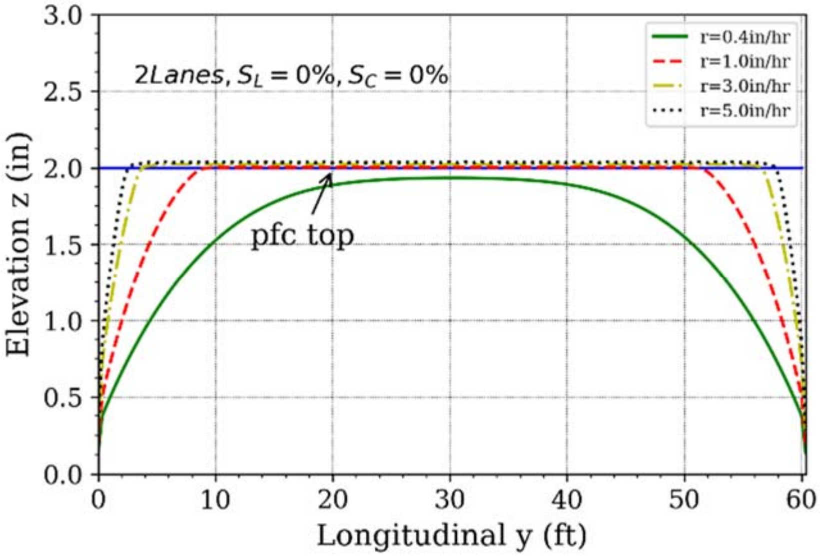

Figure 53. Water depth in 2-lane PFC pavement with zero slope on both direction

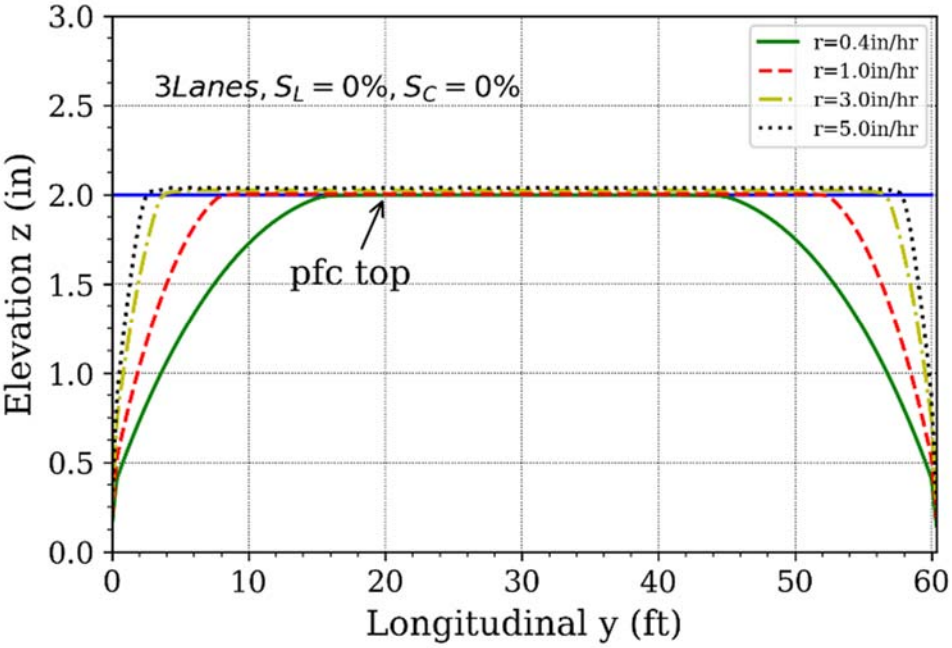

Figure 54. Water depth in 3-lane PFC pavement with zero slope on both direction

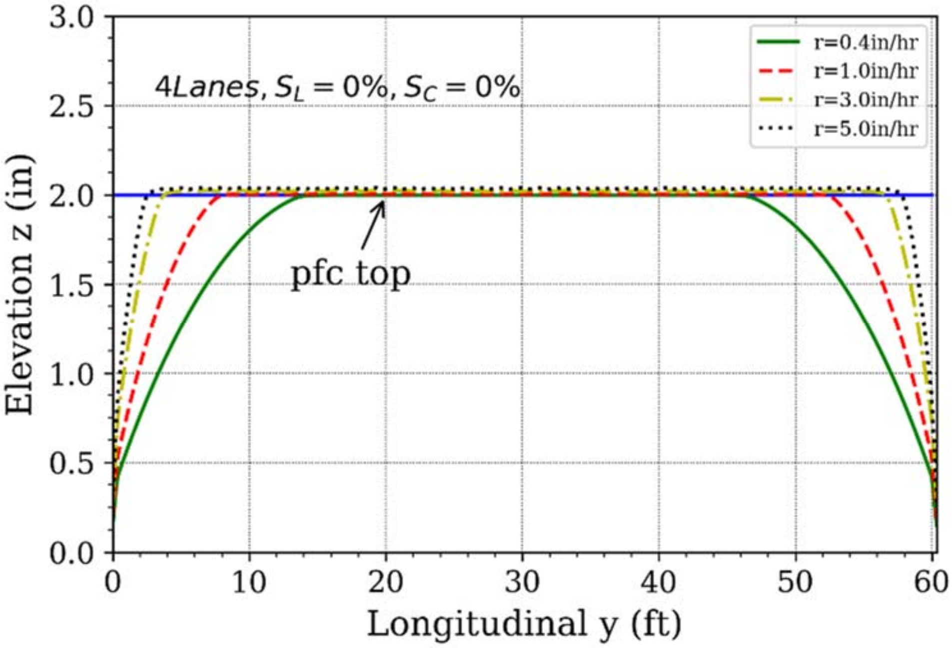

Figure 55. Water depth in 4-lane PFC pavement with zero slope on both direction

2) Longitudinal slope = 0% and cross slope = 1%

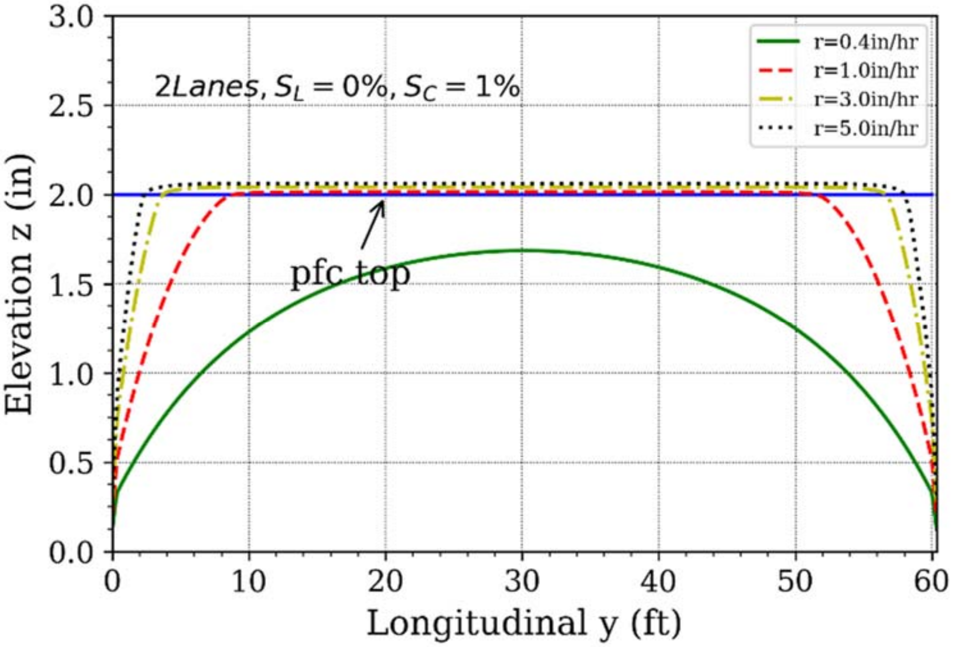

Figure 56. Water depth in 2-lane PFC pavement with 0% longitudinal and 1% cross slope

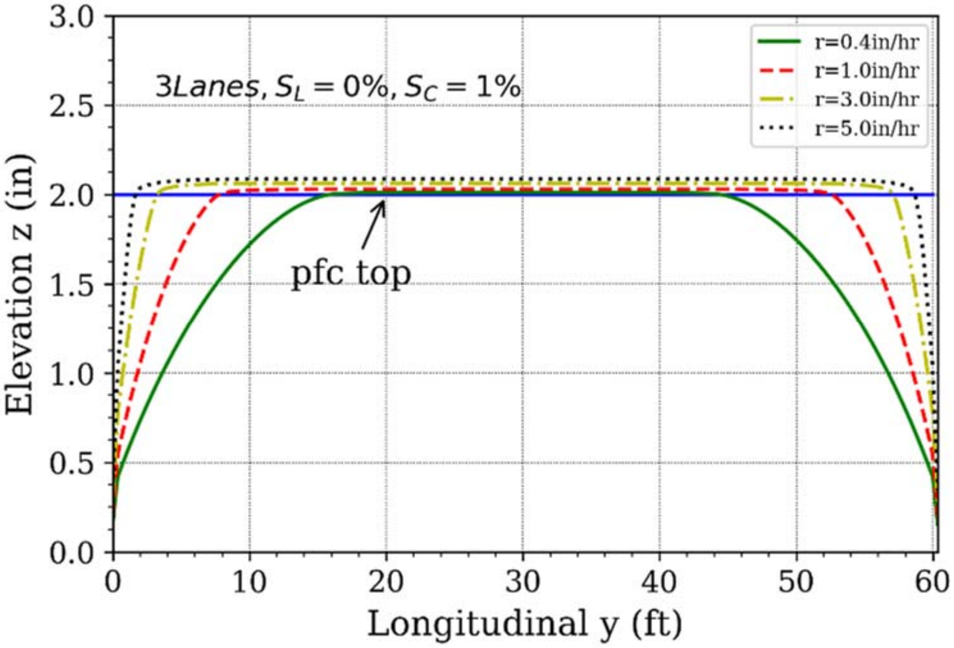

Figure 57. Water depth in 3-lane PFC pavement with 0% longitudinal and 1% cross slope

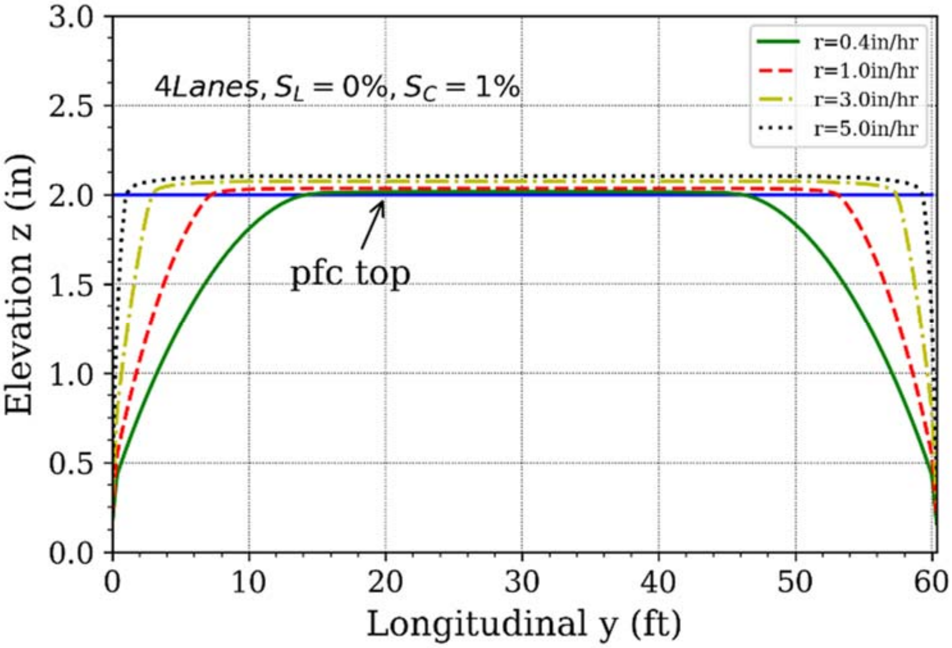

Figure 58. Water depth in 4-lane PFC pavement with 0% longitudinal and 1% cross slope

3) Longitudinal slope = 0% and Cross slope = 2%

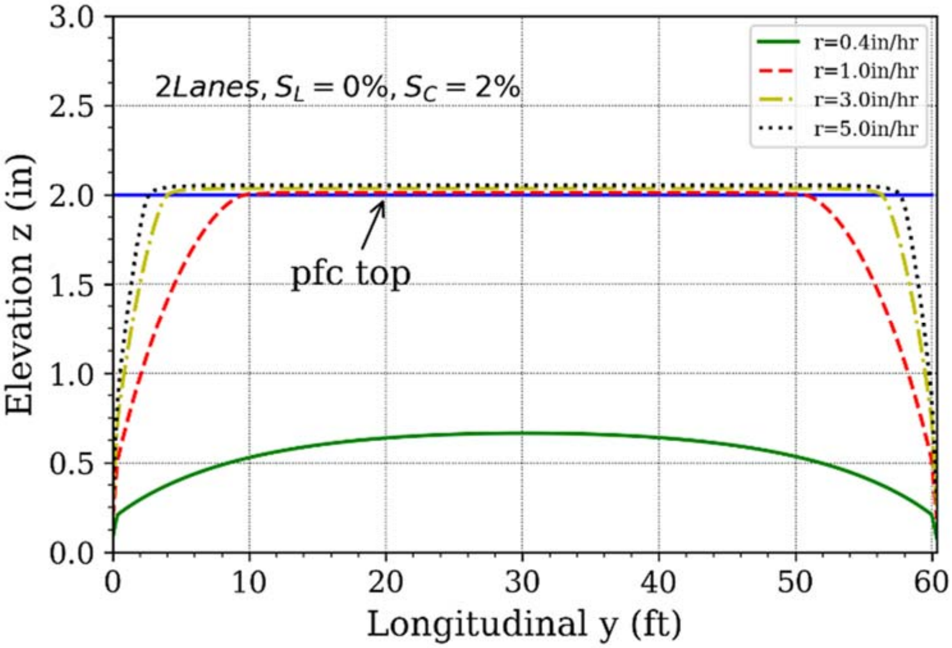

Figure 59. Water depth in 2-lane PFC pavement with 0% longitudinal and 2% cross slope

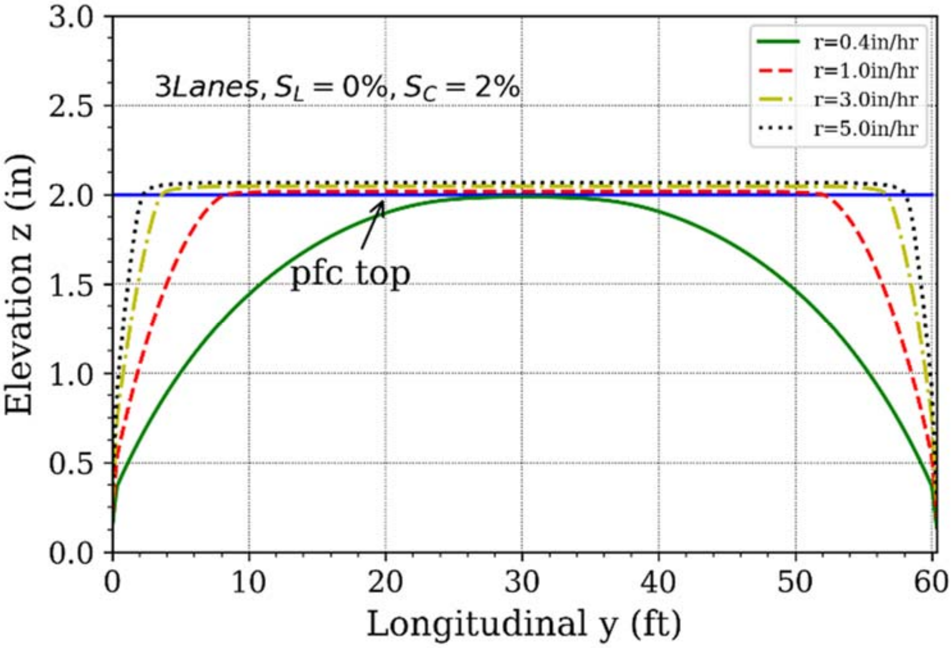

Figure 60. Water depth in 3-lane PFC pavement with 0% longitudinal and 2% cross slope

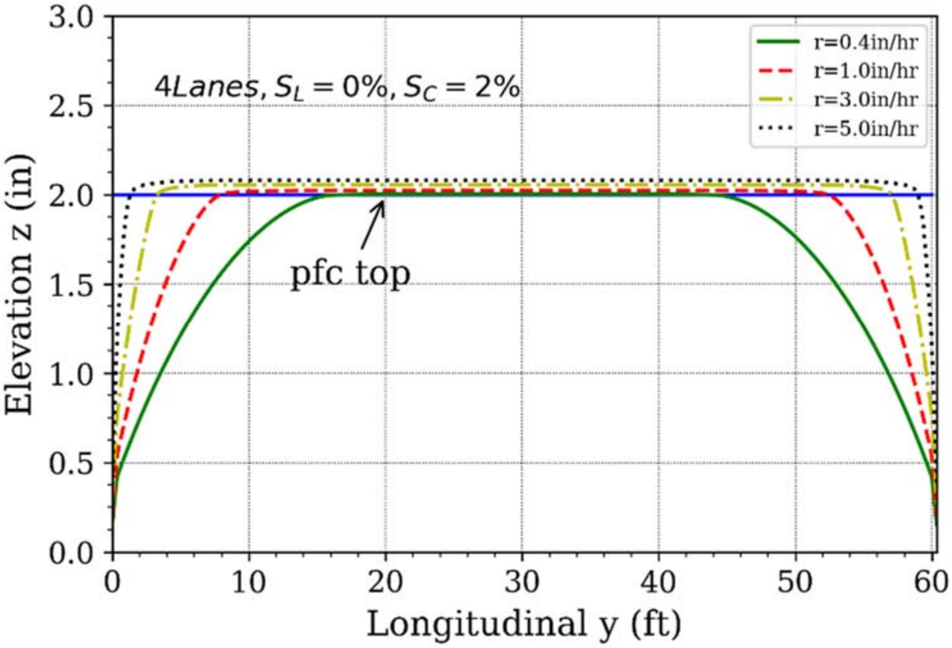

Figure 61. Water depth in 4-lane PFC pavement with 0% longitudinal and 2% cross slope

4) Longitudinal slope = 0% and Cross slope = 3%

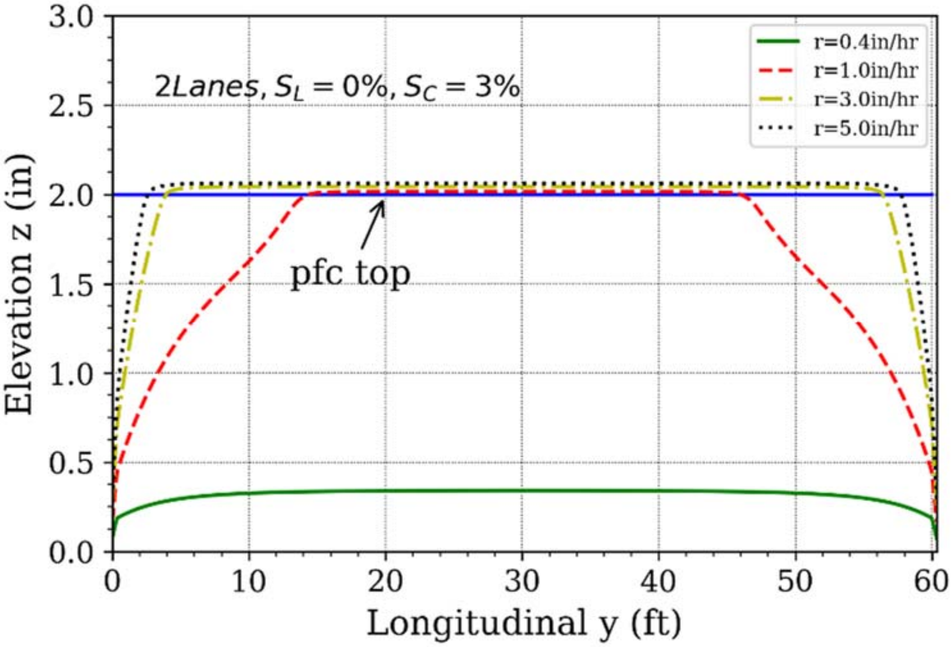

Figure 62. Water depth in 2-lane PFC pavement with 0% longitudinal and 3% cross slope

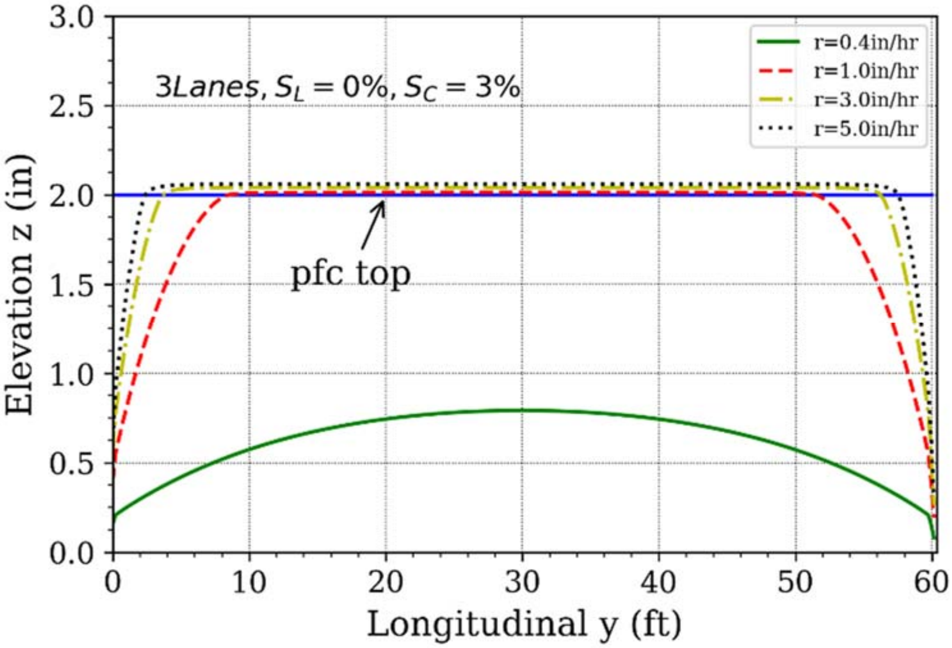

Figure 63. Water depth in 3-lane PFC pavement with 0% longitudinal and 3% cross slope

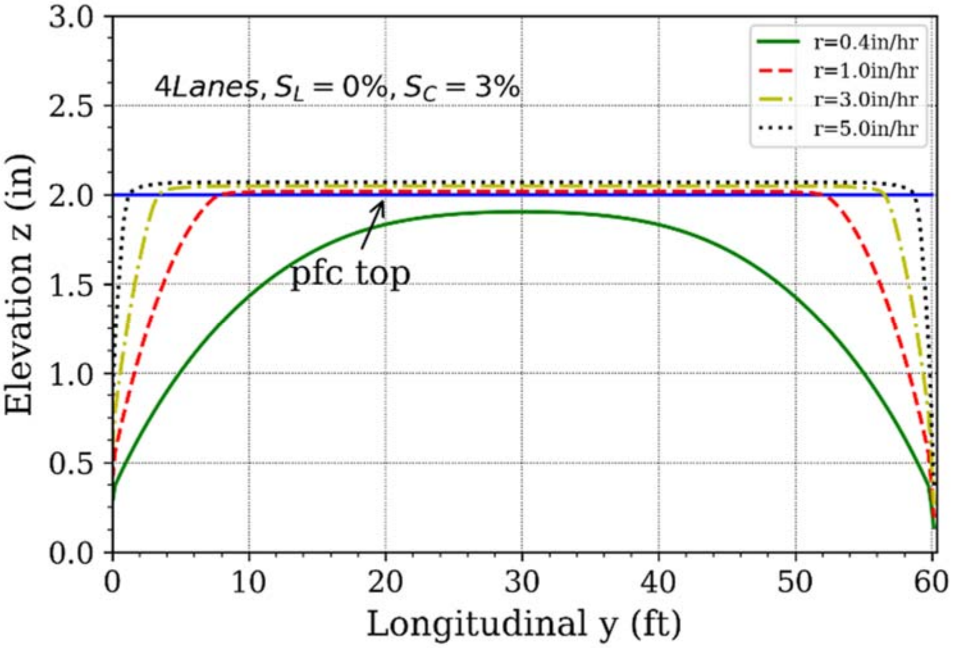

Figure 64. Water depth in 3-lane PFC pavement with 0% longitudinal and 3% cross slope

5) Longitudinal slope = 1% and Cross slope = 0%

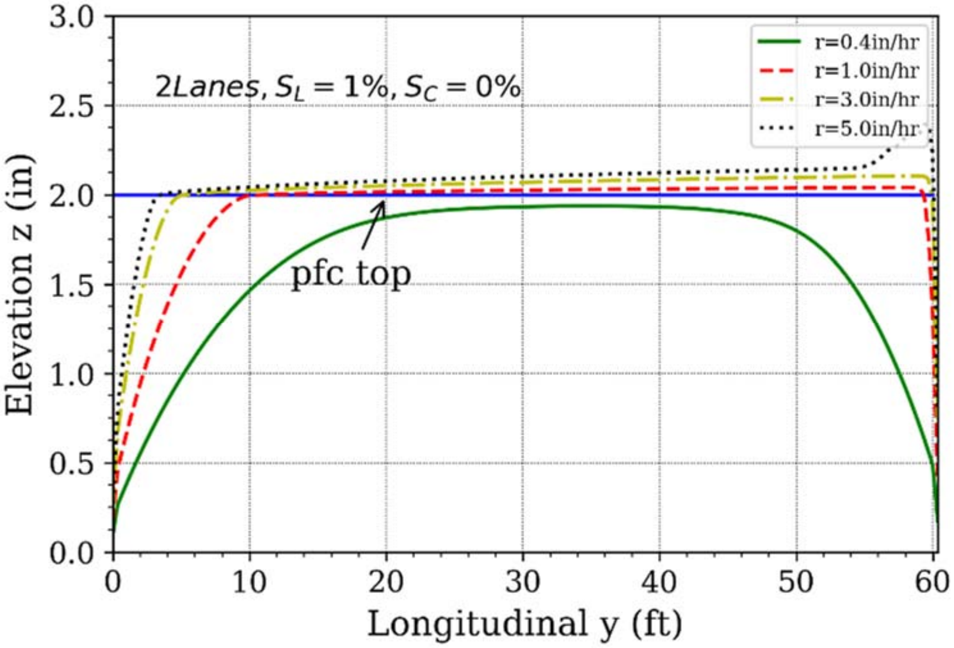

Figure 65. Water depth in 2-lane PFC pavement with 1% longitudinal and 0% cross slope

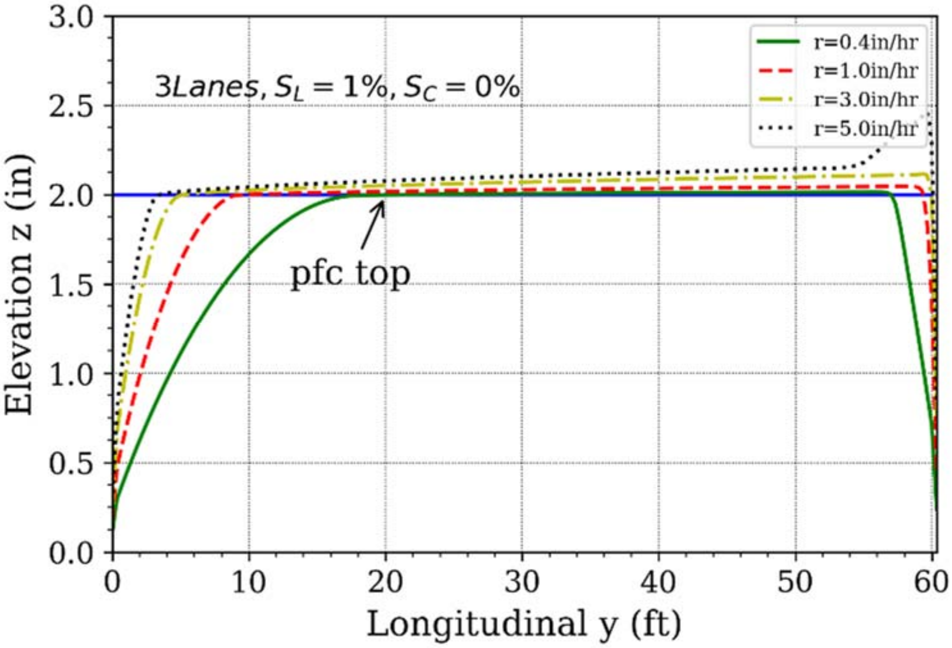

Figure 66. Water depth in 3-lane PFC pavement with 1% longitudinal and 0% cross slope

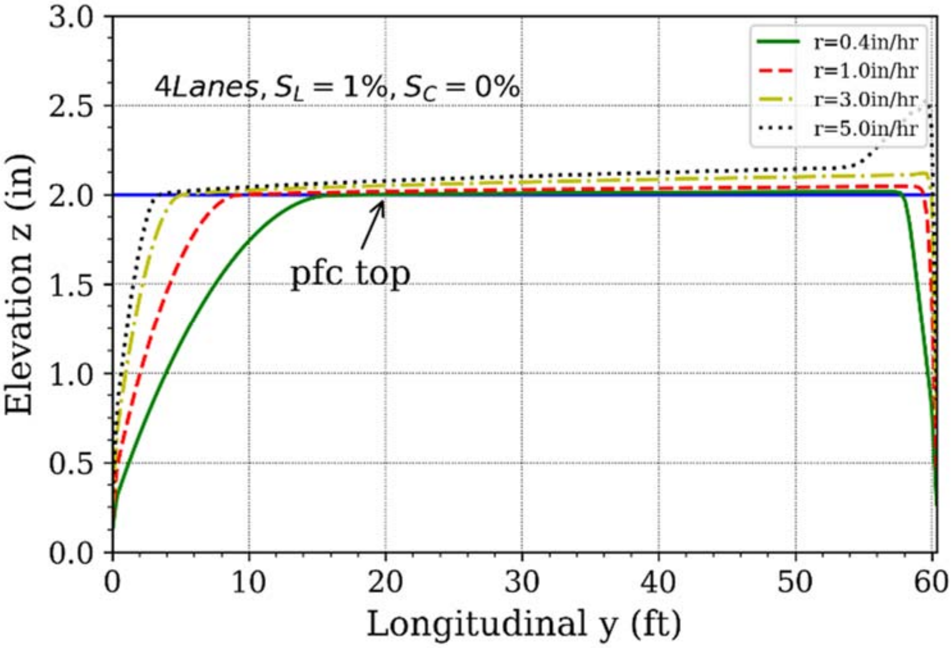

Figure 67. Water depth in 4-lane PFC pavement with 1% longitudinal and 0% cross slope

6) Longitudinal slope = 1% and Cross slope = 1%

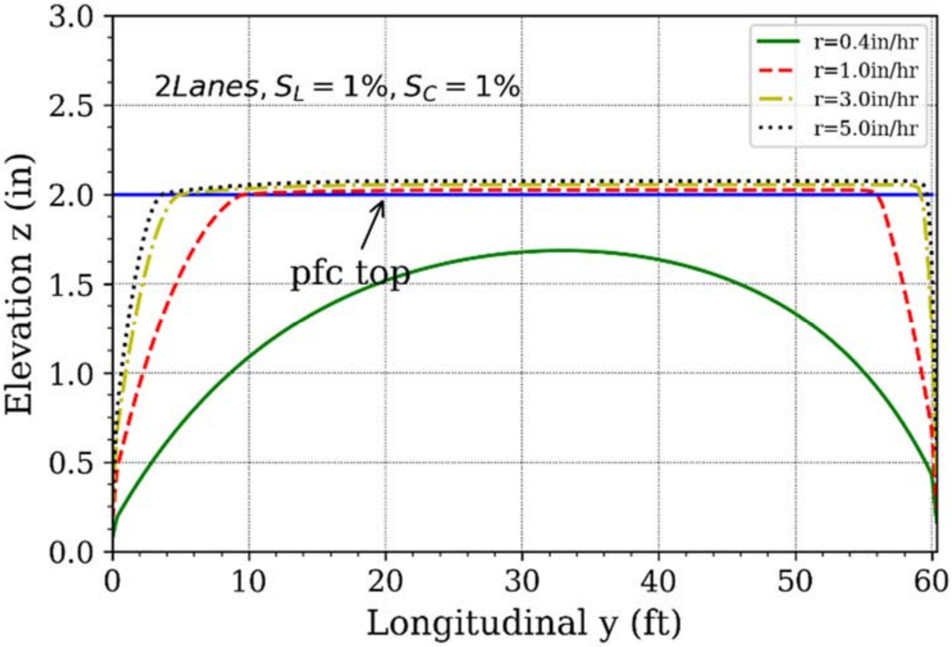

Figure 68. Water depth in 2-lane PFC pavement with 1% longitudinal and 1% cross slope

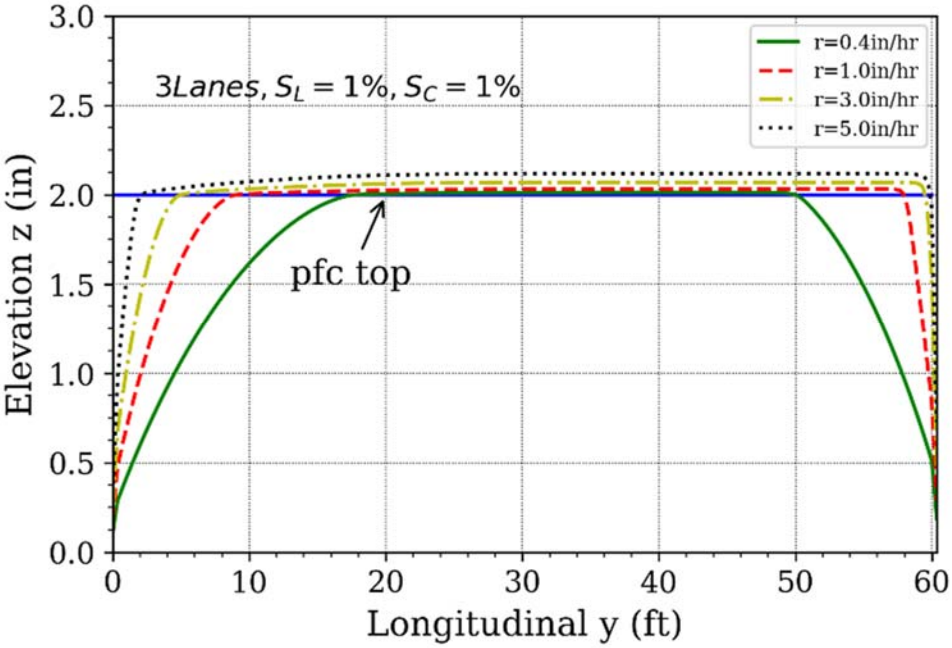

Figure 69. Water depth in 3-lane PFC pavement with 1% longitudinal and 1% cross slope

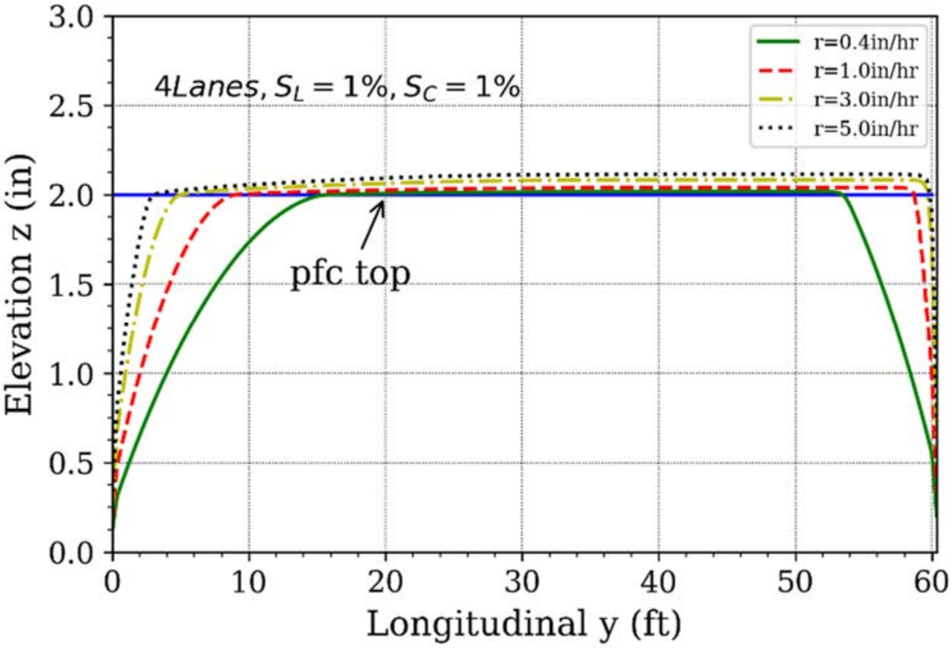

Figure 70. Water depth in 4-lane PFC pavement with 1% longitudinal and 1% cross slope

7) Longitudinal slope = 1% and Cross slope = 2%

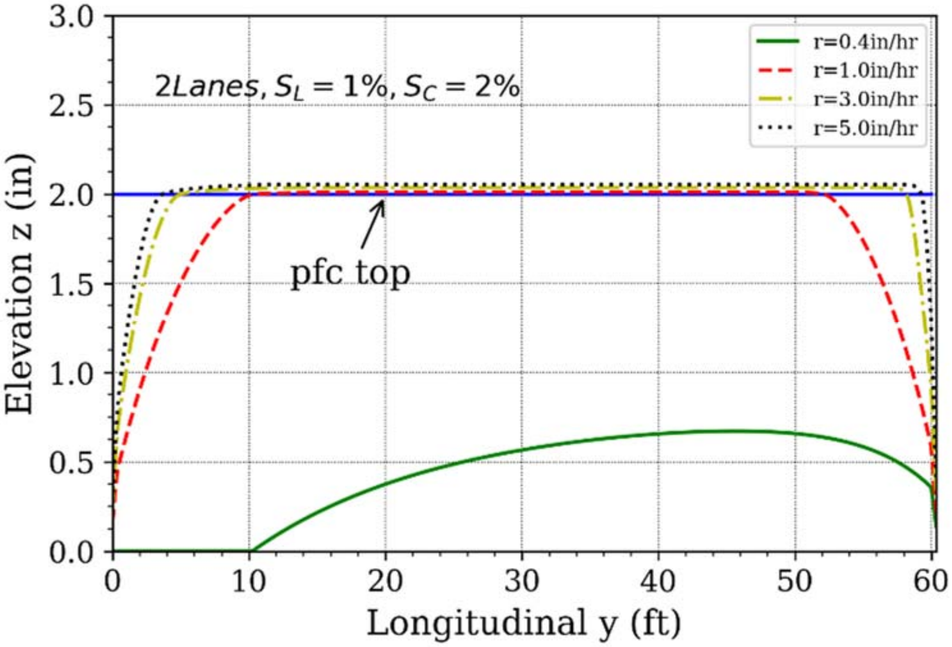

Figure 71. Water depth in 2-lane PFC pavement with 1% longitudinal and 2% cross slope

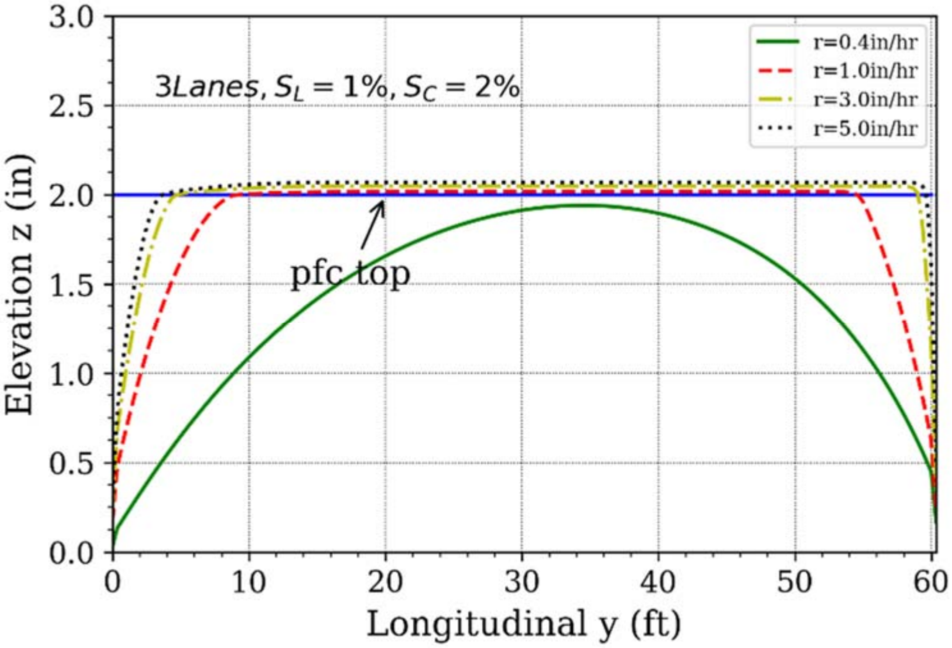

Figure 72. Water depth in 3-lane PFC pavement with 1% longitudinal and 2% cross slope

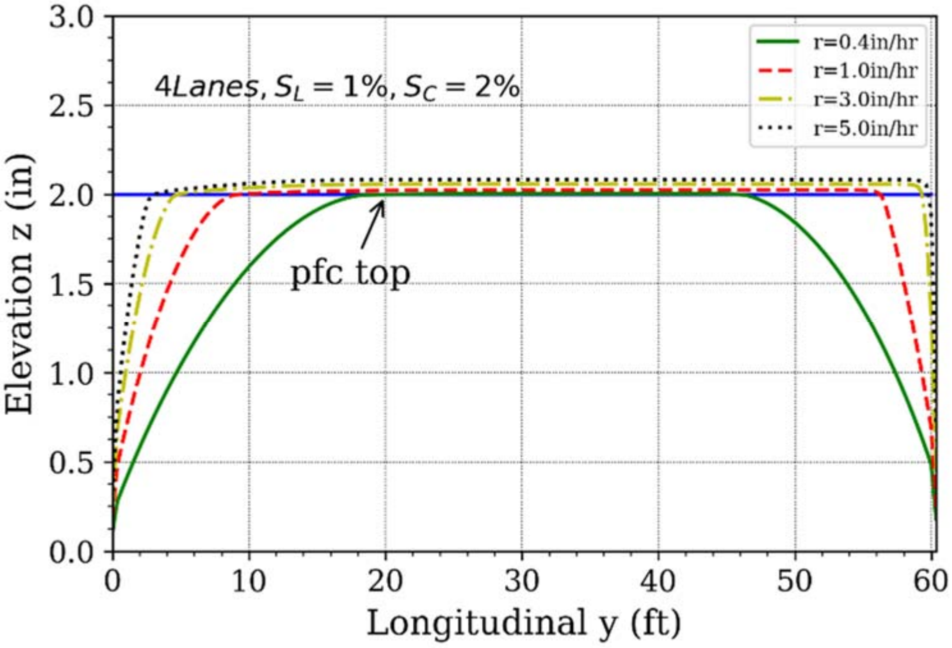

Figure 73. Water depth in 4-lane PFC pavement with 1% longitudinal and 2% cross slope

6) Longitudinal slope = 1% and Cross slope = 3%

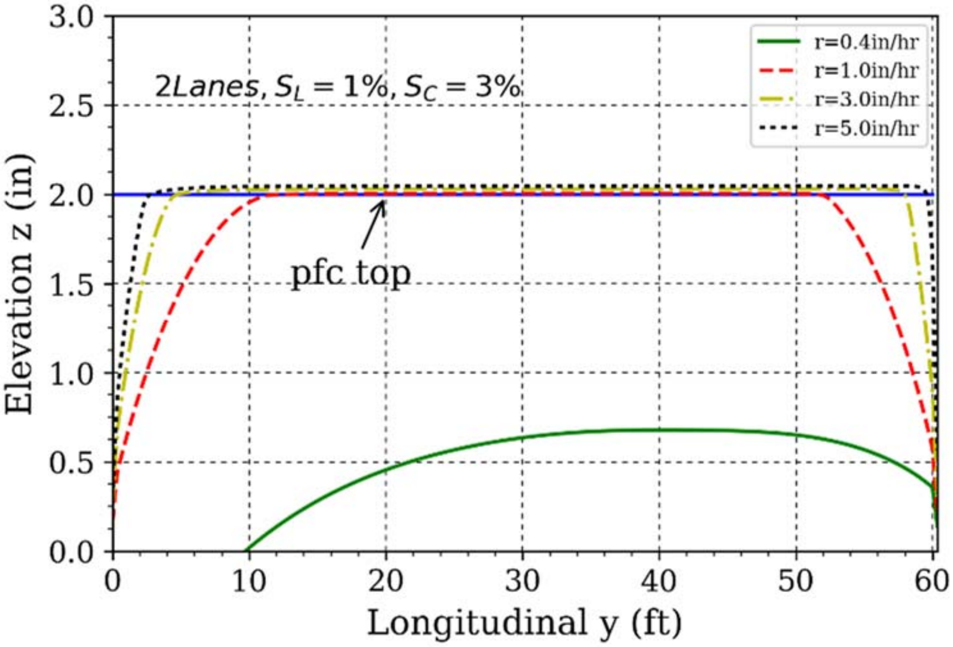

Figure 74. Water depth in 2-lane PFC pavement with 1% longitudinal and 3% cross slope

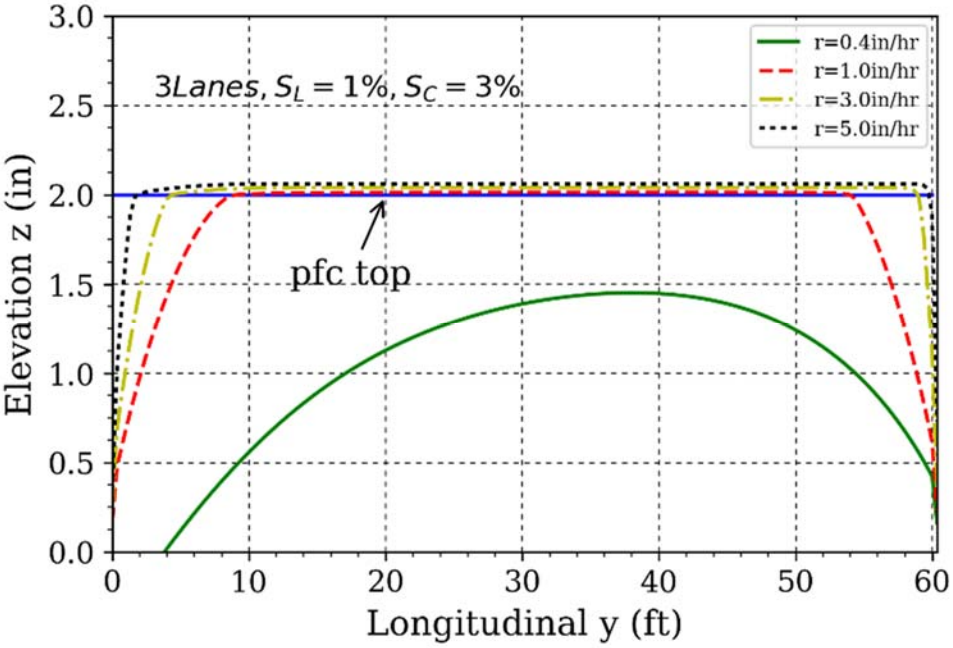

Figure 75. Water depth in 3-lane PFC pavement with 1% longitudinal and 3% cross slope

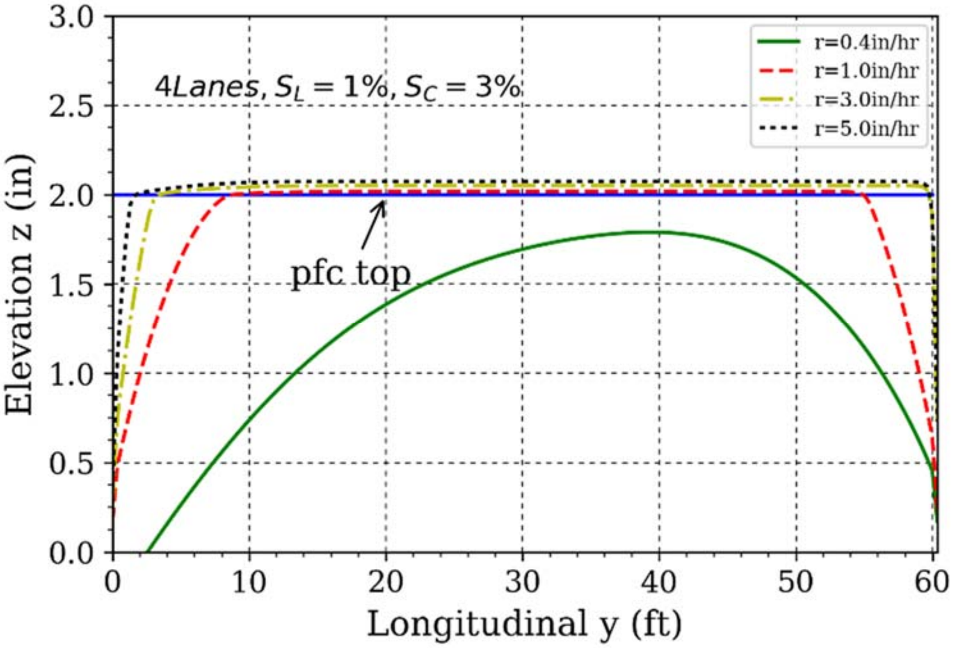

Figure 76. Water depth in 4-lane PFC pavement with 1% longitudinal and 3% cross slope

Water Flow within and on PFC with Underdrain

Given certain geometry slopes, Figures 77~100 show the underdrain's effective drainage range under various rain intensity. As the trend shown in the figures, the effectiveness of the underdrain decreases with the increase of the rainfall intensity when the slopes are given. For example, the underdrain can keep the 2-lane pavement, which has zero slope on both directions, from standing water within 20 ft when the rain intensity is 1 in/hr, and this number will gradually decrease to 3 ft as the rain intensity increases to 5 in/hr.

On the other hand, raising the slopes on both directions does not necessarily mean linear increase of the underdrain's effective range. For example, in the case of 4-lane pavement with 3.0 in/hr rain intensity and 1% longitudinal slope, the effective drainage range oscillates between 6.66 ft and 4.13 ft as the cross slope changes from 0% to 3%. This may due to the fact that water is cumulated at the lower corner of the pavement, where the elevation of the drainage is too high to convey the pond.

1) Zero slope on both longitudinal and cross direction

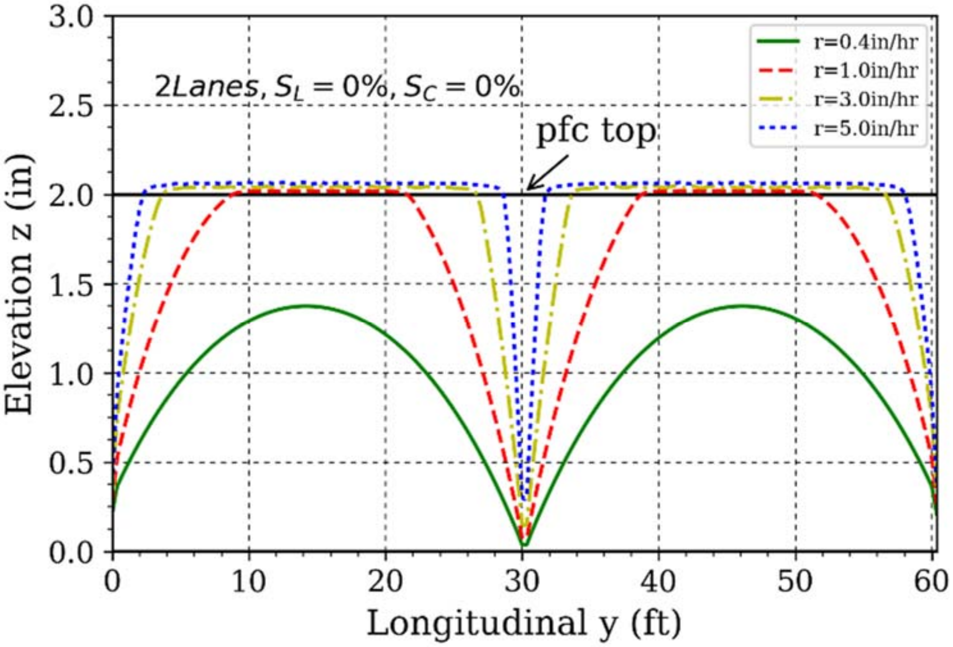

Figure 77. Influence range of underdrain on 2-lane PFC pavement with zero slope on both direction

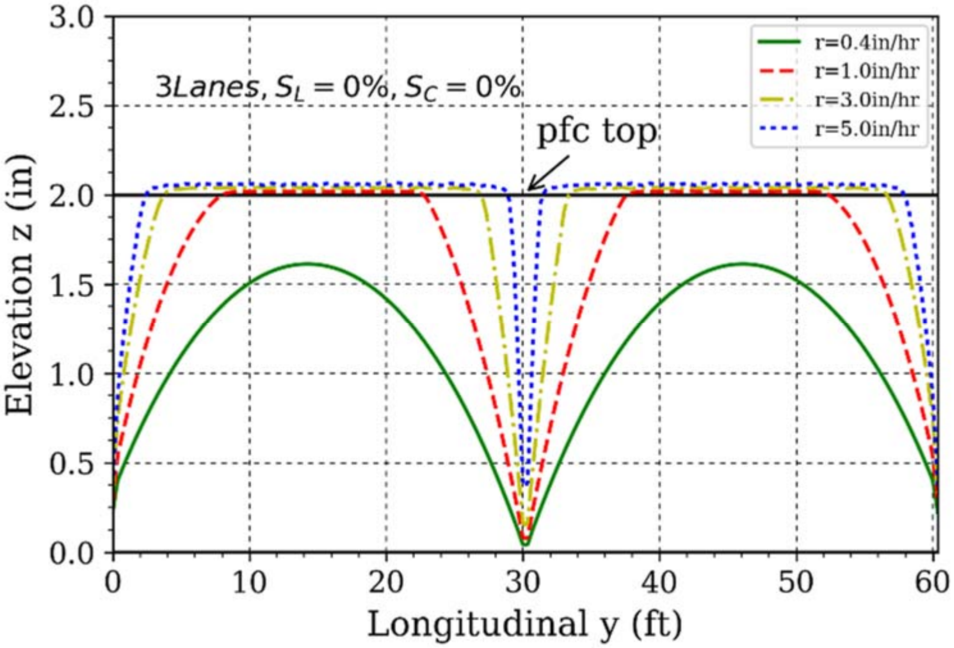

Figure 78. Influence range of underdrain on 3-lane PFC pavement with zero slope on both direction

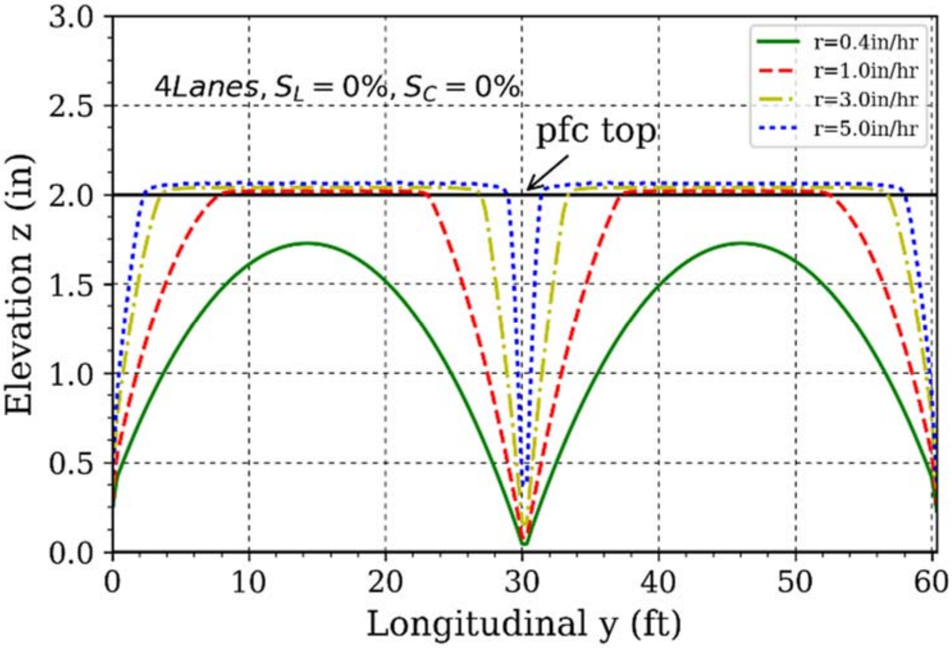

Figure 79. Influence range of underdrain on 4-lane PFC pavement with zero slope on both direction

2) Longitudinal slope = 0% and Cross slope = 1%

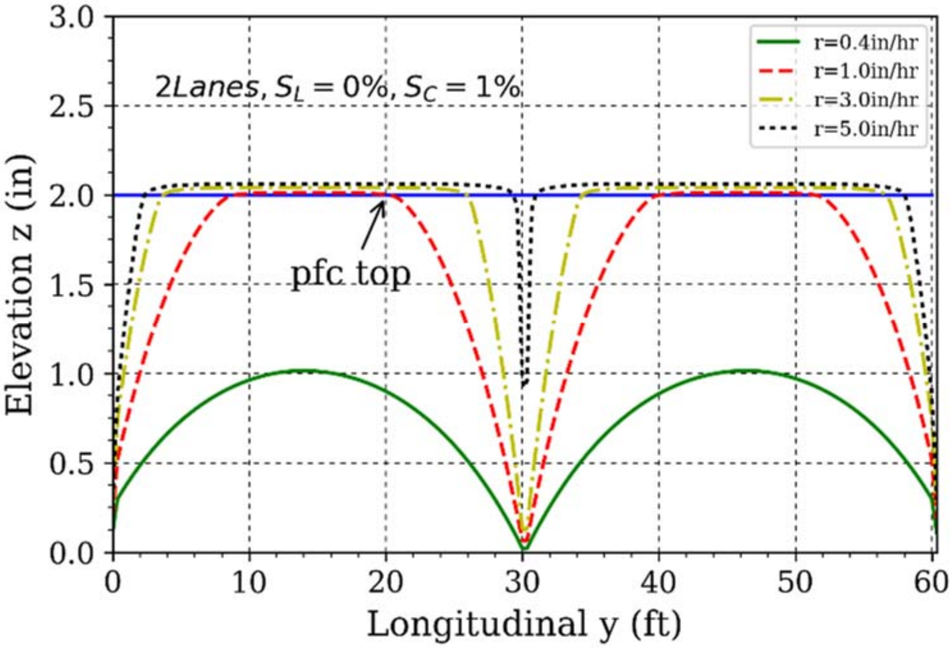

Figure 80. Influence range of underdrain on 2-lane PFC pavement with 0% longitudinal and 1% cross slope

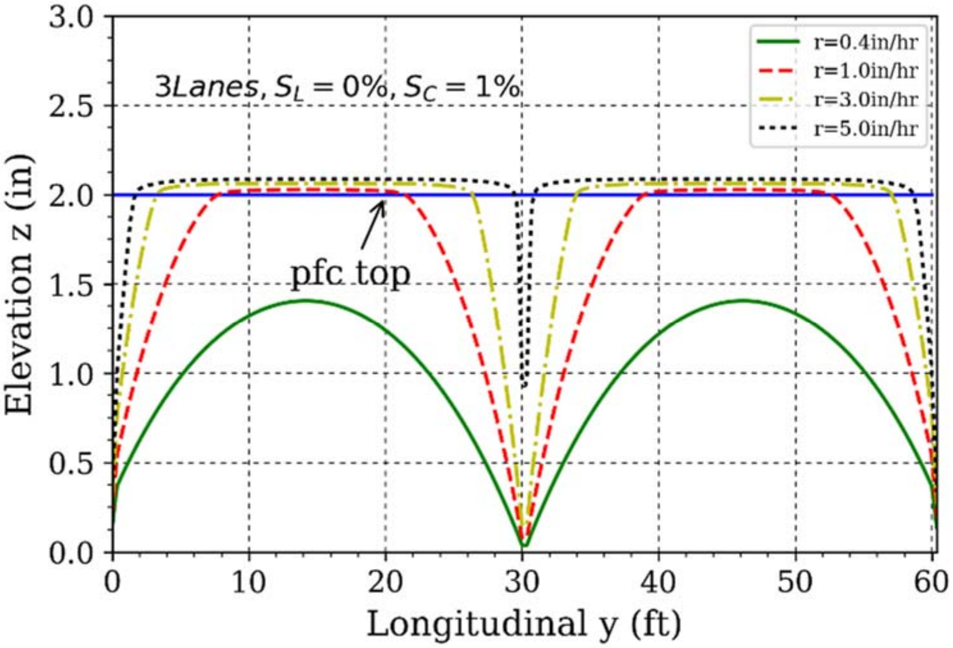

Figure 81. Influence range of underdrain on 3-lane PFC pavement with 0% longitudinal and 1% cross slope

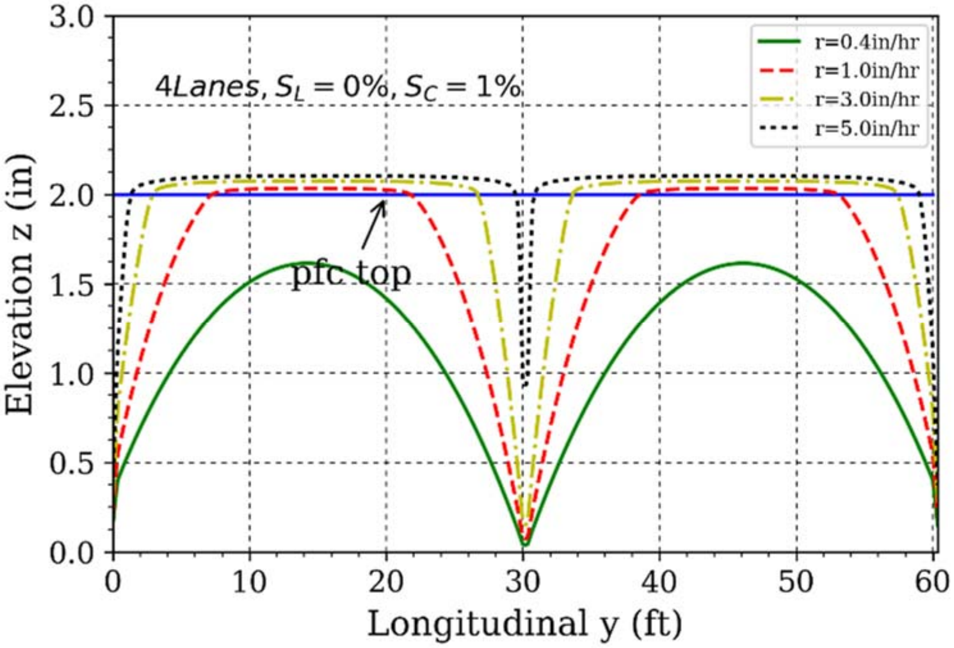

Figure 82. Influence range of underdrain on 4-lane PFC pavement with 0% longitudinal and 1% cross slope

3) Longitudinal slope = 0% and Cross slope = 2%

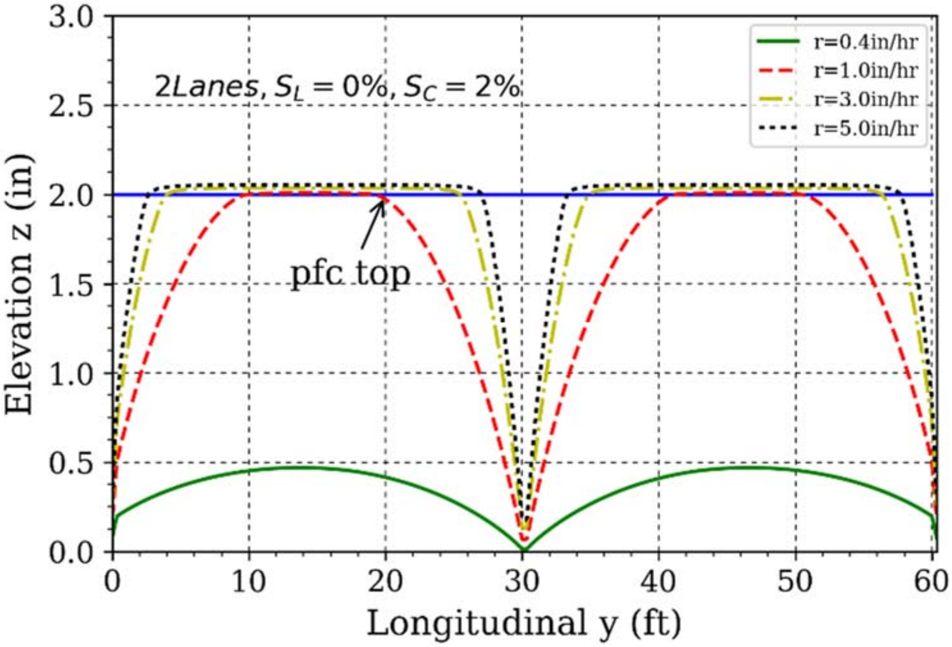

Figure 83. Influence range of underdrain on 2-lane PFC pavement with 0% longitudinal and 2% cross slope

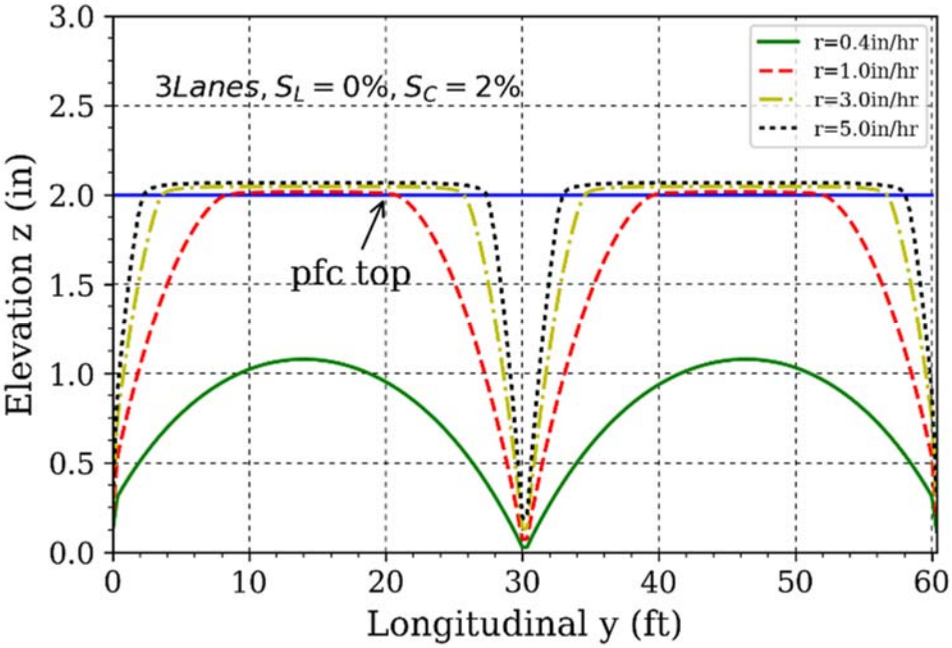

Figure 84. Influence range of underdrain on 3-lane PFC pavement with 0% longitudinal and 2% cross slope

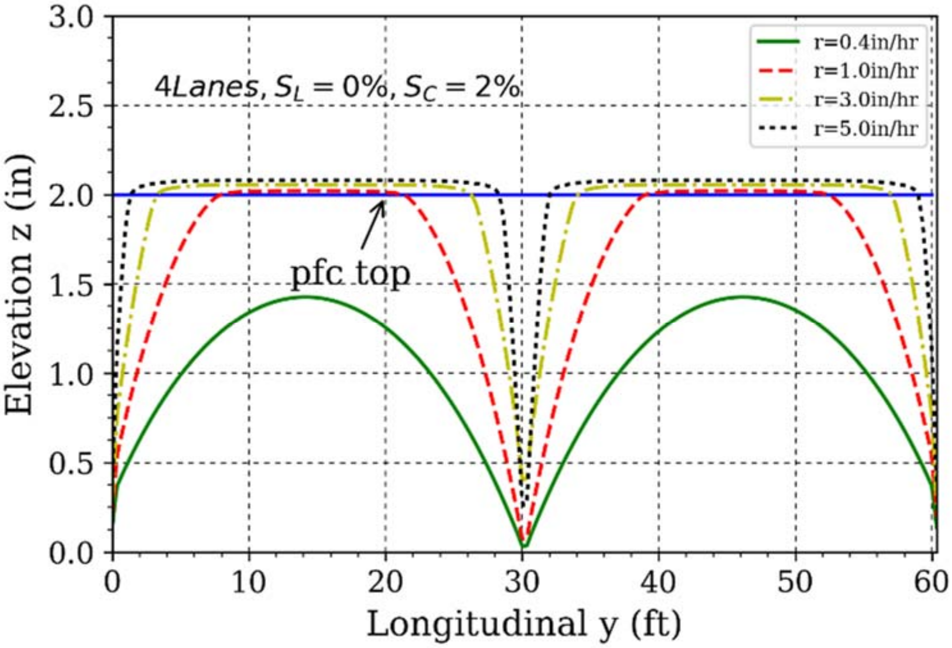

Figure 85. Influence range of underdrain on 4-lane PFC pavement with 0% longitudinal and 2% cross slope

4) Longitudinal slope = 0% and Cross slope = 3%

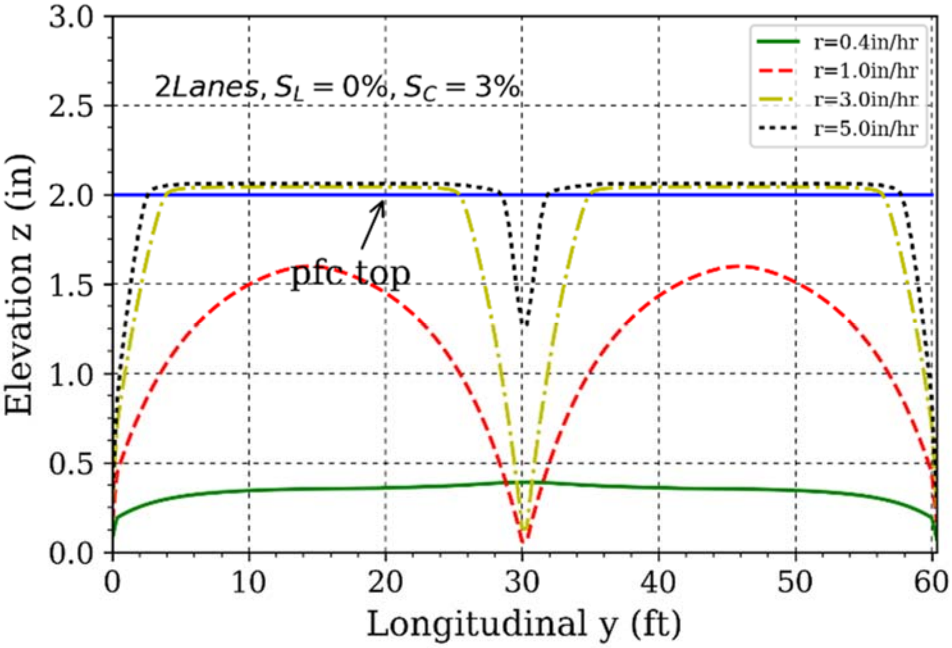

Figure 86. Influence range of underdrain on 2-lane PFC pavement with 0% longitudinal and 3% cross slope

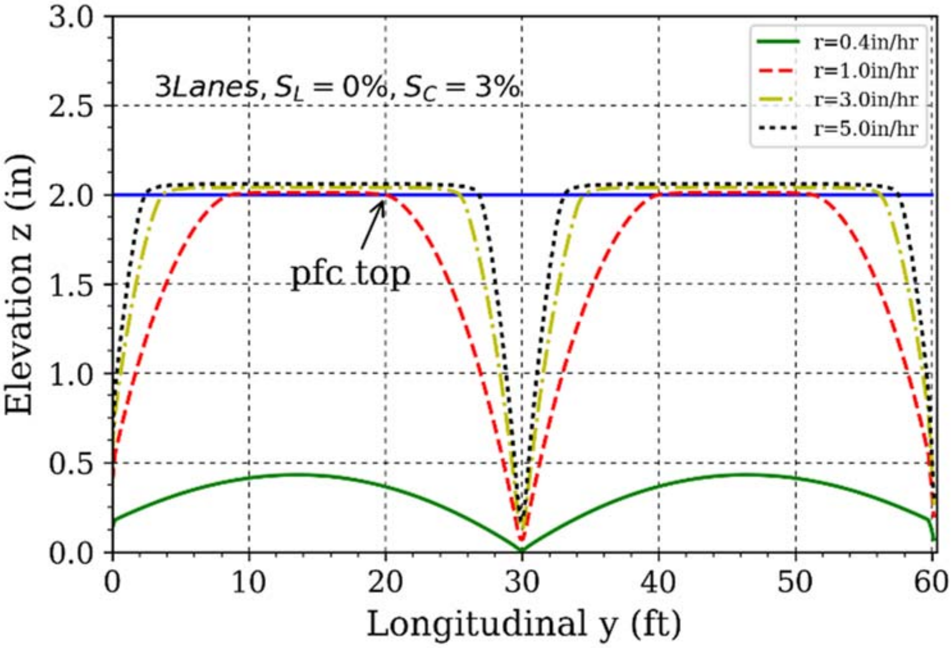

Figure 87. Influence range of underdrain on 3-lane PFC pavement with 0% longitudinal and 3% cross slope

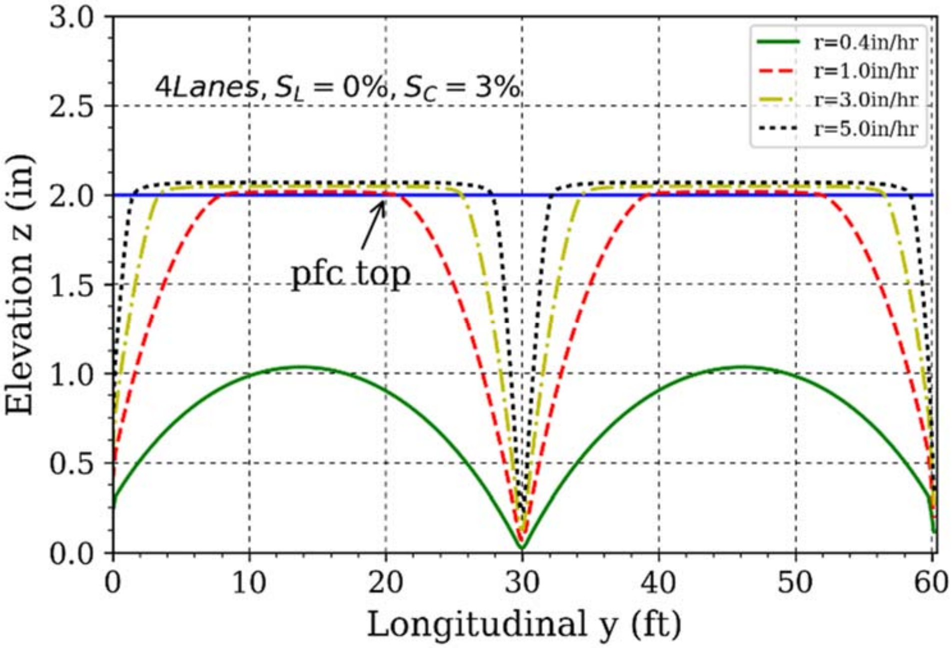

Figure 88. Influence range of underdrain on 4-lane PFC pavement with 0% longitudinal and 3% cross slope

5) Longitudinal slope = 1% and Cross slope = 0%

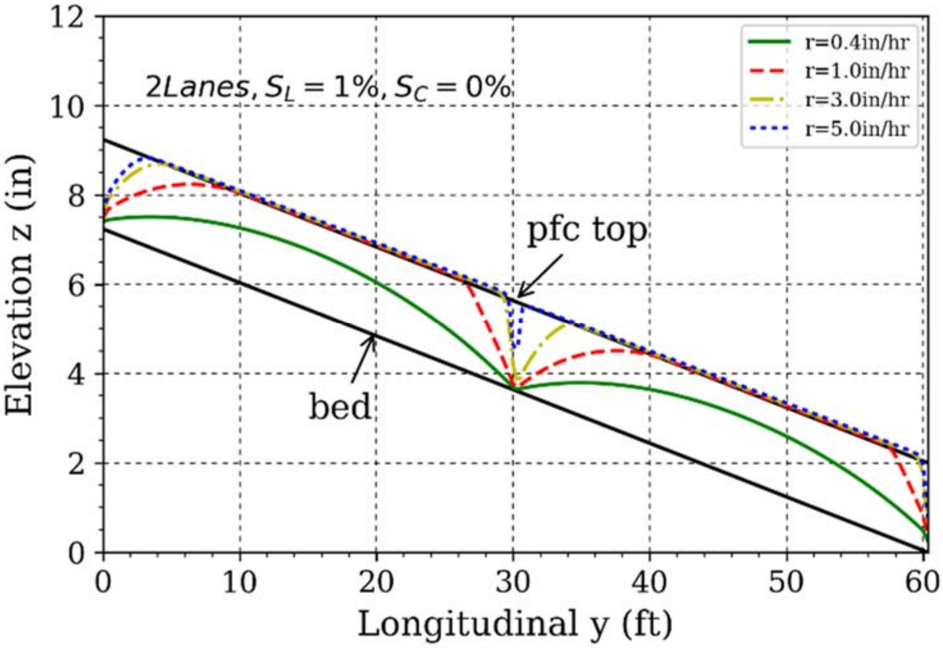

Figure 89. Influence range of underdrain on 2-lane PFC pavement with 1% longitudinal and 0% cross slope

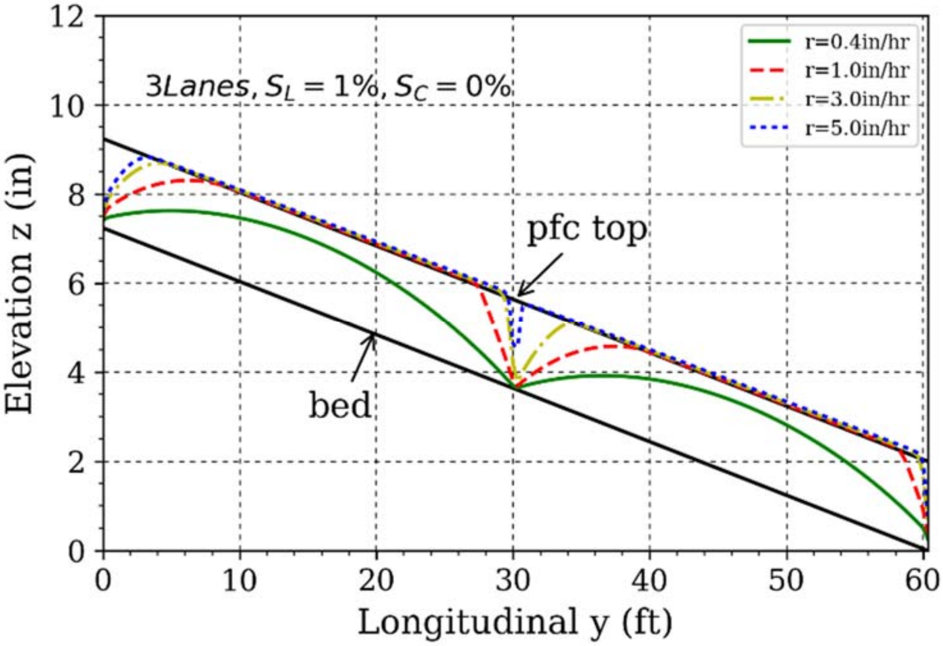

Figure 90. Influence range of underdrain on 3-lane PFC pavement with 1% longitudinal and 0% cross slope

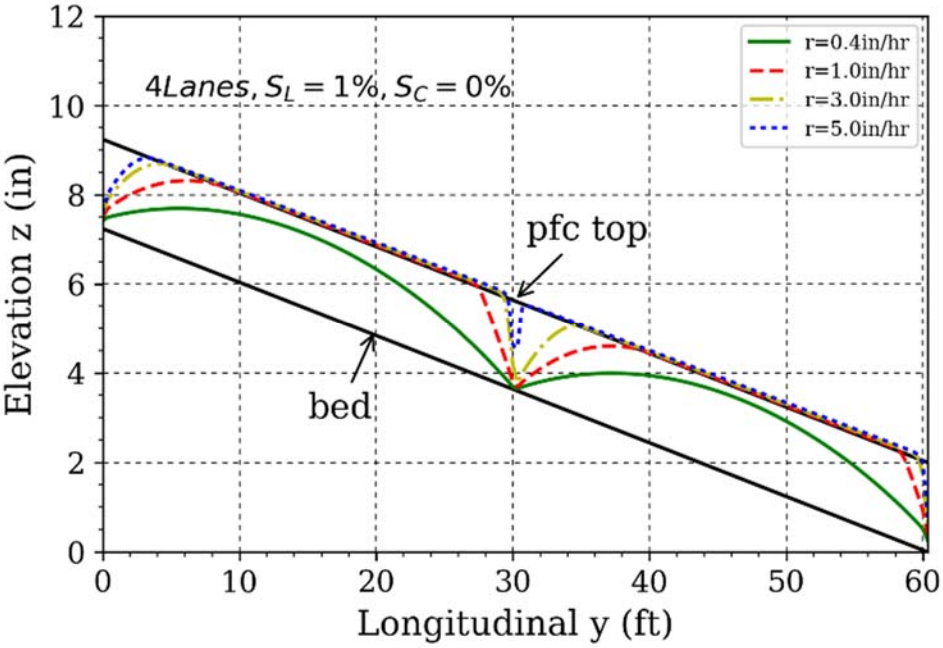

Figure 91. Influence range of underdrain on 4-lane PFC pavement with 1% longitudinal and 0% cross slope

6) Longitudinal slope = 1% and Cross slope = 1%

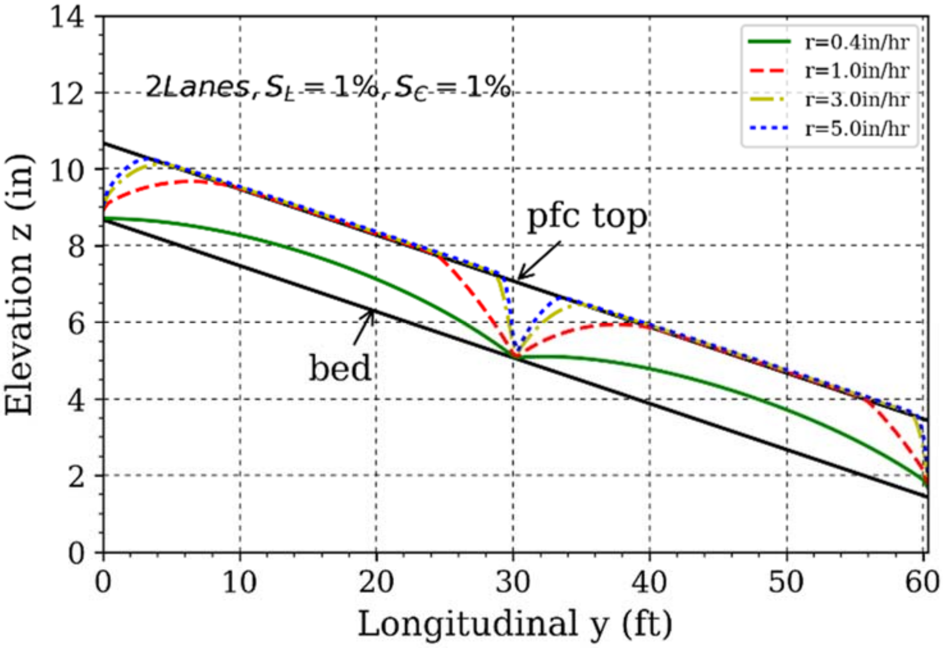

Figure 92. Influence range of underdrain on 2-lane PFC pavement with 1% longitudinal and 1% cross slope

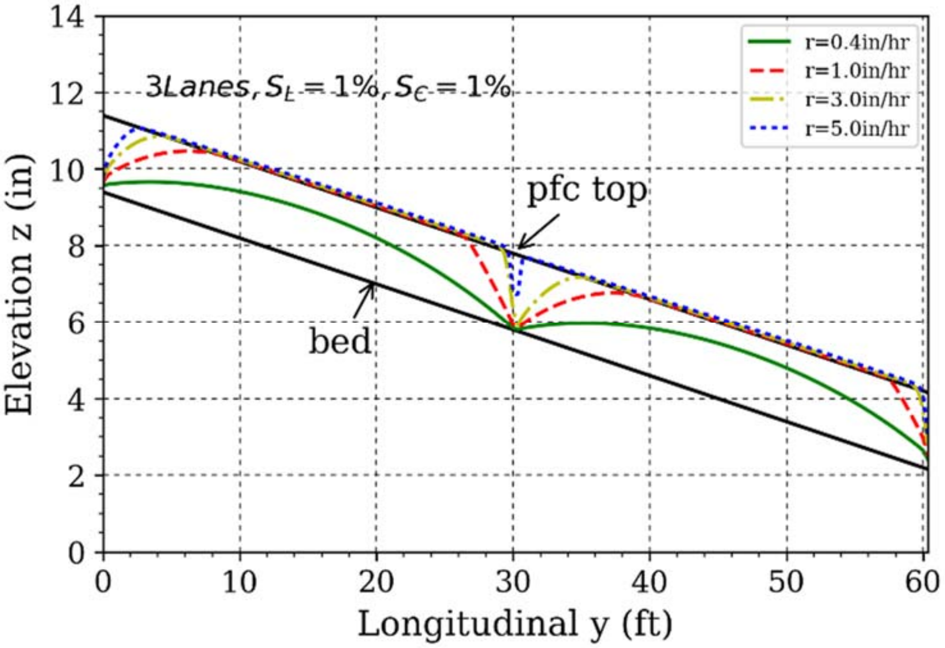

Figure 93. Influence range of underdrain on 3-lane PFC pavement with 1% longitudinal and 1% cross slope

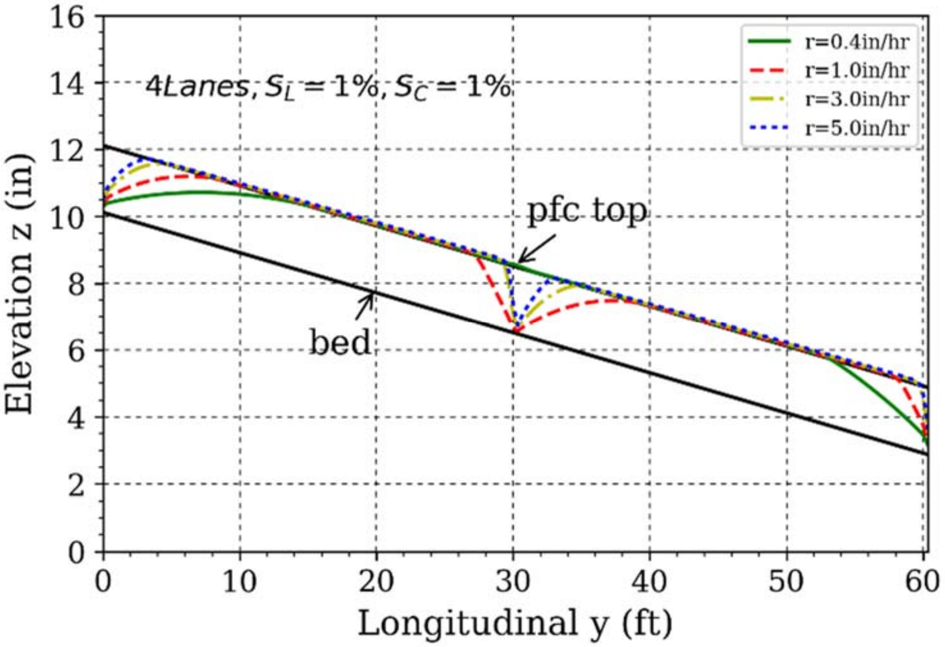

Figure 94. Influence range of underdrain on 4-lane PFC pavement with 1% longitudinal and 1% cross slope

7) Longitudinal slope = 1% and Cross slope = 2%

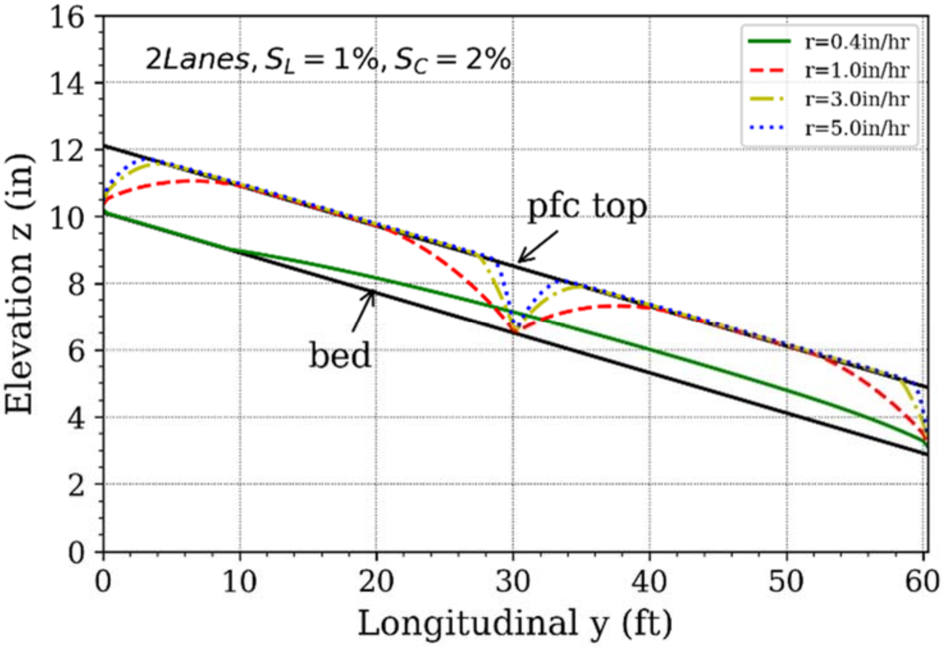

Figure 95. Influence range of underdrain on 2-lane PFC pavement with 1% longitudinal and 2% cross slope

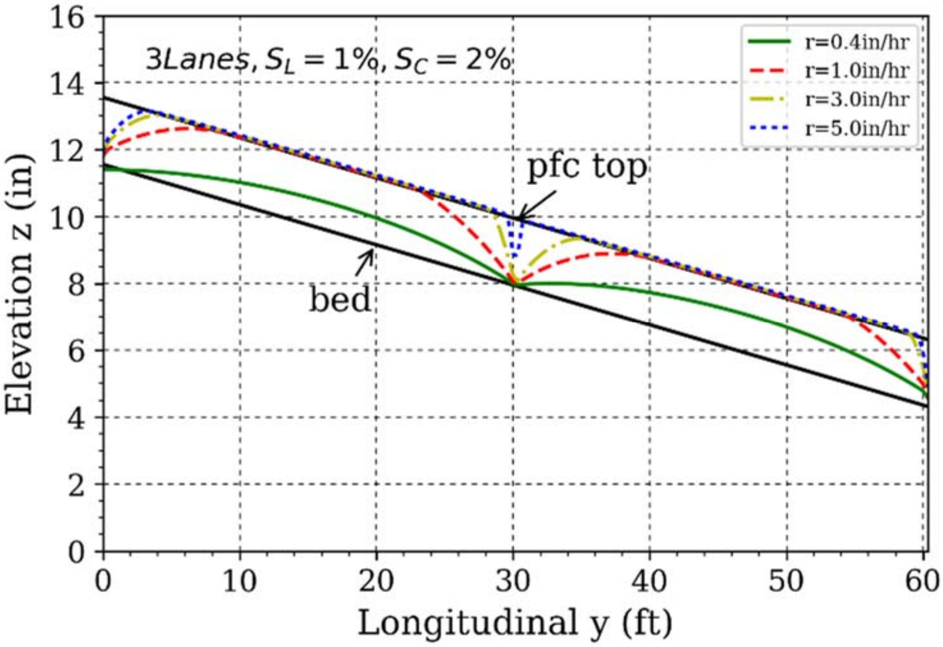

Figure 96. Influence range of underdrain on 3-lane PFC pavement with 1% longitudinal and 2% cross slope

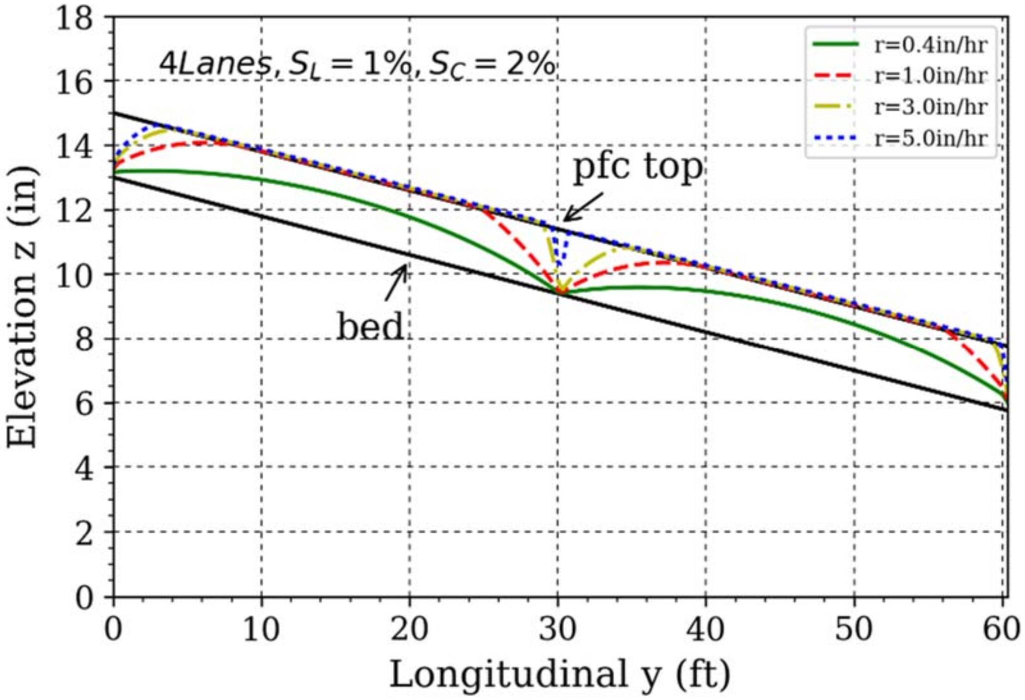

Figure 97. Influence range of underdrain on 4-lane PFC pavement with 1% longitudinal and 2% cross slope

8) Longitudinal slope = 1% and Cross slope = 3%

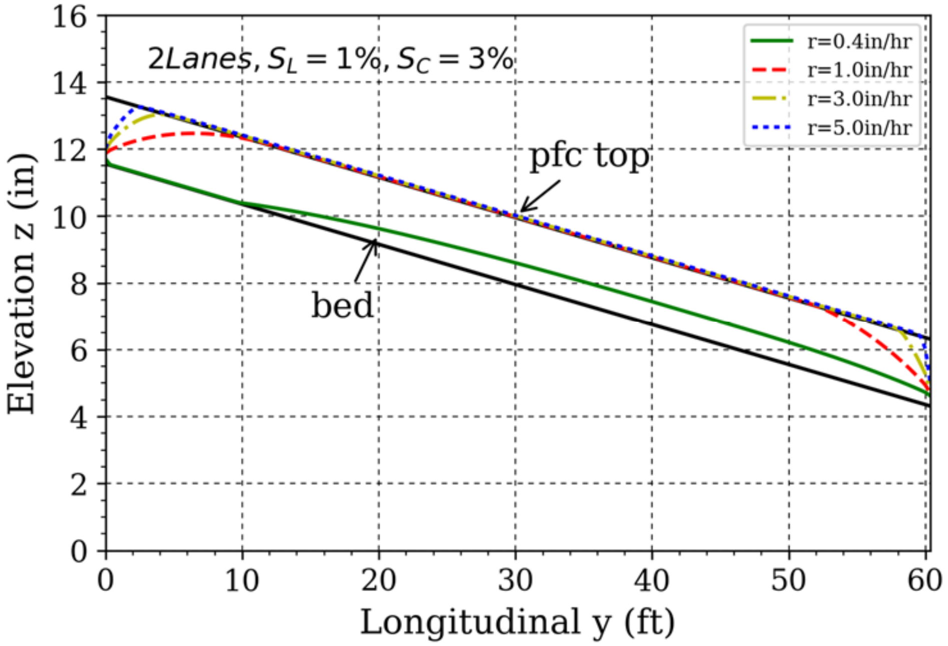

Figure 98. Influence range of underdrain on 2-lane PFC pavement with 1% longitudinal and 3% cross slope

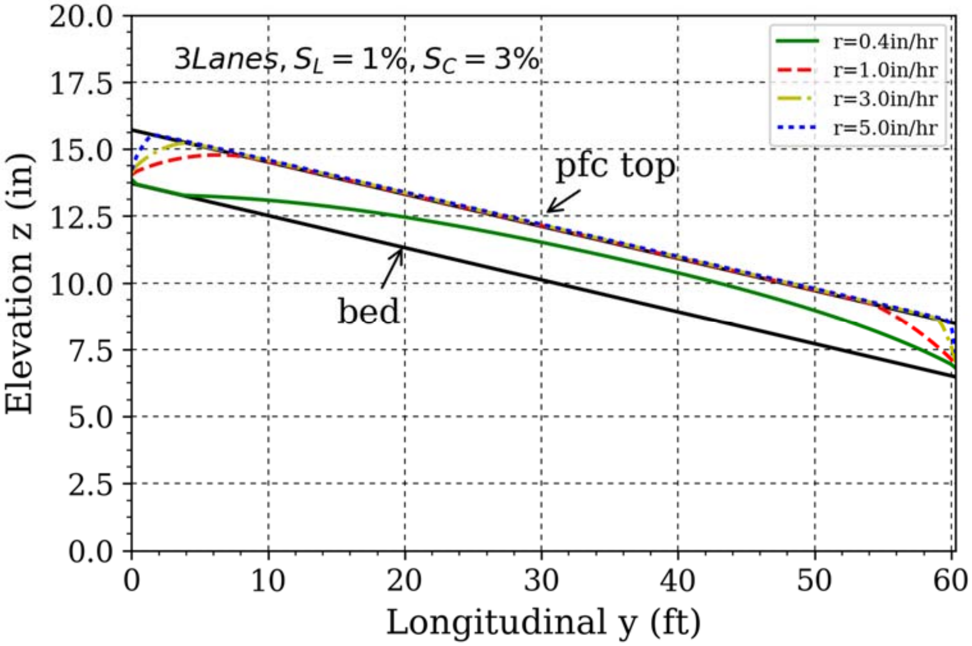

Figure 99. Influence range of underdrain on 3-lane PFC pavement with 1% longitudinal and 3% cross slope

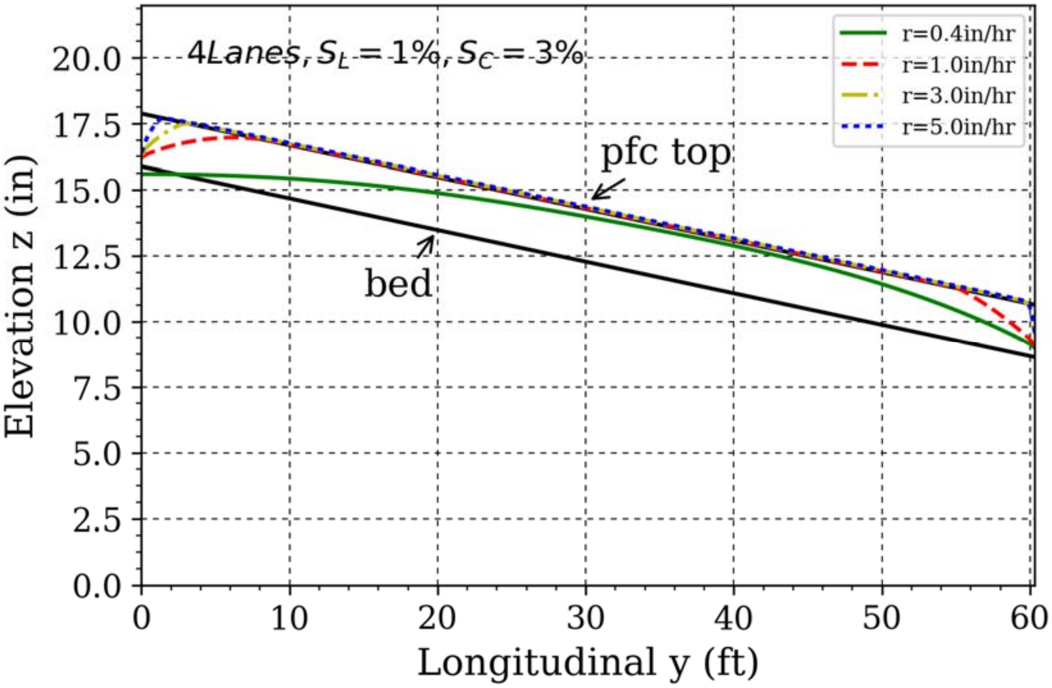

Figure 100. Influence range of underdrain on 4-lane PFC pavement with 1% longitudinal and 3% cross slope

CHAPTER 5: ANALYSIS, DISCUSSIONS, AND RECOMMENDATIONS

SUMMARY OF THE RESULTS AND FINDINGS

The data presented in Chapter 4 manifests that the underdrain has different degrees of effectiveness at the different pavement widths and slopes, and rainfall intensities. Effectiveness of the underdrain under various conditions is now quantified by an effective range, which defines the range that the standing water on the pavement can be removed, as illustrated in Figure 101. Namely, this range is the maximum allowable spacing of the underdrain if it is used for PFC.

The summary of the effective range for various conditions are presented in Tables 16-27. At a low rainfall intensity (i.e., 0.4 in/hr), there is no standing water on the pavement surface even without underdrain. For these situations, the effective range is indicated as “NN”, meaning “No Need”. An interesting finding from the results is that the combination of cross and longitudinal slopes does not necessarily promote the drainage all the time. The combination of cross and longitudinal slopes made the water drain downward faster; as a result, there is less water on the roadway crown and more water at the roadway edge. In summary, the combination of cross and longitudinal slopes may make the water ponding worse at the roadway edge.

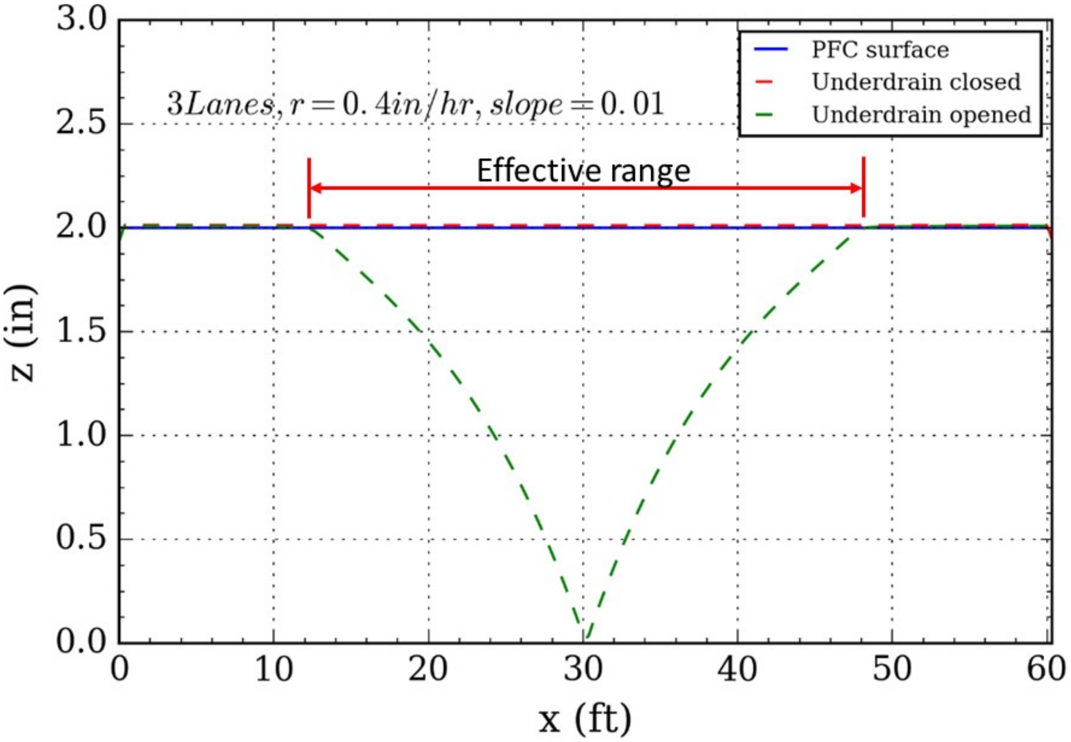

Figure 101. Effective influence range of underdrain

Table 16. Effective range for 2-lane pavement, rainfall intensity r = 0.4 in/hr

Effective range of Underdrain (ft), 2 Lanes, r = 0.4 in/hr		
Long. Slope y Cross Slope x	0%	1%
0%	NN	NN
1%	NN	NN
2%	NN	NN
3%	NN	NN

Table 17. Effective range for 2-lane pavement, rainfall intensity r = 1.0 in/hr

Effective range of Underdrain (ft), 2 Lanes, r = 1.0 in/hr		
Long. Slope y Cross Slope x	0%	1%
0%	20.5	18.5
1%	20.2	16.7
2%	22.3	21.9
3%	NN	11.5

Table 18. Effective range for 2-lane pavement, rainfall intensity r = 3.0 in/hr

Effective range of Underdrain (ft), 2 Lanes, r = 3.0 in/hr		
Long. Slope y Cross Slope x	0%	1%
0%	7.25	6.3
1%	8.6	6.6
2%	9.5	8.1
3%	9.54	8.82

Table 19. Effective range for 2-lane pavement, rainfall intensity r = 5.0 in/hr

Effective range of Underdrain (ft), 2 Lanes, r = 5.0 in/hr		
Long. Slope y Cross Slope x	0%	1%
0%	3.5	2.2
1%	1.83	4.6
2%	6.4	5.1
3%	3.5	5.18

Table 20. Effective range for 3-lane pavement, rainfall intensity r = 0.4 in/hr

Effective range of Underdrain (ft), 3 Lanes, r = 0.4 in/hr		
Long. Slope y Cross Slope x	0%	1%
0%	NN	NN
1%	NN	NN
2%	NN	NN
3%	NN	NN

Table 21. Effective range for 3-lane pavement, rainfall intensity r = 1.0 in/hr

Effective range of Underdrain (ft), 3 Lanes, r = 1.0 in/hr		
Long. Slope y Cross Slope x	0%	1%
0%	18	16.2
1%	17.8	13.5
2%	19.2	17.8
3%	20.4	18.4

Table 22. Effective range for 3-lane pavement, rainfall intensity r = 3.0 in/hr

Effective range of Underdrain (ft), 3 Lanes, r = 3.0 in/hr		
Long. Slope y Cross Slope x	0%	1%
0%	6.88	6.33
1%	7.6	6.2
2%	9	7.3
3%	9.08	7.48

Table 23. Effective range for 3-lane pavement, rainfall intensity r = 5.0 in/hr

Effective range of Underdrain (ft), 3 Lanes, r = 5.0 in/hr		
Long. Slope y Cross Slope x	0%	1%
0%	3	2.2
1%	1.5	1.5
2%	6	1.8
3%	6.23	3.2

Table 24. Effective range for 4-lane pavement, rainfall intensity r = 0.4 in/hr

Effective range of Underdrain (ft), 4 Lanes, r = 0.4 in/hr		
Long. Slope y Cross Slope x	0%	1%
0%	NN	NN
1%	NN	NN
2%	NN	NN
3%	NN	NN

Table 25. Effective range for 4-lane pavement, rainfall intensity r = 1.0 in/hr

Effective range of Underdrain (ft), 4 Lanes, r = 1.0 in/hr		
Long. Slope y Cross Slope x	0%	1%
0%	17.6	15.9
1%	17	12.8
2%	18	15.8
3%	18.76	17

Table 26. Effective range for 4-lane pavement, rainfall intensity r = 3.0 in/hr

Effective range of Underdrain (ft), 4 Lanes, r = 3.0 in/hr		
Long. Slope y Cross Slope x	0%	1%
0%	6.88	6.66
1%	7.08	5.9
2%	7.87	6.4
3%	8.7	4.13

Table 27. Effective range for 4-lane pavement, rainfall intensity r = 3.0 in/hr

Effective range of Underdrain (ft), 4 Lanes, r = 5.0 in/hr		
Long. Slope y Cross Slope x	0%	1%
0%	2.8	2.2
1%	1.5	3.7
2%	3.6	1.67
3%	4.23	1.9

SUGGESTED FUTURE WORK

The findings show that underdrains have an impact on the ability of PFC to drain ponding water. The spacing of underdrains for a 5 in/hr rain intensity is probably impractical in the transverse direction of the roadway (as was modeled) because the underdrain would appear for every 6 feet or less, which may cause concerns to the integrity of the roadway as well as the constructability.

A possible alternative could be to use transverse saw cuts (using the same machinery for grooved pavement, but applied across the travel direction, rather than in-line with travel direction), then, after the cuts are complete, apply the PFC over the cuts. The cuts would serve the role of the drain slot and could improve the drainage performance of PFC in hard-to-drain situations, while maintaining structural integrity (at least better than with 4-inch deep slots).

REFERENCES

Alvarez, A. E., Martin, A. P., Estakhri, C. K., Button, J. W., Glover, C. J., and Jung, S. H. (2006). "Synthesis of Current Practice on the Design, Construction, and Maintenance of Porous Friction Courses." 86.

APC (2003). "Open Graded Friction Courses: Smooth, Quiet, and More Durable than Ever." Asphalt Pavement Alliance.

Arambula, E., Estakhri, C. K., Martin, A. E., Trevino, M., Smit, A. D. F., and Prozzi, G. (2013). "Performance and Cost Effectiveness of Permeable Friction Course (PFC) Pavements." 254pp.

Barrett, M., and Stanard, C. (2008). "Effects of the permeable friction course (PFC) on highway Runoff." *11th International Conference on Urban Drainage* Edinburgh, Scotland, UK.

Bean, E. Z., Hunt, W. F., and Bidelspach, D. A. (2007). "Evaluation of four permeable pavement sites in eastern North Carolina for runoff reduction and water quality impacts." *Journal of Irrigation and Drainage Engineering*, 133(6), 583-592.

Bear, J. (1972). *Dynamics of Fluids in Porous Media*, American Elsevier Publishing Company Inc., New York.

Bendtsen, H., and Andersen, B. (2005). "Noise Reducing Pavements - State of the Art in Denmark." Road Directorate, Danish Road Institute, Denmark Ministry of Transport, Hedehusene, Denmark.

Berbee, R., Rijs, G., de Brouwer, R., and van Velzen, L. (1999). "Characterization and treatment of runoff from highways in the Netherlands paved with Impervious and pervious asphalt." *Water Environment Research*, 71(2), 183-190.

Brown, J. R. (1973). "Pervious Bitumen–Macadam Surfacings Laid to Reduce Splash and Spray at Stonebridge, Warwickshire." Transportation Road Research Laboratory, England.

Caltrans (2006). "Open Graded Friction Course Usage Guide, California Department of Transportation Division of Engineering Services."

Charbeneau, R. J. (2000). *Groundwater Hydraulics and Pollutant Transport*, Prentice-Hall, Upper Saddle River, NJ.

Charbeneau, R. J., and Barrett, M. E. (2008). "Drainage hydraulics of permeable friction courses," *Water Resources Research*, 44, W04417.

Charbeneau, R. J., Klenzendorf, J. B., and Barrett, M. E. (2011). "Methodology for determining laboratory and in situ hydraulic conductivity of asphalt permeable friction course." *Journal of Hydraulic Engineering*, 137(1), 15-22.

Collins, K. A., Hunt, W. F., and Hathaway, J. M. (2011). "Side-by-side comparison of nitrogen species removal for four types of permeable pavement and standard asphalt in eastern North Carolina." *Journal of Hydrologic Engineering*, 15(6), 512-521.

Collins, R. E. (1961). *Flow of Fluids through Porous Materials*, Reinhold, New York.

Cooley, L. A., Ahlrich, R. C., Watson, D. E., and Kandhal, P. S. (2007). "Improved Porous Friction Courses (PFC) on Asphalt Airfield Pavements." 29.

Cooley, L. A., Brumfield, J. W., Mallick, R. B., Mogawer, W. S., Partl, M., Poulikakos, L., and Hicks, G. (2009). "Construction and Maintenance Practices for Permeable Friction Courses." Washington D.C. 2009.

Decoene, Y. (1990). "Contribution of cellulose fibers to the performance of porous asphalt." *Transportation Research Record*, 1265, 82-86.

Donavan, P. R. (2005). "Comparative Measurement of Tire/Pavement Noise in Europe and the United States." Illingworth & Rodkin, Inc.

Eck, B., Winston, R., Hunt, W., and Barrett, M. (2012). "Water quality of drainage from permeable friction course." *Journal of Environmental Engineering*, 138(2), 174-181.

Ergun, S. (1952). "Fluid flow through packed columns." *Chemical Engineering Progress*, 48(2), 89–94.

Estakhri, C. K., Alvarez, A. E., and Martin, A. E. (2008). "Guidelines on Construction and Maintenance of Porous Friction Courses in Texas." 44.

Forchheimer, P. (1901). "Wasserbewegung dur Bodem." *Zeitschrift des Verbundes der deutschen Ingenieurs*, 45(1782-1788).

Fwa, T. F., Tan, S. A., and Chuai, C. T. (1998). "Permeability measurement of base materials using falling-head test apparatus." *Transportation Research Record*, 1615, 94-99.

Huang, K., Mohanty, B. P., and van Genuchten, M. T. (1996). "A new convergence criterion for the modified Picard iteration method to solve the variably saturated flow equation." *Journal of Hydrology*, 178(1–4), 69-91.

Huber, G. (2000). "Synthesis of Highway Practice 284: Performance Survey on Open-Graded Friction Course Mixes." Washington D.C.

Isenring, T., Koster, H., and Scazziga, I. (1990). "Experience with porous asphalt in Switzerland." *Transportation Research Record 1265*, 87-94.

Jackson, T. J., and Ragan, R. M. (1974). "Hydrology of porous pavement parking lots." *Journal of the Hydraulic Division*, 100(12), 1739-1752.

Jasak, H. (1996). "Error analysis and estimation for finite volume method with applications to fluid flow."

Kadlec, H. R., and Knight, L. R. (1996). *Treatment Wetlands*, CRC Press Lewis Publishers Boca Raton, Florida.

Kandhal, P. S., and Mallick, R. B. "Transportation Research Circular E-C500: Open Graded Asphalt Friction Course: State of Practice." *Proc., TRB*, National Research Council.

Kearfott, P., Barrett, M., and Malina, J. F. J. (2005). "Stormwater Quality Documentation of Roadside Shoulders Borrow Ditches." Center for Research in Water Resources, The University of Texas at Austin, Austin.

Khalid, H., and Perez, F. (1996). "Performance and Durability of Bituminous Materials." *Performance Assessment of Spanish and British Porous Asphalts*, E & FN Spon, London, 137-157.

Klenzendorf, J. B. (2010). "Hydraulic Conductivity Measurement of Permeable Friction Course (PFC) Experiencing Two-Dimensional Nonlinear Flow Effects." University of Texas at Austin.

Kovacs, G. (1981). *Seepage Hydraulics*, Elsevier Scientific Publishing Company, Amsterdam.

Kuzmin, D., Möller, M., and Turek, S. (2003). "Multidimensional FEM-FCT schemes for arbitrary time stepping." *International Journal for Numerical Methods in Fluids*, 42(3), 265-295.

Liu, K. W., Alvarez, A. E., Martin, A. P., Dossey, T., Smit, A., and Estakhri, C. K. (2010). "Synthesis of Current Research on Permeable Friction Courses: Performance, Design, Construction, and Maintenance."

Liu, X. (2012). "suGWFoam: an Open Source Saturated-Unsaturated GroundWater Flow Solver based on OpenFOAM." *Civil and Environmental Engineering Studies Technical Report*, No. 01-01.

Liu, X., Chen, Y., and Shen, C. (2016). "Coupled Two-Dimensional Surface Flow and Three-Dimensional Subsurface Flow Modeling for Drainage of Permeable Road Pavement." *Journal of Hydrologic Engineering*, 0(0), 04016051.

Liu, X., Chen, Y., and Shen, C. (2016). "Coupled two-dimensional surface flow and three-dimensional subsurface flow modeling for drainage of permeable road pavement." *Journal of Hydrologic Engineering*, 0(0).

Loaiciga, H. A. (2005). "Steady state phreatic surfaces in sloping aquifers." *Water Resources Research*, 41(W08402).

Luce, A., Mahmoud, E., Masad, E., and Chowdhury, A. (2007). "Relationship of aggregate microtexture to asphalt pavement skid resistance." *Journal of Testing and Evaluation*, 35(6).

Miller, M. M., and Johnson, H. D. (1973). "Effects of Resistance to Skidding on Accidents: Surface Dressing on an Elevated Section of the M4 Motorway." Transport and Road Research Laboratory, Berkshire, United Kingdom.

OpenFoam (2014). *OpenFOAM. The Open Source CFD Toolbox. Programmer's Guide*, Free Software Foundation, Inc.

OpenFoam (2014). *OpenFOAM. The Open Source CFD Toolbox. User Guide*, Free Software Foundation, Inc.

Pagotta, C., Legret, M., and Le Cloirec, P. (2000). "Comparison of the hydraulic behaviour and the quality of highway runoff water according to the type of pavement." *Water Resources*, 34(18), 4446–4454.

Poulikakos, L., Takahashi, S., and Partl, M. (2003). "A Comparison of Swiss and Japanese Porous Asphalt through Various Mechanical Tests." *Conference paper Swiss Transport Research Conference 2004. 3rd STRC*Monte Verità/Ascona.

Ranchet, J. (1995). "Impacts of porous pavements on the hydraulic behaviour and the cleansing of water." *Techniques Sciences et Méthodes 11*, 869-871.

Ranieri, V. (2002). "Runoff control in porous pavements." *Transportation Research Record*, 1789(46-55).

Richards, L. A. (1931). "Capillary conduction of liquids through porous mediums." *Physics-A Journal of General and Applied Physics*, 1(1), 318-333.

Ruiz, A., Alberola, R., Perez, F., and Sanchez, B. (1990). "Porous asphalt mixtures in Spain." *Transportation Research Record*, 1265, 87-94.

Sampson, L. C. (2013). "Permeable Friction Courses: Stormwater Quality Benefits and Hydraulic Profile Modeling." University of Texas – Austin.

Sampson, L. C. (2013). "Permeable friction courses: stormwater quality benefits and hydraulic profile modeling."

Sampson, L. C., Houston, A. V., Charbeneau, R. J., and Barrett, M. E. (2014). "Water Quality and Hydraulic Performance of Permeable Friction Course on Curbed Sections of Highways." 104.

Stotz, G., and Krauth, K. (1994). "The pollution of effluents from pervious pavements of an experimental highway section: first results." *The Science of the Total Environment*, 146/147, 465-470.

Szymkiewicz, A. (2012). *Modelling Water Flow in Unsaturated Porous Media: Accounting for Nonlinear Permeability and Material Heterogeneity,* Springer Science & Business Media.

Tan, S. A., Fwa, T. F., and Chuai, C. T. (1999). "Automatic field Permeameter for drainage properties of porous asphalt mixes." *Journal of Testing and Evaluation*, 27(1), 57-62.

TxDOT (2004). "Standard Specifications for Construction and Maintenance of Highways, Streets, and Bridges Adopted by the Texas Department of Transportation." Texas Department of Transportation, Austin, Texas.

van Der Zwan, J. T., Goeman, T., Gruis, H. J. A. J., Swar, J. H., and Oldenburger, R. H. (1990). "Porous asphalt wearing courses in the Netherlands: state of the art review." *Transportation Research Record*, 1265, 95-110.

van Genuchten, M. T. (1980). "A closed-form equation for predicting the hydraulic conductivity of unsaturated soils." *Soil Science Society of America Journal* 44(5), 892-898.

Ward, J. C. (1964). "Turbulent flow in porous media." *Journal of the Hydraulic Division*, 90(5), 1-12.

Weller, H. G., Tabor, G., Jasak, H., and Fureby, C. (1998). "A tensorial approach to computational continuum mechanics using object-oriented techniques." *Computers in Physics*, 12(6), 620-631.

Yildirim, Y., Dossey, T., Fults, K., Tahmoressi, M., and Trevino, M. (2007). "Winter Maintenance Issues Associated with New Generation of Open-Graded Friction Courses."

Zalesak, S. T. (1979). "Fully multidimensional flux-corrected transport algorithms for fluids." *Journal of computational physics*, 31(3), 335-362.